

This is the author's peer reviewed, accepted manuscript. However, the online version of record will be different from this version once it has been copyedited and typeset.

PLEASE CITE THIS ARTICLE AS DOI: 10.1063/5.0131032

AIP/123-QED

The stressful way of droplets along single fibre strands – A computational analysis

Francisco Bodziony,¹ Martin Wörner,² and Holger Marschall¹

¹*Computational Multiphase Flow Group, Mathematical Modeling and Analysis,
Department of Mathematics, Technical University Darmstadt, Darmstadt, Hessen, 64289,
Germany*

²*Institute of Catalysis Research and Technology (IKFT), Karlsruhe
Institute of Technology (KIT), Karlsruhe, Baden-Württemberg, 76131,
Germany*

(*Electronic mail: marschall@mma.tu-darmstadt.de)

(Dated: 9 December 2022)

Droplets wetting and moving on fibres are omnipresent in both nature and industry. However, little is known on the local stresses the fibre substrates experiences and, in turn, the local forces acting on those droplets while moving on vertical fibre strands. This work is concerned with disclosing the influence of droplet volume, viscosity and chemical substrate heterogeneity on droplet motion. For this purpose, we pursue a computational simulation campaign by means of direct numerical simulations resolving all relevant spatial and temporal scales. On the basis of local simulation data, we evaluate and analyse effective viscous dissipation rates as well as viscous and capillary forces. We also assess the validity of an assumption which is frequently used in correlations for droplets moving on single fibre strands – neglecting the capillary force. Our computational analysis allows to falsify/verify this assumption for different scenarios and reveals that such correlations have to be applied with care, particularly when it comes to chemical heterogeneity of the fibre substrates.

I. Introduction

Droplets wetting and moving on fibres are omnipresent in both nature and industry – from spider web arrangement to engineering applications in the textile^{1,2}, filters^{3,4} and the paper industry.

Plateau⁵ has been the first to study droplets spreading on fibres. He has observed that only due to surface tension, a liquid covering a fibre would turn into a string of beads, taking the shape of unduloids. Following up on these studies, many physicists have started investigating the flow of liquid films on threads, notably Lord Rayleigh⁶, who has studied liquid film instabilities for falling cylindrical jets which has been later expanded upon by Yarin et al.⁷ and conversely studied by Kliakhandler⁸, Craster⁹, Duprat¹⁰. The analytical solution to the unduloidal shape studied by Plateau has been later derived by Carroll^{11–13} who has analysed droplets which are molded by capillary forces. This analytical solution has been validated in the same paper for various systems and has been shown to be accurate for droplets that are not influenced by gravitational forces, are axisymmetrical and present a so-called "barrel shape", as opposed to a "clam-shell shape".

The motion of single droplets on fibres has also been extensively studied, where the droplet is set in motion due to gravitational effects^{14,15}, asymmetric slug in a tube¹⁶, temperature gradients¹⁷ and also due to radius gradients¹⁸. However, to the best of the authors' knowledge, no studies exist which investigate the transient droplet motion on fibres by means of Direct Numerical Simulations (DNS), i.e. resolving all relevant spatio-temporal scales. Thus far, numerical studies have been concerned with the equilibrium shape of droplet at fibres only. Venkateshan et al.¹⁹ have studied the 3D shape of water droplets with different volumes on various fibrous structures, using the finite element code Surface Evolver. Also using the same approach, Aziz et al.^{20–22} have investigated wetting of a liquid droplet on a fibre and fibrous coatings. In particular, the authors have studied the shape of a droplet deposited on a single fibre, the effect of the capillary force exerted on a fibre by a droplet and the volume residue after the droplet detachment. Modern manufacturing techniques allow now to produce fibers with controlled heterogeneous wettability²³ which are of interest for various applications including oil-water separation²⁴ and catalysis²⁵. The motion of a droplet on a fiber with controlled heterogeneous wettability due to a chemically inhomogeneous surface has not been studied numerically at all so far.

This contribution is concerned with a detailed numerical investigation of the transient spreading and motion of three-dimensional droplets on single fibres using Direct Numerical Simulations.

We aim to analyse the contribution of the local forces acting on a sliding droplet on a chemically homogeneous as well as heterogeneous (patterned) fibre strand. For this purpose, we deploy a phase-field method which has been shown to be particularly suited for accurately describing transient wetting processes with contact line dynamics^{26–28}, particularly since the underlying diffuse interface model inherently allows for a moving three-phase contact line in combination with the no-slip condition at solid walls^{29–31}.

Our diffuse interface phase-field solver is used – phaseFieldFoam, implemented in OpenFOAM (FOAM-extend 4.0 and 4.1). The solver phaseFieldFoam has been extensively validated for several cases of static and dynamic wetting, on both simple and complex substrates, such as chemically patterned surfaces^{32–35}. The objective of this work is two-fold, viz.

- to detail on crucial methodological aspects to devise a high-fidelity simulation of wetting processes using the phase-field approach and finite-volume discretisation with particular focus on non-planar substrates such as fibres,
- to provide local insights into the hydrodynamics of droplets spreading and moving on single fibres, in particular on the influence of wettability of chemically homogeneous substrates as well as of patterns of chemically heterogeneous substrates on local stresses and forces.

II. Mathematical Model

A. Cahn-Hilliard Navier-Stokes Equations

We assume two immiscible Newtonian fluid phases under isochoric and isothermal conditions. Then, the coupled Cahn-Hilliard Navier-Stokes equations read in semi-closed formulation (see [36]),

$$\partial_t C + \nabla \cdot (C\mathbf{u}) = -\nabla \cdot \mathbf{J}, \quad (1a)$$

$$\nabla \cdot \mathbf{u} = 0, \quad (1b)$$

$$\partial_t (\rho\mathbf{u}) + \nabla \cdot (\rho\mathbf{u}\mathbf{u}) = -\nabla \bar{p} + \nabla \cdot \boldsymbol{\tau} - \nabla \cdot (\mathbf{u}\mathbf{J}) - \Phi \nabla C + \mathbf{f}_b, \quad (1c)$$

where C denotes the phase-field order parameter, \bar{p} is a modified pressure, since parts of the known Korteweg tensor term accounting for interfacial capillarity have been absorbed into the pressure gradient term. Assuming a liquid of Newtonian fluid rheology, $\boldsymbol{\tau} = 2\mu \text{dev } \mathbf{D}$, where \mathbf{D} is the

rate-of-deformation (rate-of-strain) tensor, $\mathbf{D} = \frac{1}{2}(\nabla\mathbf{u} + (\nabla\mathbf{u})^T)$ and $\text{dev } \mathbf{D}$ denotes the deviatoric, trace-free part ($\text{tr}(\text{dev } \mathbf{D}) = 0$). Moreover, ρ and μ are the volumetric average density and dynamic viscosity of the fluids, given from the phasic densities and viscosities as $\rho = \frac{1+C}{2}\rho_1 + \frac{1-C}{2}\rho_2$ and $\mu = \frac{1+C}{2}\mu_1 + \frac{1-C}{2}\mu_2$, and $\mathbf{f}_b = \rho\mathbf{g}$ is the body force due to gravity. Note that herein we are using the contrast of volumetric phase fractions as order parameter C that is $C \in [-1, 1]$, opposed to concentrations in some other treatises.

With this, the set of governing equations (1) is closed – apart from \mathbf{J} which denotes the phase-field flux. Following Landau & Lifshitz³⁷, it is governed by generalizing Fick's law as $\mathbf{J} = -M\nabla\Phi$, where Φ is the chemical potential and M the mobility. In other words, under the above assumptions, the dynamics of the phase-field system is fundamentally driven by the gradient in the local chemical potential Φ . Note that the term $\nabla \cdot (\mathbf{u}\mathbf{J})$ is required for thermodynamic consistency^{29,38}.

Within the diffuse-interface model framework, following Cahn and Hilliard³⁹, the local chemical potential arises from the variational derivative of the total free energy F (Helmholtz free energy), which is considered as a *functional* of the order parameter C , viz.

$$\Phi = \frac{\delta F_m(C, \nabla C)}{\delta C}, \quad (2)$$

where F_m denotes the bulk (mixing) contribution to the total free energy of the system,

$$F = F_m + F_w = \int_{\Omega} f_m(C, \nabla C) \, d\mathbf{x} + \int_{\partial\Omega} f_w(C) \, ds. \quad (3)$$

Herein, Ω is the fluid domain and $\partial\Omega$ its boundary, a solid surface not permeable to fluids. The local mixing energy and the local wall energy densities are denoted f_m and f_w , respectively. The mixing energy density (Helmholtz free energy density)³⁹ can be written as

$$f_m = \frac{1}{2}\lambda|\nabla C|^2 + \frac{\lambda}{\epsilon^2}\Psi(C). \quad (4)$$

The first term on the r.h.s. of (4) is the gradient energy, which represents the interfacial energy density describing non-local interactions between the two components promoting complete mixing of the fluids, while the second term is the so-called bulk energy density, which models the counter tendency to separate²⁸.

B. Wetting Condition

The wall free energy density in (3) can be written as

$$f_w = \sigma_{SL} + (\sigma_{SG} - \sigma_{SL})\Psi_w(C), \quad (5)$$

where $\Psi_w(C)$ obeys the bulk limits $\Psi_w(C = -1) = 0$ and $\Psi_w(C = 1) = 1$, respectively.

A variational procedure, i.e. variation in F_w and intergration by parts, reveals that

$$\lambda \partial_n C + f'_w(C) = 0, \quad (6)$$

where λ is the mixing energy coefficient and $f'_w(C) = (\sigma_{SG} - \sigma_{SL})\Psi'_w(C)$ denotes the derivative of the wall free energy density with respect to the order parameter. Effectively (5) postulates that the wall free energy density is a function only of the fluid composition next to the wall²⁸. Eq. (6) is commonly referred to as wetting condition. It describes the diffusive relaxation process of the dynamic contact angle locally constraining towards the equilibrium angle to leading order^{28,30}.

Now, choosing a particular double-well potential function $\Psi(C)$ allows closure. Using the phenomenological double-well function of polynomial form according Ginzburg and Landau, $\Psi(C) = \frac{1}{4}(C^2 - 1)^2$, the equilibrium profile of the order parameter can be derived by minimisation of the free energy: requiring $\Phi := \frac{\delta F}{\delta C} = \frac{\lambda}{\varepsilon^2}\Psi'(C) - \lambda\Delta C \stackrel{!}{=} 0$, where Φ denotes the chemical potential, and assuming a planar interface, leads to

$$C(n) = \tanh\left(\frac{n}{\sqrt{2}\varepsilon}\right), \quad (7)$$

where n denotes the interfacial normal vector and ε is a measure of the width of the diffuse interface, commonly referred to as interfacial capillary width. Within $3/\sqrt{2}\varepsilon$ the order parameter C varies from about -0.9 to 0.9 . Under these assumptions, one can also show that the mixing energy coefficient λ within the diffuse interface context can be related to the surface tension coefficient employed in sharp interface models by

$$\lambda = \frac{3}{2\sqrt{2}}\sigma\varepsilon. \quad (8)$$

With this, we can exploit fundamental geometrical relations: if the interface makes a contact angle θ_0 with a wall (see Fig. 1), using a coordinate system which holds the wall normal n_w as one

coordinate and t_w as the other, gives

$$n = n_w \cos(\theta_0) + t_w \sin(\theta_0). \quad (9)$$

Differentiating the equilibrium profile $C(n)$ along the coordinate normal to the wall as

$$\partial_n C = \frac{\partial C(n)}{\partial n_w} = \frac{\partial C(n)}{\partial n} \frac{dn}{dn_w}, \quad (10)$$

allows us to recognise

$$\frac{\partial C(n)}{\partial n} = \frac{1}{\sqrt{2\varepsilon}} \left(1 - \tanh^2 \left(\frac{n}{\sqrt{2\varepsilon}} \right) \right) = \frac{1}{\sqrt{2\varepsilon}} (1 - C^2(n)),$$

from (7) and

$$\frac{dn}{dn_w} = \cos \theta_0,$$

from a simple geometrical observation. Thus, we finally arrive at the wetting boundary condition,

$$\partial_n C = \frac{\cos \theta_0}{\sqrt{2\varepsilon}} (1 - C^2(n)). \quad (11)$$

Using the Young-Dupré equation⁴⁰,

$$(\sigma_{SG} - \sigma_{SL}) = \sigma_{GL} \cos \theta_0, \quad (12)$$

it can be shown that (5) can be written in closed form as³⁰

$$f_w = \sigma \cos \theta_0 \frac{C(C^2 - 3)}{4} + \frac{\sigma_{SL} + \sigma_{SG}}{2}. \quad (13)$$

Here, we have used the wetting condition (6), since $\Psi_w(C) = \frac{C(C^2-3)-2}{4}$ is a closure restoring (11), inserting λ according to (8) and $(\sigma_{SG} - \sigma_{SL})$ according to (12) into (6). Note carefully how the particular choice of the double-well function $\Psi(C)$ according to Ginzburg and Landau has allowed us to consistently close for the phase-field transport equation and the wetting boundary condition. Both closures are indeed connected.

$$\partial_n \Phi = 0 \quad (14)$$

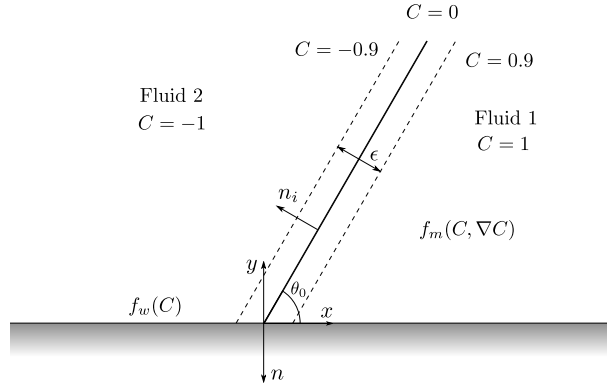


FIG. 1: Contact line in the diffuse-interface setting: n is the inward normal to the wall, n_i is the normal to the interface in the direction of ∇C , and ϵ is the capillary width.

C. No-Slip Condition

The Navier-Stokes equations are supplemented by the no-slip wall boundary conditions on the solid substrate $\partial\Omega_w$, viz.

$$\mathbf{u}|_w \stackrel{!}{=} \mathbf{u}_w \quad (15)$$

intuitively requiring that the velocity of the fluid at the wall $\mathbf{u}|_w$ is equal to the velocity of the wall \mathbf{u}_w . Equivalently, one can demand for the normal velocity component that

$$\dot{m}_w = \rho(\mathbf{u} - \mathbf{u}_w) \cdot \mathbf{n}_w \stackrel{!}{=} \mathbf{0}, \quad (16)$$

i.e. to fulfill a no-penetration condition due to impermeability of the wall, and for the tangential velocity component that

$$\mathbf{P}_w \cdot (\mathbf{u} - \mathbf{u}_w) = \mathbf{0}, \quad (17)$$

where $\mathbf{P}_w := \mathbf{I} - \mathbf{n}_w \mathbf{n}_w$ is the projection operator onto the tangent plane of the boundary with outer unit normal \mathbf{n}_w , and \mathbf{I} denotes the identity or unit diagonal tensor. Moreover, it is

$$\mathbf{K} - (\mathbf{n}_w \cdot \mathbf{K}) \mathbf{n}_w = \boldsymbol{\tau}_w, \quad (18)$$

where \mathbf{K} denotes the wall-tangential contribution of the viscous boundary force per unit area, $\mathbf{K} := \mu (\nabla \mathbf{u} + (\nabla \mathbf{u})^\top) \mathbf{n}_w$, which amounts to the viscous wall stress $\boldsymbol{\tau}_w$ exerted to the wall.

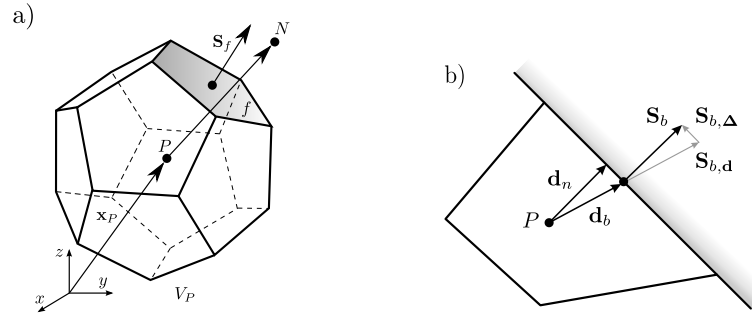


FIG. 2: Finite volume notation for equation discretisation on unstructured meshes. (a) Polyhedral Control Volume and (b) Boundary Control Volume.

III. Numerical Method

In the following we attempt to provide an overview of the numerical method of the phaseField-Foam solver. One focus shall be on the discretisation of the Cahn-Hilliard equation, since it is a non-linear fourth-order partial differential equation (PDE) and thus challenging to treat numerically in an accurate yet robust manner. Hence, special care must be taken in the solution method as set out in the remainder. Moreover, the Moving Reference Frame (MRF) technique and its implementation is described, since it is crucial for an efficient deployment of computational resources by significantly reducing the required size of the computation domain. Moreover, we detail on the requirement of a consistent no-slip boundary condition at fibre walls which is different from the de-facto standard Dirichlet boundary condition imposing a zero velocity field at walls in the linear momentum equation.

A. Cahn-Hilliard Equation Discretisation

The Cahn-Hilliard equation is a non-linear fourth-order PDE and thus challenging to treat numerically in an accurate yet robust manner. The difficulty originates from its right-hand-side. Illustratively, this can be seen by considering the mechanism of interfacial evolution, which within the diffuse-interface model theory is governed by dissipation of the free energy functional according

to (3) as⁴¹

$$\partial_t C = -\frac{\delta F}{\delta C}. \quad (19)$$

Note that (19) is void of the advection term which is not needed here for making this point: in order to promote numerical stability, it is desirable to employ a temporal discretization which satisfies the discrete energy stability condition, viz. the decay of energy with time as

$$F(C^n) \leq F(C^o), \quad (20)$$

where the superscripts n and o denote the new and old time levels, respectively. It is a common practice to devise a splitting technique to avoid implicit schemes which come at the cost of solving a non-linear non-convex problem, i.e. to incorporate the r.h.s. of (19) at the new time level. While such schemes enjoy stability when solving the inherently stiff phase-field equations, there are alternative schemes offering a better performance. Depending on the approximation of the potential terms in $f_m(C^n, C^o)$ and $f_w(C^n, C^o)$, see (3), one arrives at different schemes with distinct stability properties. One distinguishes linear and non-linear approximations of the potential terms. We shall continue to focus on linear schemes, since they do not suffer from the significant computational overhead of non-linear schemes, which require iterative methods. More particular, in the remainder we consider the well-established linear Eyre approximation, dating back to the work of Elliott and Stuart⁴² but named after Eyre⁴³, and the optimal dissipation approximation⁴⁴. For the sake of brevity, we shall refer to these schemes as *stable* and *optimal*, according to their properties, namely unconditional energy-stability due the existence of numerical dissipation, and conditional energy-stability but optimal dissipation, respectively. For an overview and detailed discussion the reader is referred to the work of Tierra and Guillén-González⁴¹. Since [41] details on the mixing energy potential f_m term, we shall further restrict ourselves in the remainder to the wall energy potential f_w and its numerical treatment in the boundary condition for the order parameter. It is important to note that both terms have to be approximated consistently, i.e. using the same scheme, so as to simulate wetting processes at high physical fidelity by phase-field methods.

For the discretization of the temporal term (`ddtSchemes`), a first order accurate Euler scheme is employed. Regarding the advection term discretization (`divSchemes`), for the divergence term of the scalar transport of the order parameter a high-resolution scheme (`Gamma`) is used, while the convection term of the momentum equation is discretized using `limitedLinearV` scheme, which is second order accurate. The gradient term (`gradSchemes`) is discretized with the sec-

and order accurate (linear) scheme and the laplacian term (laplacianSchemes) with (linear corrected).

Discretisation of the wetting condition

The wetting boundary condition (11) for the phase-field evolution equation can be also stated in general notation as so-called convective boundary condition (or boundary condition of third kind), viz.

$$k\partial_n\phi + h(\phi - \phi_{\text{ref}}) = 0. \quad (21)$$

For implementation, we cast this as Robin or mixed-type boundary condition, viz.

$$\phi_b = \omega_b\phi_{\text{ref}} + (1 - \omega_b)(\phi_P + \mathbf{g}_{\text{ref}} \cdot \mathbf{d}_n), \quad (22)$$

where ϕ_b refers to the boundary patch value (i.e. the value on the boundary face b) and ϕ_P is the internal cell value adjacent to the boundary face, cp. Fig. 2. Moreover, $\omega_b \in [0, 1]$ are weights, \mathbf{d}_n is face-normal component of the distance vector between the boundary face centre and the adjacent cell centre, and ϕ_{ref} and \mathbf{g}_{ref} denote a reference value and reference gradient, respectively. To deploy a Robin (mixed) boundary condition, appropriate values for ϕ_{ref} , \mathbf{g}_{ref} and ω_b must be found. For this, (21) is linearized as

$$k\frac{\phi_b - \phi_P}{|\mathbf{d}_n|} + h(\phi_b - \phi_{\text{ref}}) = 0. \quad (23)$$

With this, we obtain

$$\phi_b = \frac{h}{\frac{k}{|\mathbf{d}_n|} + h}\phi_{\text{ref}} + \frac{\frac{k}{|\mathbf{d}_n|}}{\frac{k}{|\mathbf{d}_n|} + h}\phi_P. \quad (24)$$

From comparison with (22) we find $\omega_b = \frac{h}{k/|\mathbf{d}_n| + h}$ and $\mathbf{g}_{\text{ref}} = \mathbf{o}$. It remains to determine k , h and ϕ_{ref} as well as ϕ_P from comparing with (6). Immediately, one identifies $k = \lambda$. To take advantage from a semi-implicit discretization in a linear scheme we note that $\phi_b = C_b^n$, where n denotes the new time level. Moreover, with the wall free energy density, cf. (5), which is repeated here for convenience,

$$f_w = \sigma_{SL} + (\sigma_{SG} - \sigma_{SL})\Psi_w(C),$$

where the non-linear wall potential is $\Psi_w(C) = \frac{C^3 - 3C}{4}$ for the chosen phenomenological Ginzburg-Landau potential, and where $\sigma_{SG} - \sigma_{SL} = \sigma \cos \theta_0$ (cf. (12)), the first derivative of $f_w(C)$ with respect to the order parameter C can be written as

$$f'_w(C) = -\frac{3}{4}\sigma \cos \theta_0(1 - C^2). \quad (25)$$

This is the author's peer reviewed, accepted manuscript. However, the online version of record will be different from this version once it has been copyedited and typeset.

PLEASE CITE THIS ARTICLE AS DOI: 10.1063/1.50131032

TABLE I: Splitting scheme parameters for wetting boundary condition

scheme	ω_b	k	h	ϕ_{ref}	g_{ref}
stable	$\frac{h}{\frac{k}{ d_n } + h}$	λ	$\beta \frac{3}{4} \sigma \cos \theta_0$	$\frac{1}{\beta} (1 + \beta C^o - (C^o)^2)$	0
optimal	$\frac{h}{\frac{k}{ d_n } + h}$	λ	$\frac{3}{4} \sigma \cos \theta_0 C^o$	$\frac{1}{C^o}$	0
no splitting	0	-	-	-	$\frac{\sqrt{2} \cos \theta_0}{2 \epsilon} (1 - (C^o)^2)$

Adding dissipation to this yields the stable scheme, which is of first order in time,

$$f'_w(C^n, C^o) = \beta \frac{3}{4} \sigma \cos \theta_0 C^n - \frac{3}{4} \sigma \cos \theta_0 (1 - \beta C^o - (C^o)^2), \quad (26)$$

and choosing the parameter $\beta = C^o$ leads to the optimal scheme, a second order in time scheme,

$$f'_w(C^n, C^o) = -\frac{3}{4} \sigma \cos \theta_0 (1 - C^o C^n). \quad (27)$$

Comparison of (6) and (21) then allows to eventually determine h and ϕ_{ref} . The parameters are summarized in Table I. It is noteworthy that these parameters are valid only for the chosen phenomenological Ginzburg-Landau potential and must be changed upon choice of other potentials.

Tierra and Guillén-González⁴¹ have noted that the energy stability condition is only satisfied for appropriate values of β , viz. $\beta \geq (3(C^n)^2 - 1)/2$. With such a condition a value of β can be determined large enough to assure that the scheme is energy-stable. However, this has limits: it has been shown in [44] that wrong equilibrium solutions can be the consequence of introducing too much numerical dissipation.

B. No-Slip Boundary Condition

From Section II C it is evident that special attention has to be devoted when discretising the viscous stress term in the momentum equation. In particular, (18) must be enforced on discrete level.

For Newtonian fluids the viscous stress tensor can be closed as $\boldsymbol{\tau} = \mu(\nabla \mathbf{u} + (\nabla \mathbf{u})^\top)$. Then, deploying the finite volume method,

$$\begin{aligned} \int_{V_p} \nabla \cdot \boldsymbol{\tau} \, d\mathbf{x} &= \int_{V_p} \nabla \cdot [\mu(\nabla \mathbf{u} + (\nabla \mathbf{u})^\top)] \, d\mathbf{x} \\ &= \sum_{f,i=1}^{n_{f,i}} \mu_f \mathbf{S}_f \cdot (\nabla \mathbf{u})_f + \sum_{f,b=1}^{n_{f,b}} \mu_f \mathbf{S}_f \cdot (\nabla \mathbf{u})_f + [(\nabla \mathbf{u}) \cdot \nabla \mu] V_p, \end{aligned} \quad (28)$$

where i and b denote inner and boundary faces, respectively. Here, we have used that $\nabla \cdot (\mu(\nabla \mathbf{u})^\top) = (\nabla \mathbf{u}) \cdot \nabla \mu + \mu \nabla(\nabla \cdot \mathbf{u})$. For a single boundary face b , finite volume discretisation yields

$$\begin{aligned} \mu_b \mathbf{S}_b \cdot (\nabla \mathbf{u})_b &= \mu_b |\mathbf{S}_b| \frac{\mathbf{u}_b - \mathbf{u}_P}{|\mathbf{d}_n|} \\ &= \mu_b |\mathbf{S}_b| \frac{1}{|\mathbf{d}_n|} \mathbf{u}_b + \mu_b |\mathbf{S}_b| \frac{-1}{|\mathbf{d}_n|} \mathbf{u}_P, \end{aligned} \quad (29)$$

where the last identity shows the split into explicit contribution to the source vector (first term) and the implicit contribution to the system matrix (second term), respectively.

However, while this is accurate for orthogonal Cartesian boundary cells, for non-planar boundary patches (skewed meshes) one must ensure that the applied boundary condition guarantees that the wall shear stress $\boldsymbol{\tau}_w$ is tangent to the wall along with \mathbf{u}_w ⁴⁵, cp. (18),

$$\begin{aligned} \mu_b \mathbf{S}_b \cdot (\nabla \mathbf{u})_b &= \mu_b |\mathbf{S}_b| \frac{(\mathbf{u}_b - \mathbf{u}_P)_\parallel}{|\mathbf{d}_n|} \\ &= \mu_b |\mathbf{S}_b| \frac{(\mathbf{u}_b - \mathbf{u}_P) - [(\mathbf{u}_b - \mathbf{u}_P) \cdot \mathbf{n}_b] \mathbf{n}_b}{|\mathbf{d}_n|} \\ &= \mu_b |\mathbf{S}_b| \frac{\mathbf{P}_w(\mathbf{u}_b - \mathbf{u}_P)}{|\mathbf{d}_n|}. \end{aligned} \quad (30)$$

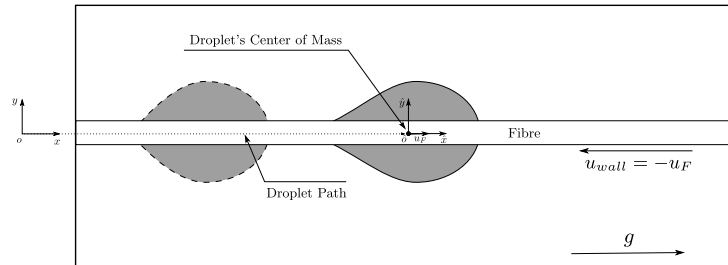


FIG. 3: Sketch of the Moving Reference Frame (MRF) technique.

C. Moving Reference Frame Technique

In order to reduce computational costs, a Moving Reference Frame (MRF) technique has been employed. Following the droplet's center of mass during the simulation, such a technique allows to significantly reduce the computational domain size.

Here, we are dealing with a non-inertial non-rotating reference frame. This method has been successfully used in rising bubble simulations^{46,47} and is convenient to implement due to its simplicity.

Fig. 3 depicts the situation for a droplet sliding on the surface of a vertically aligned fibre: the droplet slides with respect to the inertial reference frame (x, y, z) but remains centred within the computational domain in the non-inertial frame of reference $(\hat{x}, \hat{y}, \hat{z})$.

For this, we add the frame acceleration \mathbf{a}_F to the momentum equation (1) as

$$\frac{\partial(\rho \mathbf{u}_F)}{\partial t} + \rho \mathbf{a}_F + \nabla \cdot (\rho \mathbf{u}_F \otimes \mathbf{u}_F) = -\nabla \bar{p} + \nabla \cdot \boldsymbol{\tau} + \Phi \nabla C + \mathbf{f}_b. \quad (31)$$

The acceleration \mathbf{a}_F and velocity \mathbf{u}_F of the moving reference frame relative to the inertial reference frame are given by

$$\mathbf{a}_F = \frac{d\mathbf{u}_F}{dt} \quad \text{and} \quad \mathbf{u}_F = \frac{d\mathbf{x}_F}{dt}. \quad (32)$$

Herein, \mathbf{x}_F is the droplet centre of mass relative to the moving reference frame.

The velocity of the moving reference frame is adjusted at the beginning of each time step so as to keep the droplet barycentre at a fixed location within the computational domain. This is done by applying a velocity correction $\Delta \mathbf{u}_F$ for each time step. This correction is computed using a

PID controller where the control variable is the droplet's centre position vector. This vector is compared to a given constant target position. The applied velocity correction is

$$\Delta \mathbf{u}_F = \left(K_P \mathbf{e}_F + K_I \int_0^t \mathbf{e}_F dt + K_D \frac{\mathbf{e}_F - \mathbf{e}_F^o}{\delta t} \right) \frac{1}{\Delta t}, \quad (33)$$

where

$$\mathbf{e}_F = \mathbf{x}_F - \mathbf{x}_F^o. \quad (34)$$

Following the proposal in [46], a PID controller suffers significantly less from oscillations compared to a PD controller which has been used in [47].

At every time step, the frame velocity field is then updated

$$\mathbf{u}_F = \mathbf{u}_F^o + \Delta \mathbf{u}_F, \quad (35)$$

and used according to (32) for the calculation of the reference frame acceleration.

Since there also exists a solid wall in contact with the droplet, we impose a wall velocity which is equal in value to the frame velocity but opposite in sign, viz.

$$\mathbf{u}_w = -\mathbf{u}_F. \quad (36)$$

Effectively, this ensures that the droplet barycentre is kept in place.

IV. Validation

Note that our phase-field solver has been previously subject to significant validation efforts regarding wetting and de-wetting processes⁴⁸ and applied to different complex wetting physics^{32,49}. Here, we focus on three-dimensional cases relevant to droplets wetting on fibers such as the evolution of the spreading diameter and equilibrium shape of a droplet on flat and particularly spherical surfaces⁵⁰, as well as the spreading of a droplet on single fibre strand, where the dimensions of the equilibrium shape of an axisymmetric droplet on a cylinder are compared with literature-known reference data^{15,51,52}.

For model calibration, we have initially pursued a parameter study based on the first case (see Section IV A) in order to determine free model parameters of the phase-field method, which have been then fixed for all further simulations in this study. Because all the cases examined are capillary-dominated transient flows with low Reynolds numbers, we use an adaptive time-step

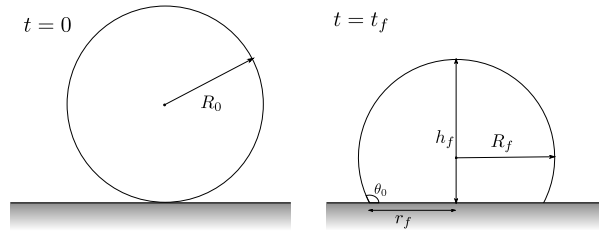


FIG. 4: Schematic representation of the initial (left) and equilibrium (right) shapes of a droplet on a flat surface with static contact angle θ_0 , in the absence of gravity.

TABLE II: Physical properties.

property	oil	water
density (kg/m^3)	950	1000
kinematic viscosity (m^2/s)	2e-5	1e-6
surface tension (N/m)	0.02	

criteria, where the time-steps are adjusted based on the maximum Brackbill-Kothe-Zemach (BKZ) criterion $\Delta t_{\max}^{\text{BKZ}} = \frac{1+\sqrt{5}}{2} \sqrt{\frac{\rho}{\sigma} h^3}$, as proposed in [53]. In this work, we set $\text{CFL}^{\text{BKZ}} = 1$. For time accuracy, we further restrict the maximum time step size computed according this BKZ criterion and require $\Delta t_{\max} = 2 \cdot 10^{-6}$ s.

A. Droplet spreading on a flat surface

1. Computational setup and physical properties

The equilibrium shape of an oil droplet in water on a flat surface with static contact angle, θ_0 , is investigated. A schematic representation of the initial and equilibrium shapes of the droplet on a flat surface with static contact angle is shown in Fig. 4. Table II lists the physical properties of the system⁵⁰.

For initialization, a droplet with radius $R_0 = 1 \cdot 10^{-3}$ m is placed on a smooth flat surface such that its center is at the distance of the initial droplet radius R_0 from the surface. The computational domain is of size $0.004 \times 0.004 \times 0.004 \text{m}^3$. Since the initial contact angle is different from the

equilibrium contact angle, the droplet will start spreading until it reaches its equilibrium shape. Due to absence of gravity in this case, the Eötvös number, which describes the ratio between gravitational and capillary forces, is zero, $Eo := \Delta\rho gR_0^2/\sigma = 0$. The no-slip boundary condition is applied at the bottom boundary with free-slip boundary conditions being applied on every other boundary.

2. Model Calibration

In order to calibrate the underlying diffuse-interface model for all subsequent simulations, we determine the minimum number of cells $N_C := 4\frac{\varepsilon}{d_x}$ (where d_x is the cell size at the interface) required to sufficiently resolve the diffuse interface and the highest Cahn number $Cn := \frac{\varepsilon}{D_0}$, which relates the capillary width to reference length scale, that correctly models interface dynamics. Here, the spreading diameter is investigated for various values of the above-mentioned parameters.

Too low numbers of cells N_C to resolve the diffuse interface results result with non-physical interface evolution, and consequently wrong spreading diameters as can be seen in Fig. 5. We show the evolution of the dimensionless spreading diameter S/D_0 as a function of the dimensionless time t/τ with $\tau := \sqrt{\rho R_0^3/\sigma}$, where σ is the surface tension coefficient, for a contact angle $\theta_0 = 60^\circ$ and $Cn = 0.02$, with varying N_C .

From this, we conclude that at least six cells are required to resolve the interface sufficiently, which is in accordance our previous study⁴⁸ where simulations of a rising bubble were performed.

Fixing $N_C = 6$, the effect of the Cahn number can be studied. We have varied the Cahn number as $Cn \in \{0.01, 0.02, 0.04\}$. Results are shown in Fig. 6. As the Cahn number decreases, the simulations start to converge. More specifically, Yue³⁰ showed that for $Cn \leq 0.02$ the simulated results are independent of Cn . Thus, we choose $Cn = 0.02$ to calculate the value of the capillary width ε that is used in simulations.

Fixing $Cn = 0.02$, the final parameter to be determined is the scalar mobility M , cp. (1). Yue et al.³⁰ have shown that the mobility should be adjusted by a scaling formula. The mobility used in our simulations can be calculated based on $Cn = 4S = 4\sqrt{M\mu_e}/D_0$, where $\mu_e = \sqrt{\mu_1\mu_2}$ is the effective viscosity, which is used due to the highly dissimilar viscosities. Here, S reflects the diffusion length scale at the contact line³⁰.

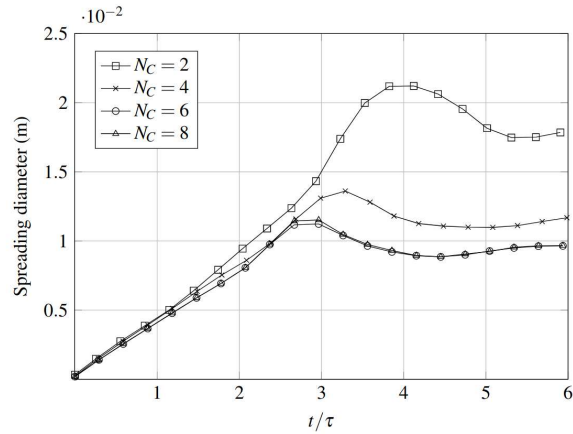


FIG. 5: Influence of the interface resolution on the droplet spreading diameter.

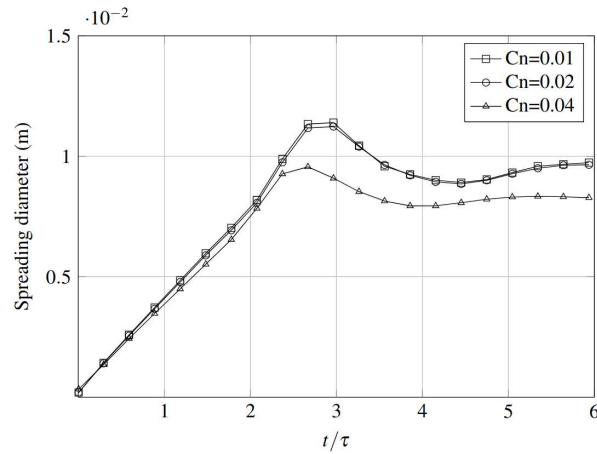


FIG. 6: Influence of the Cahn number on the droplet spreading diameter.

3. Spreading Dynamics

The spreading of a droplet has two stages – an initial stage where inertial-capillary forces are controlling droplet motion and a second stage where spreading is dominated by viscous forces. It has been observed that the spreading radius follows a power-law scaling in time⁵⁴,

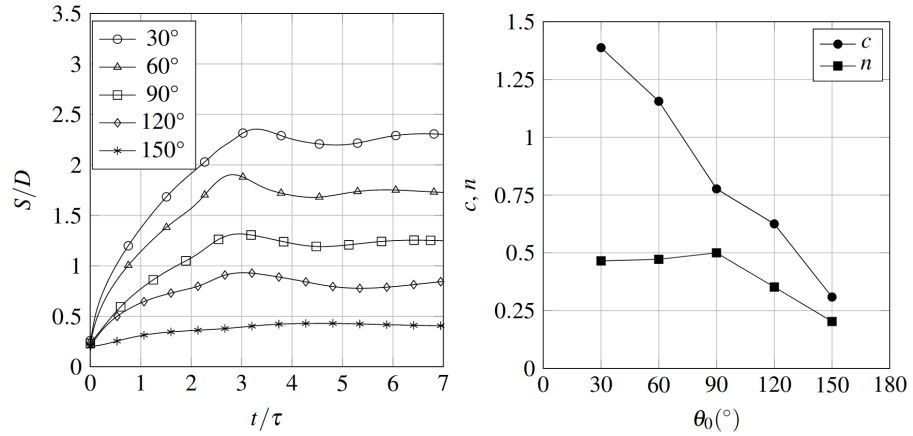


FIG. 7: Evolution of the equivalent spreading diameter (left) and the variation of the pre-factor c and exponent n (right) for various equilibrium contact angles.

$$\frac{S}{D} = c(t/\tau)^n, \quad (37)$$

where S is the spreading diameter, c is a scaling factor which depends on equilibrium contact angle and n is a scaling exponent, which has been observed by Winkels et al.⁵⁵ to not be influenced by wetting properties. Other authors^{54,56} have seen that the contact angle does influence the scaling exponent, and report that it decreases with increasing contact angle. Das et al.⁵⁷ have noted that this discrepancy may be due to the fact that system's properties are different and as such, the contribution of the viscous forces is changed with each study.

We investigate the variation of the normalized spreading diameter for five values of equilibrium contact angles, $\theta_0 \in \{30, 60, 90, 120, 150\}^\circ$. The equivalent spreading diameter S/D is displayed in Fig. 7a). Fig. 7b) shows the variation of n and c when changing the equilibrium contact angle.

By fitting Eq. (37) to the monotonic regime of data points obtained used in Fig. 7a), the values of wetting pre-factor c and the scaling exponent n have been computed for the various contact angles, both of which are influenced by the changes in equilibrium contact angle θ_0 , shown in Fig. 7b).

We have found that n decreases linearly with increasing θ_0 , except for contact angles lower than 90° , where the exponent's value stabilizes at $n \approx 1/2$. This agrees with the observations by Bianco

et al.⁵¹, who conducted experiments of water droplets spreading on treated glass plates. Bird et al.⁵⁴ observed a similar behaviour, where they have seen the scaling exponent monotonically decreases with increasing equilibrium contact angle.

Despite this, the results obtained by us and the previously mentioned authors do not agree with the observation made by Legendre et al.⁵⁶ where numerical simulations of spreading droplets were performed and Das et al.⁵⁷ who investigated the spreading behaviour of droplets over a bundle of fibres: they found that n is independent of θ_0 .

Das et al.⁵⁷ have used the Laplace number $La := \sigma \rho R_0 / \mu^2$, where μ is the dynamic viscosity of the oil droplet, which relates the inertial and surface tension forces to viscous forces, to explain these discrepancies. They have adopted the hypothesis that for $La \sim 10^1$ and lower, the effect of the contact angle on the spreading dynamics was negligible. Legendre et al.⁵⁶ showed that n varies from $2/3$ to $1/2$ when La varies from 10^0 to 10^4 , for a contact angle of 65° .

For our simulation setup, $La \sim 10^2$, which could indicate that for these Laplace numbers and for non-wetting liquids ($\theta_0 < 90^\circ$), the scaling exponent value is close to $1/2$, as it is seen in Fig. 7b). Moreover, in the studies of Bird et al.⁵⁴, it was observed the scaling exponent gives values close to $1/2$ for $La \sim 10^2$, much like the results we obtain.

Regarding the pre-factor c , it demonstrated that it also decreases with increasing contact angle, which was also noted in [54, 56, 55, 57].

One should note that the droplet's spreading diameter is not zero upon initialization. This is due to grid resolution in our numerical simulation, causing an overlap between the droplet and the surface. This can be fixed by simply increasing the grid resolution such that $S/D(t/\tau = 0)$ tends to zero. Nevertheless, we have shown that our simulated results agree with experimental observations, by capturing the scaling $S/D \sim \tau^n$ where n varies from $\sim 1/2$ to $\sim 1/4$, across the various equilibrium contact angles chosen.

4. Equilibrium Shapes

The equilibrium shape of the droplet spreading in the absence of gravity can be derived analytically, where the equilibrium contact radius r_f , curvature radius R_f and droplet height h_f are calculated from⁵⁰

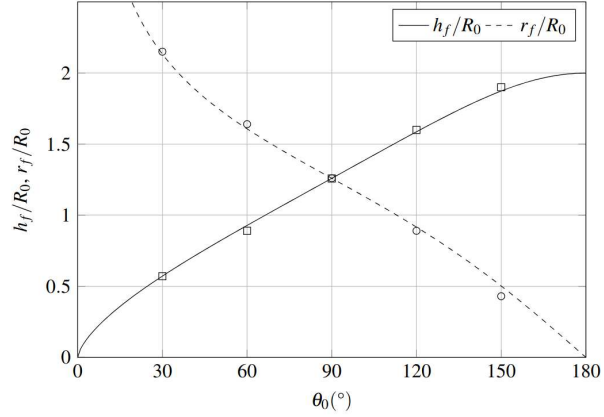


FIG. 8: Comparison of analytical and simulated equilibrium shape of a droplet spreading on a flat surface, for contact angles of 30°, 60°, 90°, 120° and 150°.

$$\Omega_L = \frac{4}{3}\pi R_0^3 = \pi R_f^3 \left(\frac{2}{3} - \cos(\theta_0) + \frac{1}{3} \cos^3(\theta_0) \right) \quad (38a)$$

$$r_f = R_f \sin(\theta_0) \quad (38b)$$

$$h_f = R_f (1 - \cos(\theta_0)) \quad (38c)$$

Fig. 8 displays the characteristic radii and heights of the droplets from simulations against the ones obtained analytically, for the same equilibrium contact angles. The results show a very good agreement between simulated and analytical results, also substantiating that the parameter values for N_C , C_n and M are appropriate.

B. Droplet spreading on a spherical surface

For further validation, we consider a case of particular relevance for spreading on non-planar substrates such as fibres: we perform simulations to study the equilibrium shapes of droplets spreading on a spherical surface.

As shown in Fig. 9, a solid sphere with a radius equal to the droplet radius is introduced in the centre of the previous computational domain. The droplet is initialized in such a way that its center is at a distance equal to R_0 from the spherical surface, just touching it. Since the initial contact

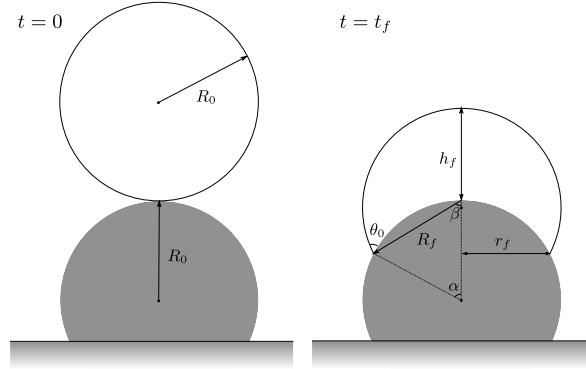


FIG. 9: Schematic representation of the initial (left) and equilibrium (right) shapes of the a droplet on a curved surface with static contact angle, in the absence of gravity.

angle is different from the static contact angle, the droplet will spread until it reaches equilibrium. Physical properties of the system are the same as in the previous section.

The equilibrium shapes of droplets on spherical surfaces can be obtained by solving the following non-linear system⁵⁰:

$$\alpha + \beta = 180 - \theta_0 \quad (39a)$$

$$\frac{4}{3}\pi R_0^3 = \frac{\pi R_f^3}{3}(1 + \cos(\beta))^2(2 - \cos(\beta)) + \frac{\pi R_0^3}{3}(1 + \cos(\alpha))^2(2 - \cos(\alpha)) - \frac{4}{3}\pi R_0^3 \quad (39b)$$

$$r = R_f \sin(\beta) = R_0 \sin(\alpha) \quad (39c)$$

$$h = R_f(1 + \cos(\beta)) - R_0(1 - \cos(\alpha)) \quad (39d)$$

For the five contact angles considered, the simulated results of the characteristic dimensions of the spreading droplet are compared with the ones obtained analytically, as shown in Fig. 10. Simulation results are in very good agreement with analytical results.

C. Droplet spreading on fibre strands

In a final validation study we investigate the equilibrium shape of droplets spreading on a fibre. The unduloidal shape of a wetting droplet on a fibre cannot be describe with simple analytical equations. Despite this, looking at the asymptotic regimes of very large droplets ($\Omega \gg d_v^3$) and

This is the author's peer reviewed, accepted manuscript. However, the online version of record will be different from this version once it has been copyedited and typeset.

PLEASE CITE THIS ARTICLE AS DOI: 10.1063/1.50131032

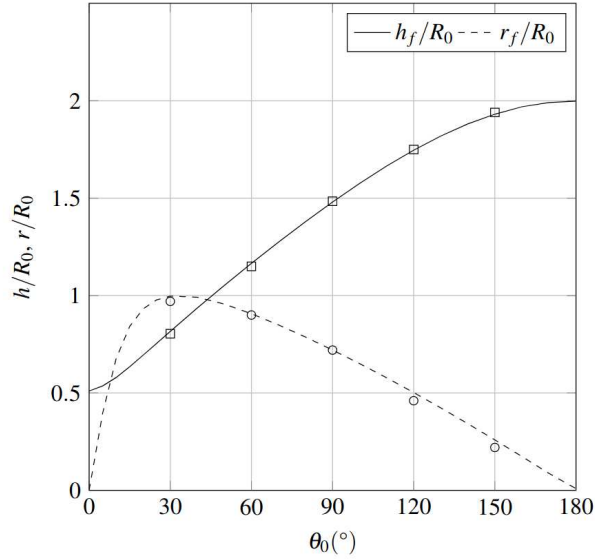


FIG. 10: Comparison of analytical and simulated equilibrium shape of a droplet spreading on a spherical surface, for contact angles of 30°, 60°, 90°, 120° and 150°.

very small ones ($\Omega \ll d_v^3$), where Ω is the droplet volume and d_v is the fiber diameter, one can derive analytical results of the full transition region between these two cases^{15,52}.

Large droplets tend to keep their spherical shape when they are placed on a fibre, thus $W \approx R_0$, with W being the system width and R_0 the deposited droplet diameter. For small droplet sizes, the droplet spreads on the fibre in such a way that the curvature of its interface is only slightly lower than the fibre curvature $2/d_v$, for which a shape approximates to that of a cylinder. Gilet et al.¹⁵ have derived a asymptotics for these two scenarios, which are succinctly shown in Table III. Herein, X is the total length of the droplet.

With the asymptotics from Table III, the dimensions of both large and small droplets on a vertical fibre can be assessed quantitatively. Gilet et al.¹⁴ have demonstrated an excellent agreement between the theoretical and experimental results for various Ω/d_v^3 .

We perform simulations of droplets spreading on fibres for various Ω/d_v , where both the width W and extension X are compared to the asymptotic solutions – see Fig. 11, for a contact angle of 15°. It can be seen that the simulations results are in very good agreement with the theoretical

This is the author's peer reviewed, accepted manuscript. However, the online version of record will be different from this version once it has been copyedited and typeset.

PLEASE CITE THIS ARTICLE AS DOI: 10.1063/1.50131032

TABLE III: Scaling laws for the equilibrium shape of very large and very small droplets spreading on a fibre.

	length	width
(large) droplet size	$X = 2W$	$W = d_v \left(\frac{3\Omega}{4\pi d_v^3} \right)^{1/3}$
(small) droplet size	$X = d_v \pi$	$W = d_v \frac{8\Omega}{\pi^2 d_v^3}$

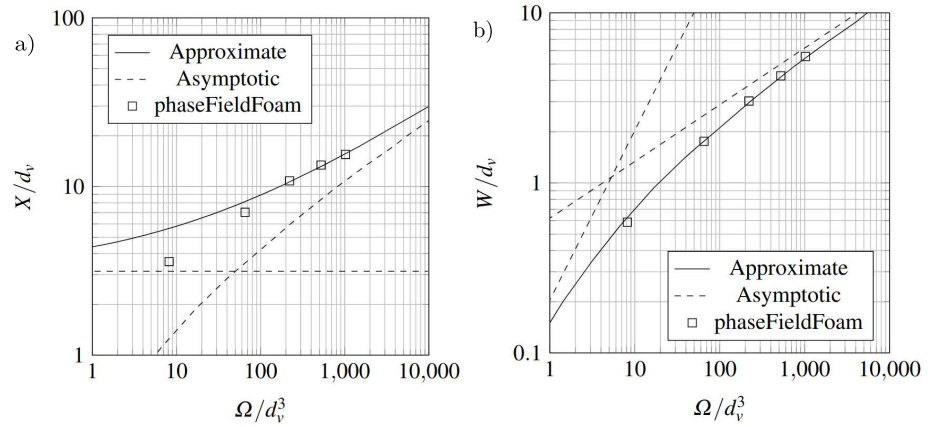


FIG. 11: Equilibrium shape of an axisymmetrical droplet spreading on a smooth fibre, for various droplet sizes smaller than the capillary length (≈ 1.5 mm): (a) dimensionless Length and (b) dimensionless width. The dashed lines represent the asymptotic solutions, see Table III. The solid lines refer to the approximate solution corresponding to an unduloid droplet shape¹⁵.

predictions, substantiating the capability of our solver to predict the equilibrium shapes of large and small droplets spreading on a fibre.

V. Motion of droplets on a vertical fibre strand

Varying the droplet's volume and viscosity, we study the terminal velocities of droplets moving on a vertical fibre strand, their accelerations and also the viscous energy dissipation rates during the

TABLE IV: Physical properties of fluids.

property	oil	air
density (kg/m^3)	950	1
kinematic viscosity (m^2/s)	$1\text{e-}5$, $2\text{e-}5$	$1.5\text{e-}6$
surface tension (N/m)	0.02	

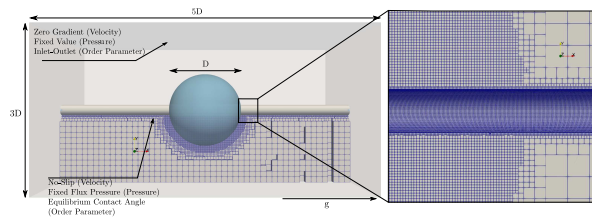


FIG. 12: Computational domain and adaptive mesh refinement.

early stages of motion. Table IV lists the physical properties of the oil-air system.

The computational setup for the present problem is shown in Fig. 12, where a droplet is placed onto a fibre. The same boundary conditions have been used for the sides of the domain, and for the fiber, a no-slip boundary condition is employed, as shown in Fig. 12. We consider droplets placed on smooth, chemically homogeneous and heterogeneous fibres of diameter $d_f = 200\mu\text{m}$. Local insights are gained by evaluating the volumetric energy densities in particular regarding viscous dissipation. To reduce the computational effort, the solver has also been enhanced to use the moving reference-frame technique as described in Section III C. Furthermore, an adaptive mesh refinement technique has been employed, where we use refinement criteria based on the order parameter so as to dynamically refine the mesh at the interface and inside the liquid phase.

A. Motion on homogeneous fibres

The motion of droplets is governed by viscous and capillary forces (neglecting charge effects here), where the viscous force F_v arises due to viscous fluid flow inside the droplet and the capillary forces F_c originates due to the capillarity of the interface and the difference of its advancing and receding contact angles at the contact line. With this, one can analyse the equation of motion of

a sliding droplet. On a vertical fibre strand, the motion of a droplet with volume Ω and density ρ_L is driven by the gravitational force $\mathbf{F}_g = F_g \hat{\mathbf{e}}_g$ of constant magnitude $F_g = \rho_L \Omega g$, where $\hat{\mathbf{e}}_g$ is the unit vector in direction of gravity and $g = \|\mathbf{g}\| = 9.81 \text{ m/s}^2$ is the magnitude of the gravitational acceleration. The component of the full equation of motion in direction of gravity is

$$\rho_L \Omega \frac{dU_p}{dt} = \rho_L \Omega g - F_v + F_c \quad (40)$$

Here, $F_v = -\mathbf{F}_v \cdot \hat{\mathbf{e}}_g$ and $F_c = \mathbf{F}_c \cdot \hat{\mathbf{e}}_g$ are components of the viscous and capillary forces, respectively. Note, that the sign of the viscous force in Eq. (40) is taken negative by convention as this force is expected to act opposite to the direction of droplet motion and gravity. The sign of the capillary force F_c can be positive or negative, as the capillary force may act along or against the direction of gravity.

To gain further insights, we investigate the rate at which work is done on a fluid element in the droplet while moving on the fibre strand changing its shape and volume. In general,

$$\boldsymbol{\sigma} : \nabla \mathbf{u} = -p \nabla \cdot \mathbf{u} + \boldsymbol{\tau} : \nabla \mathbf{u}, \quad (41)$$

where $\boldsymbol{\sigma} = -p\mathbf{I} + \boldsymbol{\tau}$ with $p = -\frac{1}{3} \text{tr} \boldsymbol{\sigma}$ denotes the total stress tensor, with p being the mechanical pressure. Since we assume isochoric flow, $\nabla \cdot \mathbf{u} \equiv 0$, we are left with the so-called dissipation function,

$$\phi := \boldsymbol{\tau} : \nabla \mathbf{u}. \quad (42)$$

Assuming a liquid of Newtonian fluid rheology, we can compute the total dissipation rate within the moving droplet, viz.

$$\varepsilon_\phi = \int_{\Omega} \phi dV. \quad (43)$$

With this, the viscous force in (40) can be approximated as

$$F_v = \frac{\varepsilon_\phi}{U_p}, \quad (44)$$

where U_p is the droplet barycenter velocity.

The capillary force F_c in (40) is computed from

$$\mathbf{F}_c = \int_{\partial\Omega} \lambda \partial_n C \nabla C dS, \quad (45)$$

i.e. the force the diffuse interface exerts on the substrate surface $\partial\Omega$ due to its capillarity⁵⁸.

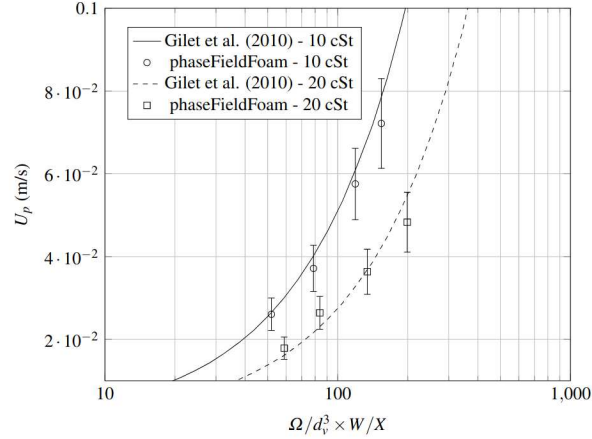


FIG. 13: Comparison between correlation (46) and results from simulations regarding the terminal velocity of a droplet sliding on a smooth fibre for various droplet volumes and viscosities.

1. Droplet velocity

Due to the small size of the fibre (and thus small contact line perimeter), the effect of capillary force is assumed to be negligible and the droplet motion is controlled by the effect of viscous forces. Based on this, Gilet et al.¹⁵ have proposed a correlation for the droplet's velocity as a function of the normalized volume, for a highly wetting liquid, viz.

$$U_p = \frac{1}{\alpha \pi C_v} \frac{g d_v^3}{\nu} \frac{W}{X} \frac{\Omega}{d_v^3}, \quad (46)$$

where C_v is a proportionality factor that accounts for the effect of surface tension. For a liquid spreading on a dry surface Hoffman⁵⁹ showed that $\alpha = 15$, which is used here to predict the droplets' terminal velocity. One should note that despite the complex dependence of W/X with Ω/d_v^3 , for sufficiently large ratios of Ω/d_v^3 , one finds that $W/X \rightarrow 0.5$ ⁵².

Simulation results of the terminal droplet velocities are shown to be in very good agreement with the correlation (46), for all considered droplet volumes and viscosities, as seen in Fig. 13. For our simulations, the equilibrium contact angle has been set to $\theta_0 = 15^\circ$.

Fig. 14 displays the temporal evolution of the droplets' barycenter velocities. Overshoots in ve-

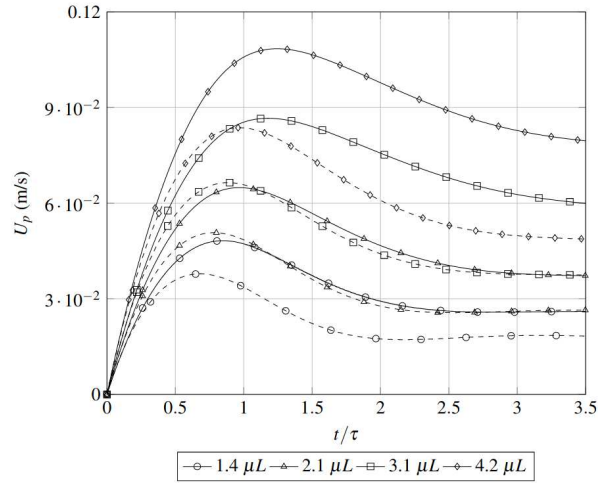


FIG. 14: Velocity profiles of a droplet moving on a smooth substrate, for various droplet volumes and viscosities. Full lines represent the high viscosity case of 20 cSt, dashed ones the low viscosity case of 10 cSt.

locities are observed at $t \sim 1$ ms, after which the velocities decrease and reach quasi-steady-state values.

The times it takes for droplets to reach their respective quasi-steady-state velocities have also been evaluated. Gilet et al. have proposed that the terminal velocity can be estimated using (46), where $t_{s-s} \sim U_p/g$. Our results show that the actual times to achieve steady-state velocities are higher: we observe that $t_{s-s} \sim (U_p/g)^n$, with $n \approx 0.7$ resulting in a much better agreement with simulated results. This discrepancy may be caused by the way the droplet is initially placed onto the fibre in experiments compared to how it is initialized for simulations. Moreover, the equilibrium contact angle used in simulations may not be the same as the one observed experimentally, which would affect the time to reach quasi-steady-state motion.

2. Viscous Dissipation & Viscous Force

Gilet's assumption proposes that the droplet motion is governed by viscous forces, making it vital to study the viscous dissipation processes during the droplets' motion at the fibre strands in more

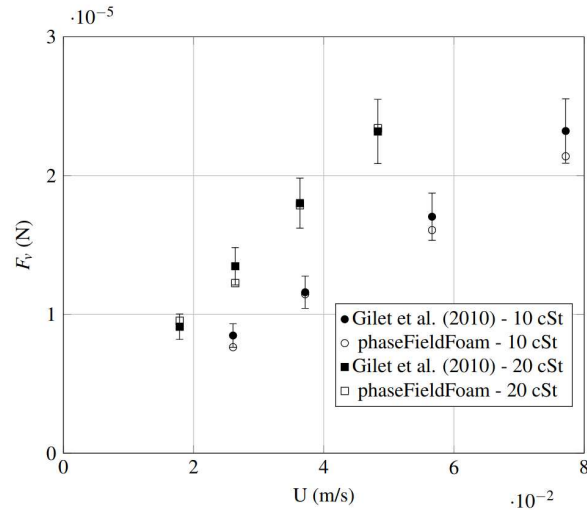


FIG. 15: Comparison of viscous forces obtained from correlation (47) and from simulation data, for various terminal velocities and viscosities.

detail. Several correlations to calculate the viscous force have been proposed in [15, 52, 60, and 61], we decide to use the one by [15] due to its simplicity,

$$F_v = \frac{1}{\alpha\pi C_v} \mu d_v \frac{X}{W} U_p, \quad (47)$$

where U_p is the droplets' terminal velocity.

Fig. 15 shows the viscous force as processed from simulation results over the droplets' velocities for kinematic viscosities of 10cSt and 20cSt, comparing it with the values obtained from (47), with the error bars indicating relative deviations of 10%.

A good agreement is observed. However, for the higher droplet velocities and for the lower viscosities the simulation results start to deviate slightly from the expected values.

To identify the processes which govern dynamic wetting of droplets on fibres, the viscous dissipation rate has been compared between simulations. Here, the dissipation arising from contact line relaxation is neglected⁶². Fig. 16 shows the rate of dissipation for a droplet moving on a fibre strand with an equilibrium contact angle $\theta_0 = 15^\circ$, for a dynamic viscosity of 10cSt and 20cSt.

Initially, the droplets experience very rapid spreading over the fibre, driven by the difference between the equilibrium and its initial contact angle. In this initial stage, the viscous dissipation

This is the author's peer reviewed, accepted manuscript. However, the online version of record will be different from this version once it has been copyedited and typeset.
 PLEASE CITE THIS ARTICLE AS DOI: 10.1063/1.50131032

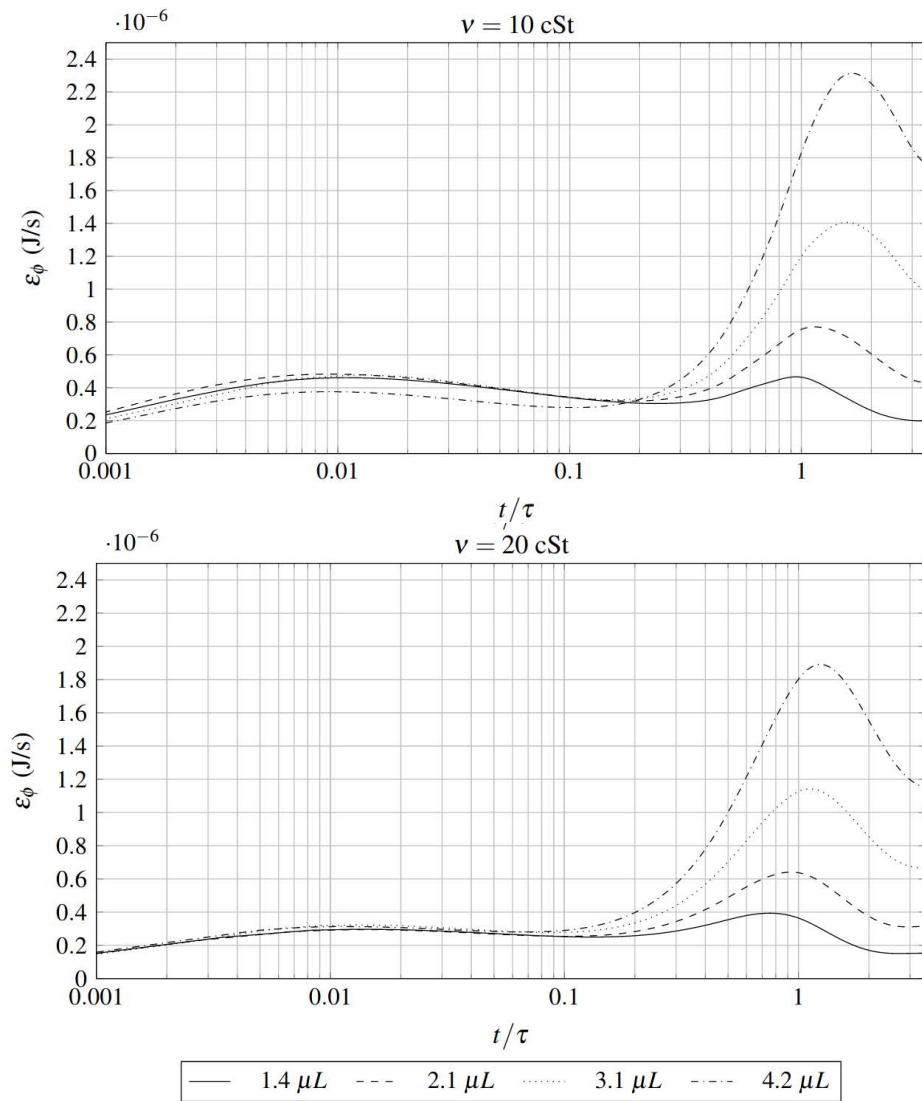


FIG. 16: Dissipation rates of a droplet moving on a fibre strand, for various droplet volumes and viscosities. A semi-logarithmic plot is used to include the evolution of the dissipation rate at the early stage of droplet motion.

increases very rapidly due to the formation of a small cusp at the contact line which has been also observed for the case of droplet spreading on flat substrates⁶³. Here we confirm the same phenomena extends to cylinder-shaped surfaces. One can also see that this behaviour is quite similar for the various droplet volumes studied, only changing when the viscosity is also varied, which may indicate that the cusp formation is not significantly affected by the droplet volume as it happens over a very short span of time and it may be only influenced by the physical properties of the fluid and equilibrium contact angle.

After the initial spreading stage, the dissipation rate will increase up to a maximum and then decreases to a lower constant value, when the droplet reaches quasi-steady-state. We observe that the dissipation rate is larger the larger the droplets, which is expected due to their larger terminal velocities. Interestingly, simulations with the higher viscous oil (20 cSt) exhibit lower dissipation rates. This is because viscosity influences the fluid velocity (cp. (46)), and a more viscous fluid will have a lower velocity in average, leading to lower dissipation rates at the bulk and wedge. Furthermore, this lower velocity promotes lower X/W ratios, which also contributes to the lower dissipation rate.

3. *Capillary Force*

To verify or falsify the assumption the capillary force was negligible when compared to the viscous force, we compute the capillary force according to (45). Fig. 17 shows the capillary force that has been computed from our simulation results using (45), for all cases previously studied.

Looking at the capillary force, it is several orders of magnitude smaller than the viscous force and thus its contribution to the overall droplet motion is indeed negligible, as assumed by Gilet et al. Certainly, this is because the contact line perimeter is small, which is then reflected on the capillary force.

Since the perimeter of the contact line is kept the same, because the fibre diameter is also the same throughout simulations, the observed changes in the capillary force are only due to the difference in the advancing and receding contact angles which increases with increasing droplet volume (and thus velocities), leading to higher capillary forces⁶⁴. We also observe that lower viscosities in general lead to higher capillary forces.

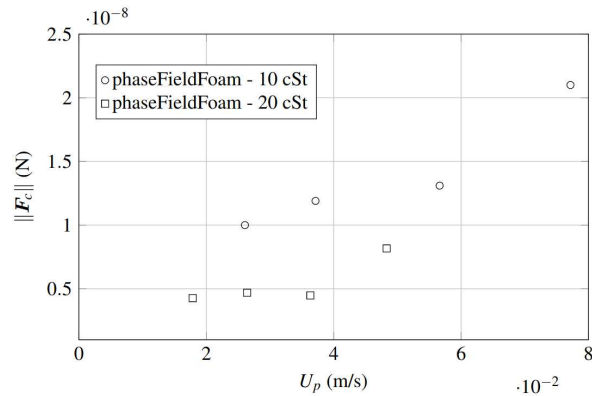


FIG. 17: Magnitude of the capillary force obtained for the various droplet volumes and viscosities.

B. Motion on chemically heterogeneous fibres

The focus of this study is to investigate the influence that locally varying wettability and also stripe periodicity have on the droplets' velocity profile, dissipation rate, viscous force and capillary force (which is assumed to be negligible compared to the viscous force), and quasi-steady-state motion.

To investigate the motion of droplets on chemically heterogeneous fibres, the same computational domain is used as depicted in Fig. 12. However, instead of applying a homogeneous wetting boundary condition with one equilibrium contact angle, the fibre's substrate is considered patterned with stripes of alternating wettability, where the equilibrium contact angle values have been locally varied between $\theta_0 = 55^\circ$ and $\theta_0 = 105^\circ$, respectively, as shown in Fig. 18. For the simulations, a droplet with volume $\Omega = 2.1 \mu\text{L}$ and $\nu_L = 10 \text{ cSt}$ is chosen.

Fig. 19 shows the velocity and dissipation rate profiles over time, as well as the gravitational, viscous and capillary forces. Figure 20 shows the evolution of the dissipation rate density and velocity vectors for the case with $\theta_0 \in \{55^\circ, 105^\circ\}$.

This is the author's peer reviewed, accepted manuscript. However, the online version of record will be different from this version once it has been copyedited and typeset.
 PLEASE CITE THIS ARTICLE AS DOI: 10.1063/1.50131032

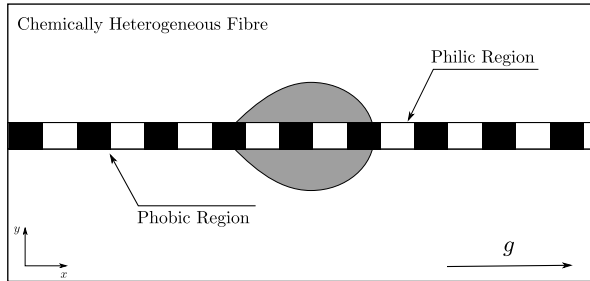


FIG. 18: Sketch of case setup, for an oil droplet sliding on a chemically patterned fibre in ambient air.

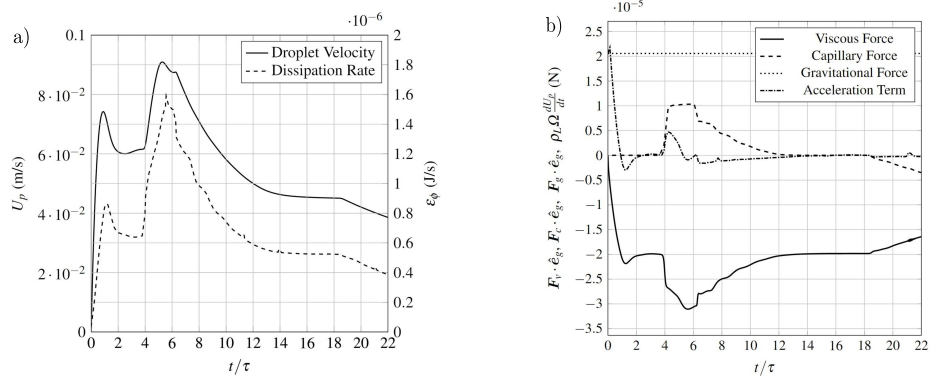


FIG. 19: Simulation of a droplet moving on a chemically patterned fiber: a) barycenter velocity, dissipation rate and b) viscous and capillary forces profiles, as well as the gravitational force and the acceleration term, calculated using (40).

This is the author's peer reviewed, accepted manuscript. However, the online version of record will be different from this version once it has been copyedited and typeset.
 PLEASE CITE THIS ARTICLE AS DOI: 10.1063/1.50131032

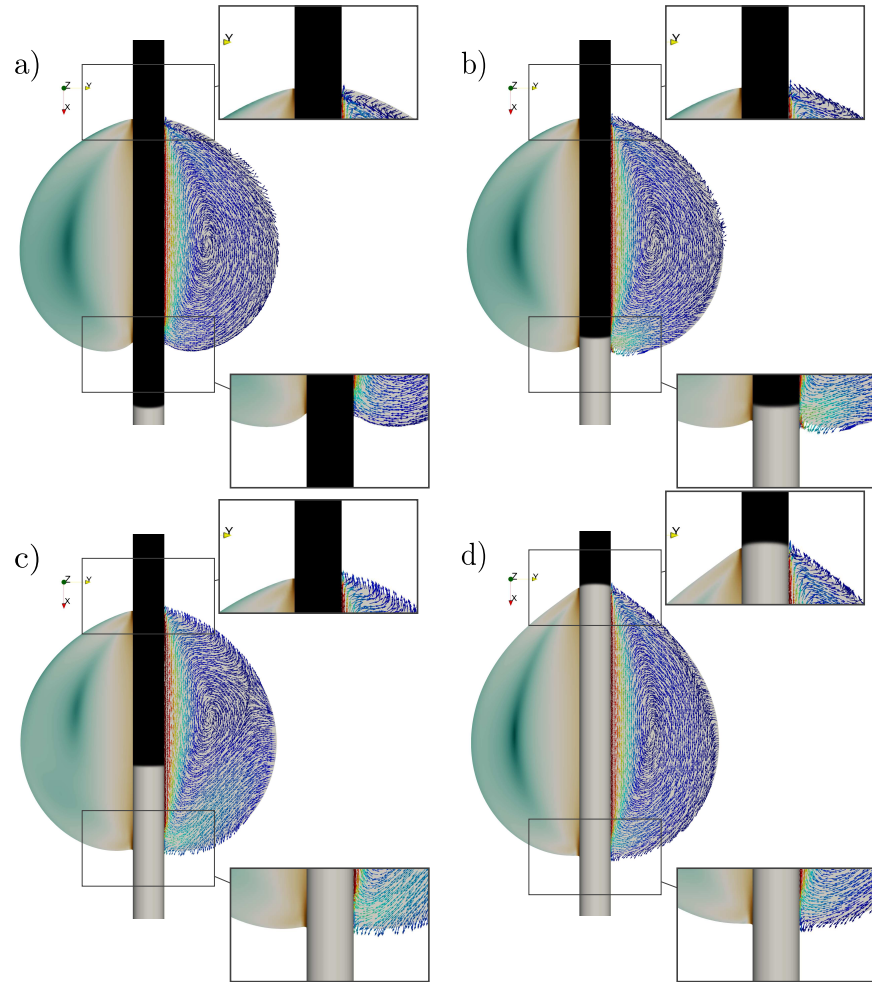


FIG. 20: Dissipation energy density and velocity vectors for the case with $\theta_0 \in \{55^\circ, 105^\circ\}$, at various dimensionless times: (a) $t/\tau = 2.80$, (b) $t/\tau = 4.05$, (c) $t/\tau = 4.40$, (d) $t/\tau = 8.05$, (e) $t/\tau = 12.80$, (f) $t/\tau = 18.65$.

This is the author's peer reviewed, accepted manuscript. However, the online version of record will be different from this version once it has been copyedited and typeset.

PLEASE CITE THIS ARTICLE AS DOI: 10.1063/1.50131032

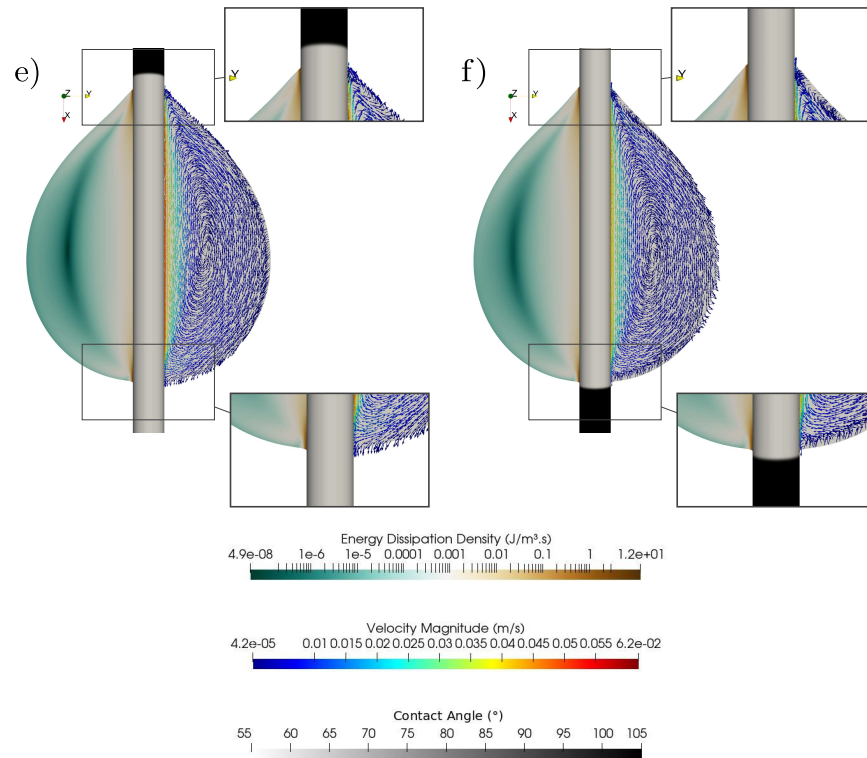


FIG. 20: Dissipation energy density and velocity vectors for the case with $\theta_0 \in \{55^\circ, 105^\circ\}$, at various dimensionless times: (a) $t/\tau = 2.80$, (b) $t/\tau = 4.05$, (c) $t/\tau = 4.40$, (d) $t/\tau = 8.05$, (e) $t/\tau = 12.80$, (f) $t/\tau = 18.65$. (cont.)

Comparing the dissipation rates depicted in Fig. 19 with the ones from Fig. 16, they are similar in the early stages of droplet motion – one observes a rapid increase of the dissipation rate due to the formation of a cusp during the initial spreading stage. The dissipation rate is biased when the transition from philic to phobic surfaces (and vice-versa) happens. Here, the capillary force may contribute to both droplet acceleration and deceleration, depending on the local contact angle and droplet shape at the contact line.

Initially, the droplet is moving exclusively on a phobic stripe, where an overshoot of the velocity and dissipation rate can be seen, at around $t/\tau = 1$. The change in the viscous force, being a function of the dissipation rate and velocity, will be similar. The capillary force at this stage is

orders of magnitude smaller than the viscous force. Following this overshoot, the droplet velocity will decrease until $t/\tau = 4$, where the front of the droplet passes through a philic stripe, forcing the front edge of the droplet to spread further. This can be seen as a rapid increase of both the velocity and dissipation rate as well as the viscous and capillary force. The magnitude of the capillary force is now much larger than before due to the deformation of the contact line. Since the front and rear of the droplet now have very different contact angles, contributions from the capillary force are larger. This increase in capillary force acts in the direction of the gravitational force, accelerating the droplet. At around $t/\tau = 6.5$, the rear edge of the droplet finally approaches the philic region. Since the spreading occurs in the direction that is opposite to the droplet motion, the droplet decelerates, which also leads to a decrease of the dissipation rate and viscous force. The capillary force will also decrease since the "hysteresis" effect is now much smaller than before, reaching values that are once again much smaller than the viscous force. At this stage, the capillary force contributes to the deceleration of the droplet, as the trailing edge is pulled in the direction opposite of gravity. At around $t/\tau = 18.5$, the front of the droplet will pass through a phobic region forcing the contact line region to bend, further decreasing the droplet's velocity and dissipation rate and increasing the capillary force due the increasingly different contact angles at the rear and front edges. The capillary force has contributed to the deceleration of the droplet.

This process repeats as the droplet is moving over the stripped patterns. Thus, its velocity will oscillate around its mean quasi-steady-state value. Thus, when compared to the homogeneous cases, the influence of the capillary force is indeed not negligible. Local deformations at the contact line as well as the difference in rear and front contact angles lead to larger values of the capillary force, which significantly affects the overall motion of the droplet.

To further investigate under which conditions the capillary force acts with or against the gravitational force, we decompose the contribution of the capillary force as

$$F_c = F_c^a + F_c^r, \quad (48)$$

where $F_c^a = \mathbf{F}_c^a \cdot \hat{\mathbf{e}}_g$ and $F_c^r = \mathbf{F}_c^r \cdot \hat{\mathbf{e}}_g$ are the capillary force contributions at the advancing and receding edge of the droplet. Fig. 21 shows the time evolution of both contributions to the capillary force. As the front edge passes to a philic region, the capillary force at the advancing and receding edges increases, which leads to a positive contribution to the capillary force in the direction of the droplet motion – accelerating the droplet. As the trailing edge of the droplet is also passing the philic region, starting at around $t/\tau = 6$, the receding contact line will move in the direction

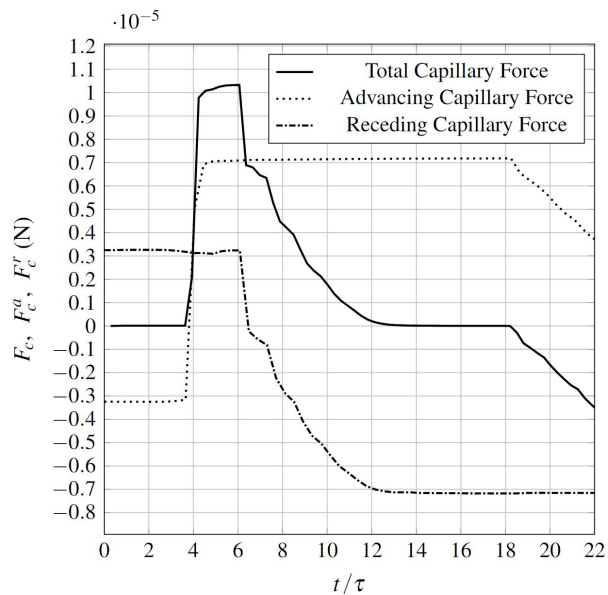


FIG. 21: Contribution of the capillary force at the leading and trailing edge during droplet motion.

opposite of the droplet motion, leading to the decrease of the receding capillary force. This leads to a decrease of the capillary force and thus the droplet decelerates, until it reaches a quasi-steady-state. At $t/\tau = 18.5$ the front edge passes to the phobic region. The decrease of the advancing capillary force decelerates the droplet once more.

We can infer that the value of the capillary force will be positive when the contact line accelerates in the direction of motion, making the droplet accelerate, and negative for a contact line that accelerates opposite to the direction of motion, decelerating the droplet. Moreover, one can see that since the droplet is initialized in the phobic region, the contribution of the capillary force at the front of the droplet is negative, and the capillary force at the rear is positive – this is the opposite in the philic region.

In order to also assess the accuracy of our force computation from DNS data, the right-hand-side (RHS) and left-hand-side (LHS) of (40) are calculated and compared – see Fig. 22. A good agreement between the terms in the RHS and LHS of (40) is observed, substantiating that the computation of the forces from DNS is reliable. A maximum deviation of about 38% occurs at the very early stages of motion, at around $t/\tau = 0.15$ - this can be attributed to the initialization

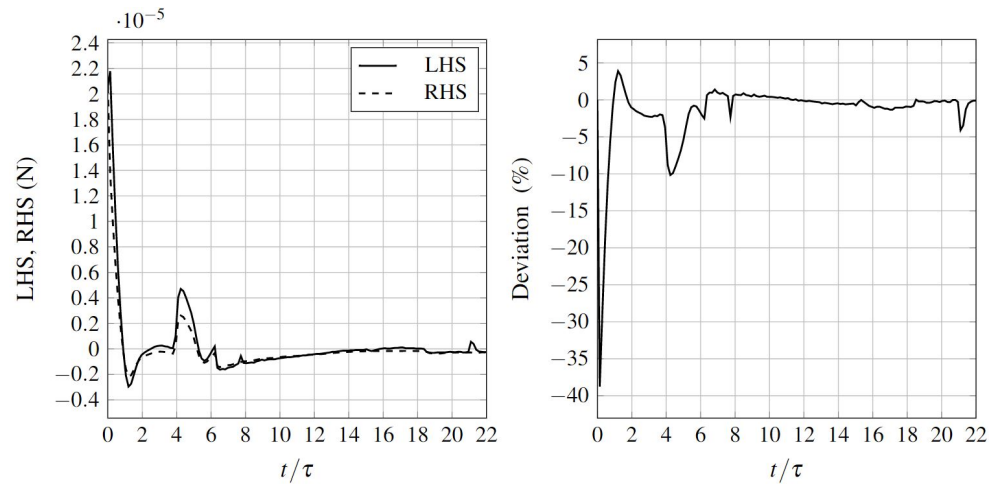


FIG. 22: Comparison between the RHS and LHS terms of Eq. (40) (left) and the deviation associated (right), for the case with $\theta_0 \in \{55^\circ, 105^\circ\}$.

setup, where an un-physical pressure field is initially used (assumed to be uniform and with a value of zero) and so the diffuse interface must first relax, which leads to a larger error at the onset of motion. Despite this, one more notable deviation occurs at $t/\tau = 4$, when the front edge of the droplet passes to the philic stripe. This deviation between the acceleration term and the sum of the forces can be attributed to the deviation from the tangent hyperbolic profile of the phase-field: as the front edge of the droplet passes to the philic stripe, the profile of the diffuse interface is deteriorated. Therefore, the interfacial profile can no longer be assumed to be of equilibrium tangent-hyperbolic shape. However, our analysis using Eq. (45) is based on this assumption. This explains the deviation in Fig. 22 to be largest at the point where the contact line passes the wettability step on the fibre surface. The faster this transition happens the more the deterioration of the equilibrium profile, and the greater the deviation. This is substantiated by the later droplet transition, at time $t/\tau = 18$, where the droplet velocity is lower and so is the deviation between LHS and RHS. Certainly, one could use the new relaxation model accounting for highly dynamic diffuse interface deformations³⁶, but this is not within the scope of this work and shall be subject to future research.

Since the focus here is to study the influence that chemical heterogeneities have on the droplet mo-

This is the author's peer reviewed, accepted manuscript. However, the online version of record will be different from this version once it has been copyedited and typeset.

PLEASE CITE THIS ARTICLE AS DOI: 10.1063/1.50131032

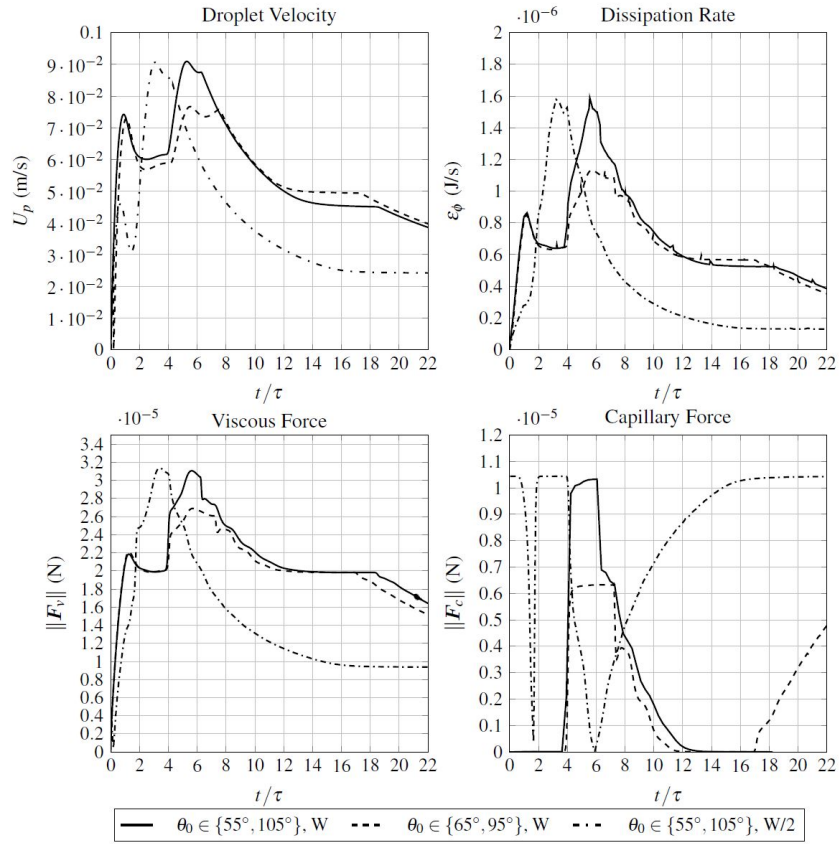


FIG. 23: Droplet velocity, dissipation rate and magnitude of viscous and capillary forces profile, for three cases of a droplet sliding down a chemically patterned fibre strand.

tion and the forces acting on the droplet, another case with $\theta_0 \in \{65^\circ, 95^\circ\}$ has been investigated, for the same stripe length in order to disclose the influence of the wettability range. Moreover, the periodicity of the stripes has been doubled, to investigate its effect on motion. Fig. 23 shows the sliding velocity and dissipation rate profiles during the simulation. Both the magnitude of the capillary force and viscous dissipation force profiles are shown.

From Fig. 23 it is evident that changing the wettability range influences sliding velocity, dissipation rate and the forces acting on the droplet significantly. For the case with $\theta_0 \in \{65^\circ, 95^\circ\}$, it can be seen that the profile of the plots resembles the ones for the case of $\theta_0 \in \{55^\circ, 105^\circ\}$. Because the

wettability range is now smaller when compared to the case with $\theta_0 \in \{55^\circ, 105^\circ\}$, the spreading motion of the droplet as it passes through the philic stripe is not as intense and the increase in sliding velocity is not as large. Conversely, this also leads to lower contact angle hysteresis and so the capillary force is slightly smaller as well. Since the contact angle of the philic region is larger as well, the droplet velocity becomes larger for the case with $\theta_0 \in \{65^\circ, 95^\circ\}$, which becomes noticeable at around $t/\tau = 8$. Thus, the front edge of the droplet will also reach the phobic region faster for the case of $\theta_0 \in \{65^\circ, 95^\circ\}$, at around $t/\tau = 17$. After this, the capillary force will once again increase to the values seen before (since the difference in contact angles is almost the same), although slower than previously because the contact line is also moving slower.

Another case where the same wetting range is used, but the periodicity of the stripes is doubled (by halving their length) is investigated. Initially, the rear and front edges of the droplet are in different regions, and the capillary force is initially large and has the same value as for the case initially described. Hence, the initial overshoot of the sliding velocity is smaller. The front of the droplet quickly encounters a philic stripe, forcing the advancing edge of the droplet to spread in the same way as for the case with the regular periodicity, just at a shorter time. Around the time the droplet velocity starts decreasing, the front edge passes through a phobic region, a decrease of velocity, dissipation energy and viscous force is observed. The capillary force steadily increases as the front edge slowly passes from the philic to the phobic region. Thus, the terminal droplet velocity is lower when compared to the other cases. Since the droplet velocity is so low, the viscous force will be smaller than the capillary force, which opposite to the assumption by Gilet et al.¹⁴. This showcases that the choice of surface chemistry can greatly affect the droplet's motion and shape and correlations must be applied with care.

VI. Summary and Outlook

We discuss the motion of droplets moving along vertically arranged, chemically homogeneous and heterogeneous fibres based on local insights gained by Direct Numerical Simulations. For this, we have utilized a diffuse interface phase-field method implemented in our in-house solver, phaseFieldFoam, in OpenFOAM (FOAM-extend 4.0/4.1). For validation, we compare (inter alia) the equilibrium shapes of droplets spreading on fibres with results obtained from analytical expressions, for various volume-to-fibre-diameter ratios.

For the homogeneous fibres we compare our simulation results regarding the terminal velocity and

the viscous force with existing correlations. We observe that simulation results are in very good agreement with these correlations. Moreover, we study the motion until the droplets have reached terminal velocities, where we observe an overshoot in the droplet velocity in the beginning for all situations. From our computational analysis, we could improve a correlation by Gilet et al.¹⁵ for the time until the droplets reach their terminal velocities. We further investigate the effect that the capillary force has on the overall droplet motion, and confirm the assumption made by Gilet et al. for cases of chemically homogeneous surfaces – that its influence is negligible when compared to the viscous dissipation. Eventually, the dissipation rates during the droplets' motion have been studied in detail. We observe a rapid increase in the dissipation rates, due to the formation of a cusp at the contact line. This observation holds for all volumes. For the less viscous liquid the dissipation rate is found to be larger than for the more viscous liquid.

For the heterogeneous fibres, we investigate the evolution of the dissipation rates, droplet velocities and viscous and capillary forces as the droplet slides through the phobic and philic regions. Here, surface chemistry has a significant influence on both the droplet's velocity and shape, as well as the forces that act on the droplet. Notably, we observed that the capillary force, which we showed to be negligible when compared to the viscous force for a droplet moving on a chemically homogeneous fibre, can reach values that are at the same order of magnitude, and in some cases larger than, as the viscous force. Thus, correlations must be applied with care in cases of chemically heterogeneous fibre substrates.

Acknowledgements

Funded by the Deutsche Forschungsgemeinschaft (DFG, German Research Foundation) - Project-ID 265191195 - SFB 1194

Data Availability

The data that support the findings of this study are available from the corresponding author upon reasonable request.

This is the author's peer reviewed, accepted manuscript. However, the online version of record will be different from this version once it has been copyedited and typeset.

PLEASE CITE THIS ARTICLE AS DOI: 10.1063/1.50131032

References

- ¹D. Chen, L. Tan, H. Liu, J. Hu, Y. Li, and F. Tang, "Fabricating superhydrophilic wool fabrics," *Langmuir* **26**, 4675–4679 (2009).
- ²S. Michielsen and H. J. Lee, "Design of a superhydrophobic surface using woven structures," *Langmuir* **23**, 6004–6010 (2007).
- ³P. Contal, J. Simao, D. Thomas, T. Frising, S. Callé, J. Appert-Collin, and D. Bémer, "Clogging of fibre filters by submicron droplets. phenomena and influence of operating conditions," *Journal of Aerosol Science* **35**, 263–278 (2004).
- ⁴S. U. Patel and G. G. Chase, "Separation of water droplets from water-in-diesel dispersion using superhydrophobic polypropylene fibrous membranes," *Separation and Purification Technology* **126**, 62–68 (2014).
- ⁵J. Plateau, *Statique expérimentale et théorique des liquides soumis aux seules forces moléculaires*, *Statique expérimentale et théorique des liquides soumis aux seules forces moléculaires* No. Bd. 1 (Gauthier-Villars, 1873).
- ⁶L. Rayleigh, "On the instability of jets," *Proceedings of the London Mathematical Society* **s1-10**, 4–13 (1878).
- ⁷D. H. Peregrine, "Free liquid jets and films: Hydrodynamics and rheology," *Journal of Fluid Mechanics* **312**, 408–409 (1996).
- ⁸I. L. Kliakhandler, S. H. Davis, and S. G. Bankoff, "Viscous beads on vertical fibre," *Journal of Fluid Mechanics* **429**, 381–390 (2001).
- ⁹R. V. Craster and O. K. Matar, "On viscous beads flowing down a vertical fibre," *Journal of Fluid Mechanics* **553**, 85 (2006).
- ¹⁰C. Duprat, C. Ruyer-Quil, S. Kalliadasis, and F. Giorgiutti-Dauphiné, "Absolute and convective instabilities of a viscous film flowing down a vertical fiber," *Physical Review Letters* **98** (2007), 10.1103/physrevlett.98.244502.
- ¹¹B. J. Carroll and J. Lucassen, "Effect of surface dynamics on the process of droplet formation from supported and free liquid cylinders," *Journal of the Chemical Society, Faraday Transactions 1: Physical Chemistry in Condensed Phases* **70**, 1228 (1974).
- ¹²B. Carroll, "The accurate measurement of contact angle, phase contact areas, drop volume, and Laplace excess pressure in drop-on-fiber systems," *Journal of Colloid and Interface Science* **57**, 488–495 (1976).

This is the author's peer reviewed, accepted manuscript. However, the online version of record will be different from this version once it has been copyedited and typeset.

PLEASE CITE THIS ARTICLE AS DOI: 10.1063/5.0131032

- ¹³B. J. Carroll, “Equilibrium conformations of liquid drops on thin cylinders under forces of capillarity. a theory for the roll-up process,” *Langmuir* **2**, 248–250 (1986).
- ¹⁴T. Gilet, D. Terwagne, and N. Vandewalle, “Digital microfluidics on a wire,” *Applied Physics Letters* **95**, 014106 (2009).
- ¹⁵T. Gilet, D. Terwagne, and N. Vandewalle, “Droplets sliding on fibres,” *The European Physical Journal E* **31**, 253–262 (2010).
- ¹⁶J. Bico and D. Quéré, “Self-propelling slugs,” *Journal of Fluid Mechanics* **467**, 101–127 (2002).
- ¹⁷A. L. Yarin, W. Liu, and D. H. Reneker, “Motion of droplets along thin fibers with temperature gradient,” *Journal of Applied Physics* **91**, 4751–4760 (2002).
- ¹⁸T. S. Chan, F. Yang, and A. Carlson, “Directional spreading of a viscous droplet on a conical fibre,” *Journal of Fluid Mechanics* **894**, A26 (2020).
- ¹⁹A. Ashari, T. Bucher, H. V. Tafreshi, M. Tahir, and M. Rahman, “Modeling fluid spread in thin fibrous sheets: Effects of fiber orientation,” *International Journal of Heat and Mass Transfer* **53**, 1750–1758 (2010).
- ²⁰H. Aziz, M. Amrei, A. Dotivala, C. Tang, and H. Tafreshi, “Modeling Cassie droplets on superhydrophobic coatings with orthogonal fibrous structures,” *Colloids and Surfaces A: Physico-chemical and Engineering Aspects* **512**, 61–70 (2017).
- ²¹H. Aziz, N. M. Farhan, and H. V. Tafreshi, “Effects of fiber wettability and size on droplet detachment residue,” *Experiments in Fluids* **59**, 122 (2018).
- ²²H. Aziz and H. V. Tafreshi, “Competing forces on a liquid bridge between parallel and orthogonal dissimilar fibers,” *Soft Matter* **15**, 6967–6977 (2019).
- ²³R. Shi, Y. Tian, and L. Wang, “Bioinspired fibers with controlled wettability: From spinning to application,” *ACS Nano* **15**, 7907–7930 (2021).
- ²⁴P. M. Gore and B. Kandasubramanian, “Heterogeneous wettable cotton based superhydrophobic janus biofabric engineered with PLA/functionalized-organoclay microfibers for efficient oil–water separation,” *J. Mater. Chem. A* **6**, 7457–7479 (2018).
- ²⁵H. Zhu, C. Zhang, N. Ma, M. Tao, and W. Zhang, “Surface wettability modification of amine-functionalized polyacrylonitrile fiber to enhance heterogeneous catalytic performance for aldol reaction in water,” *Applied Catalysis A: General* **608**, 117842 (2020).
- ²⁶P. Yue and J. J. Feng, “Wall energy relaxation in the Cahn–Hilliard model for moving contact lines,” *Physics of Fluids* **23**, 012106 (2011).

This is the author's peer reviewed, accepted manuscript. However, the online version of record will be different from this version once it has been copyedited and typeset.

PLEASE CITE THIS ARTICLE AS DOI: 10.1063/5.0131032

- ²⁷D. Jacqmin, “Calculation of two-phase Navier–Stokes flows using phase-field modeling,” *Journal of Computational Physics* **155**, 96–127 (1999).
- ²⁸D. Jacqmin, “Contact-line dynamics of a diffuse fluid interface,” *Journal of Fluid Mechanics* **402**, 57–88 (2000).
- ²⁹H. Ding, P. D. Speltz, and C. Shu, “Diffuse interface model for incompressible two-phase flows with large density ratios,” *Journal of Computational Physics* **226**, 2078–2095 (2007).
- ³⁰P. Yue, C. Zhou, and J. J. Feng, “Sharp-interface limit of the Cahn–Hilliard model for moving contact lines,” *Journal of Fluid Mechanics* **645**, 279–294 (2010).
- ³¹P. Yue, “Thermodynamically consistent phase-field modelling of contact angle hysteresis,” *Journal of Fluid Mechanics* **899**, A15 (2020).
- ³²V. Fink, X. Cai, A. Stroh, R. Bernard, J. Kriegseis, B. Frohnappel, H. Marschall, and M. Wörner, “Drop bouncing by micro-grooves,” *International Journal of Heat and Fluid Flow* **70**, 271–278 (2018).
- ³³X. Cai, H. Marschall, M. Wörner, and O. Deutschmann, “Numerical simulation of wetting phenomena with a phase-field method using OpenFOAM®,” *Chemical Engineering & Technology* **38**, 1985–1992 (2015).
- ³⁴M. Wörner, N. Samkhaniani, X. Cai, Y. Wu, A. Majumdar, H. Marschall, B. Frohnappel, and O. Deutschmann, “Spreading and rebound dynamics of sub-millimetre urea-water-solution droplets impinging on substrates of varying wettability,” *Applied Mathematical Modelling* **95**, 53–73 (2021).
- ³⁵N. Samkhaniani, A. Stroh, M. Holzinger, H. Marschall, B. Frohnappel, and M. Wörner, “Bouncing drop impingement on heated hydrophobic surfaces,” *Int. J. Heat Mass Transf.* **180**, 121777 (2021).
- ³⁶M. Bagheri, B. Stumpf, I. V. Roisman, C. Tropea, J. Hussong, M. Wörner, and H. Marschall, “Interfacial relaxation – crucial for phase-field methods to capture low to high energy drop-film impacts,” *International Journal of Heat and Fluid Flow* **94**, 108943 (2022).
- ³⁷L. Landau and E. Lifshitz, *Fluid Mechanics* (Cambridge University Press, 1959).
- ³⁸H. Abels, H. Garcke, and G. Grün, “Thermodynamically consistent, frame indifferent diffuse interface models for incompressible two-phase flows with different densities,” *Mathematical Models and Methods in Applied Sciences* **22**, 1150013 (2012).
- ³⁹J. W. Cahn and J. E. Hilliard, “Free energy of a nonuniform system. III. Nucleation in a two-component incompressible fluid,” *The Journal of Chemical Physics* **31**, 688–699 (1959).

This is the author's peer reviewed, accepted manuscript. However, the online version of record will be different from this version once it has been copyedited and typeset.

PLEASE CITE THIS ARTICLE AS DOI: 10.1063/1.50131032

- ⁴⁰B. Widom, *Capillarity and Wetting Phenomena: Drops, Bubbles, Pearls, Waves*, Vol. 57 (AIP Publishing, 2004) pp. 66–67.
- ⁴¹G. Tierra and F. Guillén-González, “Numerical methods for solving the Cahn–Hilliard equation and its applicability to related energy-based models,” *Archives of Computational Methods in Engineering* **22**, 269–289 (2014).
- ⁴²C. M. Elliott and A. M. Stuart, “The global dynamics of discrete semilinear parabolic equations,” *SIAM Journal on Numerical Analysis* **30**, 1622–1663 (1993).
- ⁴³D. J. Eyre, “Unconditionally gradient stable time marching the Cahn–Hilliard equation,” *MRS Proceedings* **529**, 39–46 (1998).
- ⁴⁴F. Guillén-González and G. Tierra, “On linear schemes for a Cahn–Hilliard diffuse interface model,” *Journal of Computational Physics* **234**, 140–171 (2013).
- ⁴⁵F. Moukalled, L. Mangani, and M. Darwish, *The Finite Volume Method in Computational Fluid Dynamics* (Springer International Publishing, 2016).
- ⁴⁶D. Deising, H. Marschall, and D. Bothe, “A unified single-field model framework for volume-of-fluid simulations of interfacial species transfer applied to bubbly flows,” *Chemical Engineering Science* **139**, 173–195 (2016).
- ⁴⁷H. Rusche, “Computational fluid dynamics of dispersed two-phase flows at high phase fractions,” Imperial College London **PhD Thesis** (2003).
- ⁴⁸X. Cai, M. Wörner, H. Marschall, and O. Deutschmann, “Numerical study on the wettability dependent interaction of a rising bubble with a periodic open cellular structure,” *Catalysis Today* **273**, 151–160 (2016).
- ⁴⁹X. Cai, M. Wörner, H. Marschall, and O. Deutschmann, “CFD simulation of liquid back suction and gas bubble formation in a circular tube with sudden or gradual expansion,” *Emission Control Science and Technology* **3**, 289–301 (2017).
- ⁵⁰H. Patel, S. Das, J. Kuipers, J. Padding, and E. Peters, “A coupled volume of fluid and immersed boundary method for simulating 3D multiphase flows with contact line dynamics in complex geometries,” *Chemical Engineering Science* **166**, 28–41 (2017).
- ⁵¹A.-L. Biance, C. Clanet, and D. Quéré, “First steps in the spreading of a liquid droplet,” *Physical Review E* **69**, 016301 (2004).
- ⁵²L. Lorenceau and D. Quéré, “Drops on a conical wire,” *Journal of Fluid Mechanics* **510**, 29–45 (2004).

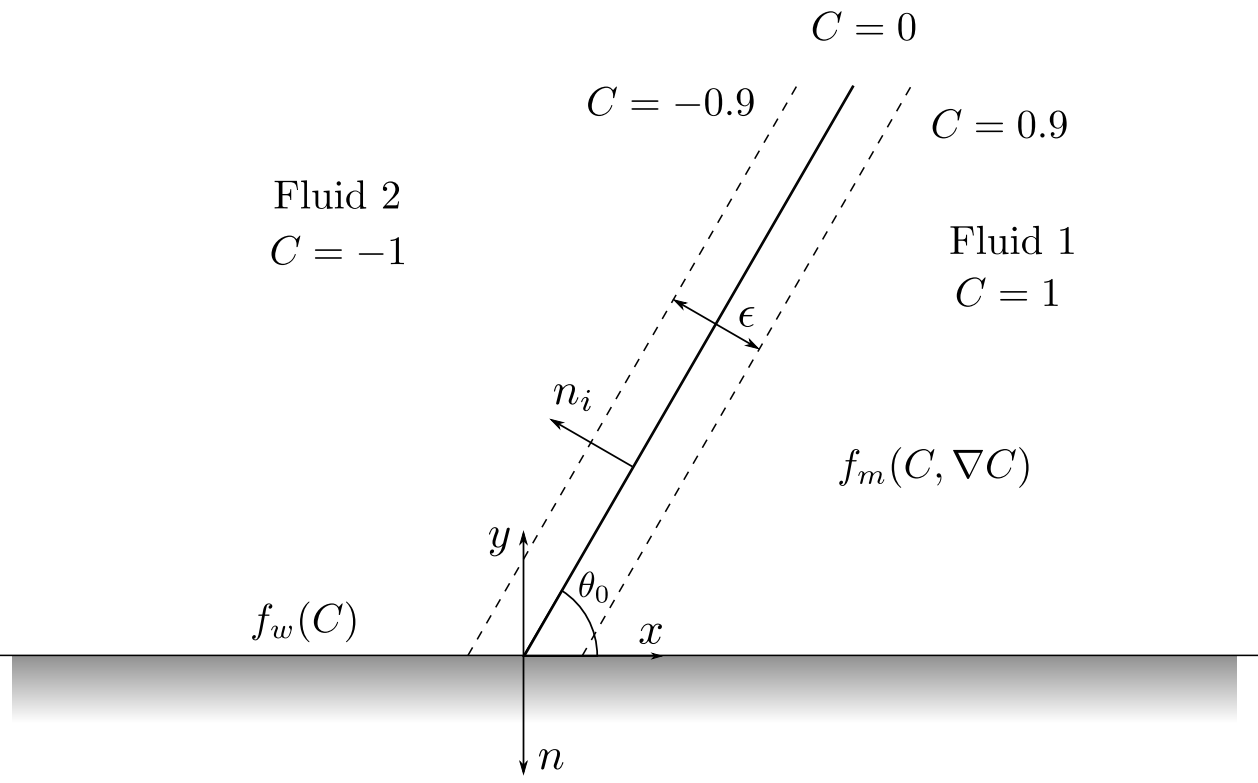
This is the author's peer reviewed, accepted manuscript. However, the online version of record will be different from this version once it has been copyedited and typeset.

PLEASE CITE THIS ARTICLE AS DOI: 10.1063/1.50131032

- ⁵³C. Galusinski and P. Vigneaux, “On stability condition for bifluid flows with surface tension: Application to microfluidics,” *Journal of Computational Physics* **227**, 6140–6164 (2008).
- ⁵⁴J. C. Bird, S. Mandre, and H. A. Stone, “Short-time dynamics of partial wetting,” *Physical Review Letters* **100**, 234501 (2008).
- ⁵⁵K. G. Winkels, J. H. Weijs, A. Eddi, and J. H. Snoeijer, “Initial spreading of low-viscosity drops on partially wetting surfaces,” *Physical Review E* **85**, 055301(R) (2012).
- ⁵⁶D. Legendre and M. Maglio, “Numerical simulation of spreading drops,” *Colloids and Surfaces A: Physicochemical and Engineering Aspects* **432**, 29–37 (2013).
- ⁵⁷S. Das, H. V. Patel, E. Milacic, N. G. Deen, and J. A. M. Kuipers, “Droplet spreading and capillary imbibition in a porous medium: A coupled IB-VOF method based numerical study,” *Physics of Fluids* **30**, 012112 (2018).
- ⁵⁸E. H. van Brummelen, M. Shokrpour-Roudbari, and G. J. van Zwieten, “Elasto-capillarity simulations based on the Navier–Stokes–Cahn–Hilliard equations,” in *Advances in Computational Fluid-Structure Interaction and Flow Simulation* (Springer International Publishing, 2016) pp. 451–462.
- ⁵⁹R. L. Hoffman, “A study of the advancing interface. i. interface shape in liquid—gas systems,” *Journal of Colloid and Interface Science* **50**, 228–241 (1975).
- ⁶⁰S. Dawar, H. Li, J. Dobson, and G. G. Chase, “Drag correlation of drop motion on fibers,” *Drying Technology* **24**, 1283–1288 (2006).
- ⁶¹S. Dawar and G. Chase, “Drag correlation for axial motion of drops on fibers,” *Separation and Purification Technology* **60**, 6–13 (2008).
- ⁶²A. Carlson, M. Do-Quang, and G. Amberg, “Dissipation in rapid dynamic wetting,” *Journal of Fluid Mechanics* **682**, 213–240 (2011).
- ⁶³J. Eggers, J. R. Lister, and H. A. Stone, “Coalescence of liquid drops,” *Journal of Fluid Mechanics* **401**, 293–310 (1999).
- ⁶⁴H. B. Eral, D. J. C. M. ’t Mannetje, and J. M. Oh, “Contact angle hysteresis: a review of fundamentals and applications,” *Colloid and Polymer Science* **291**, 247–260 (2012).

This is the author's peer reviewed, accepted manuscript. However, the online version of record will be different from this version once it has been copyedited and typeset.

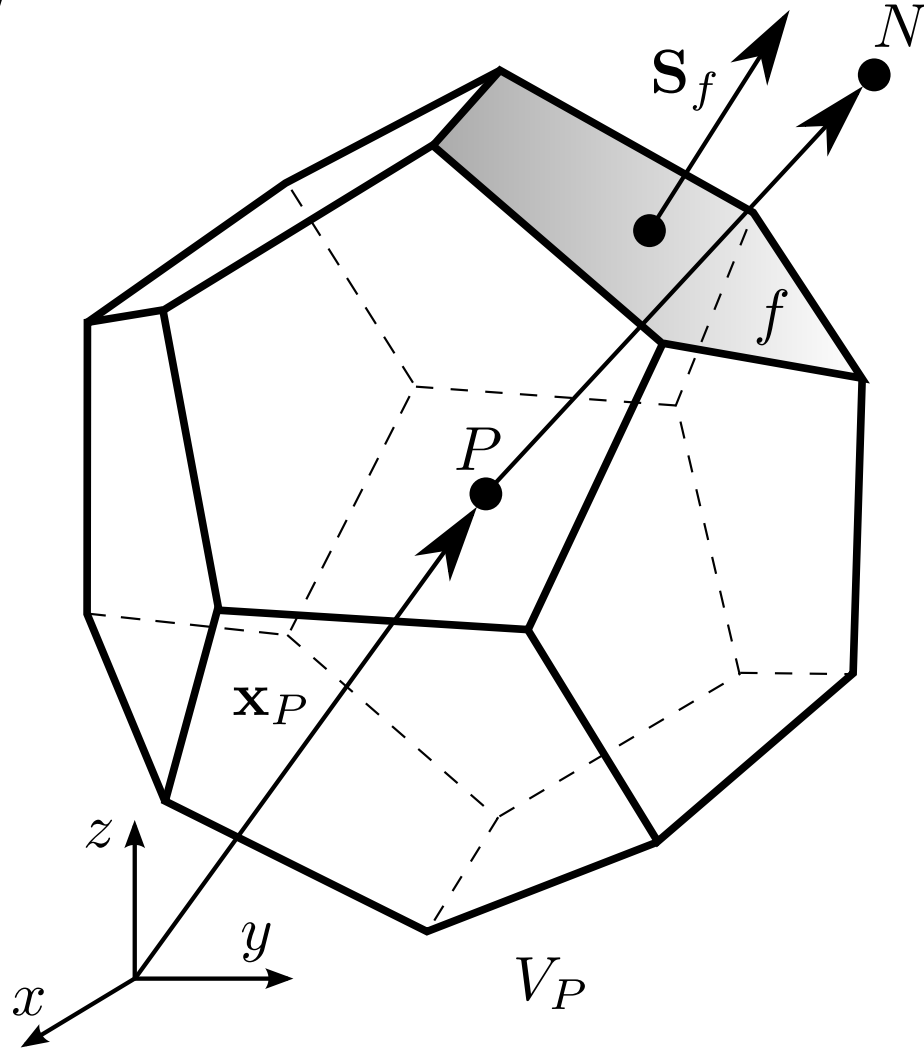
PLEASE CITE THIS ARTICLE AS DOI: 10.1063/1.50131032



This is the author's peer reviewed, accepted manuscript. However, the online version of record will be different from this version once it has been copyedited and typeset.

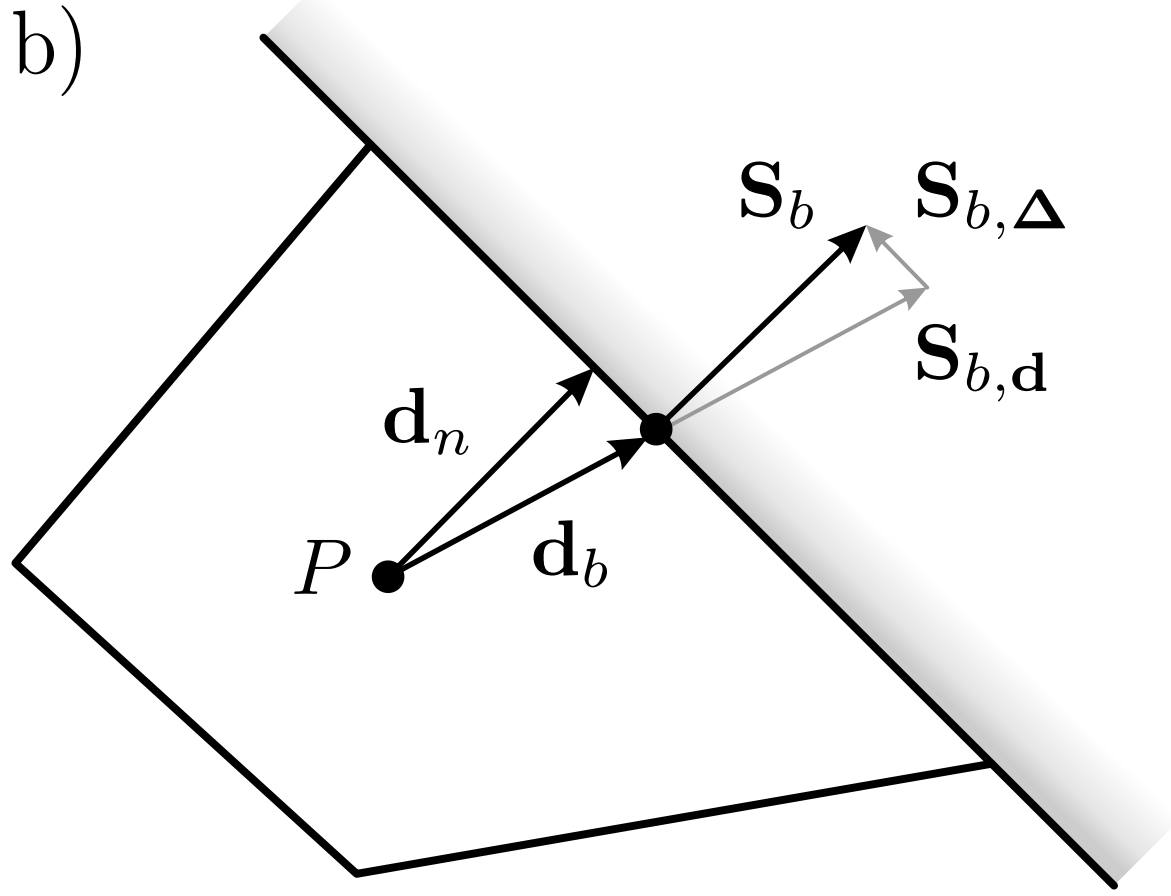
PLEASE CITE THIS ARTICLE AS DOI: 10.1063/5.0131032

a)



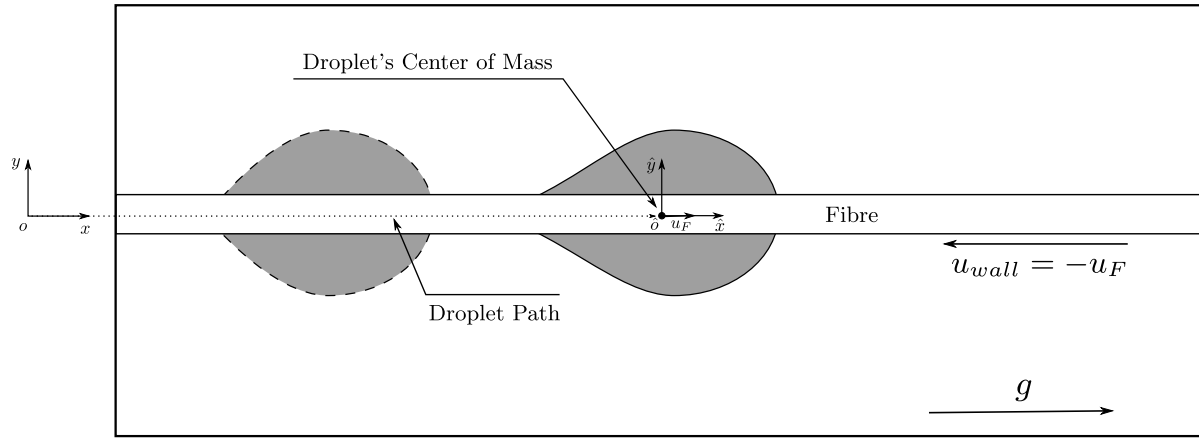
This is the author's peer reviewed, accepted manuscript. However, the online version of record will be different from this version once it has been copyedited and typeset.

PLEASE CITE THIS ARTICLE AS DOI: 10.1063/5.0131032



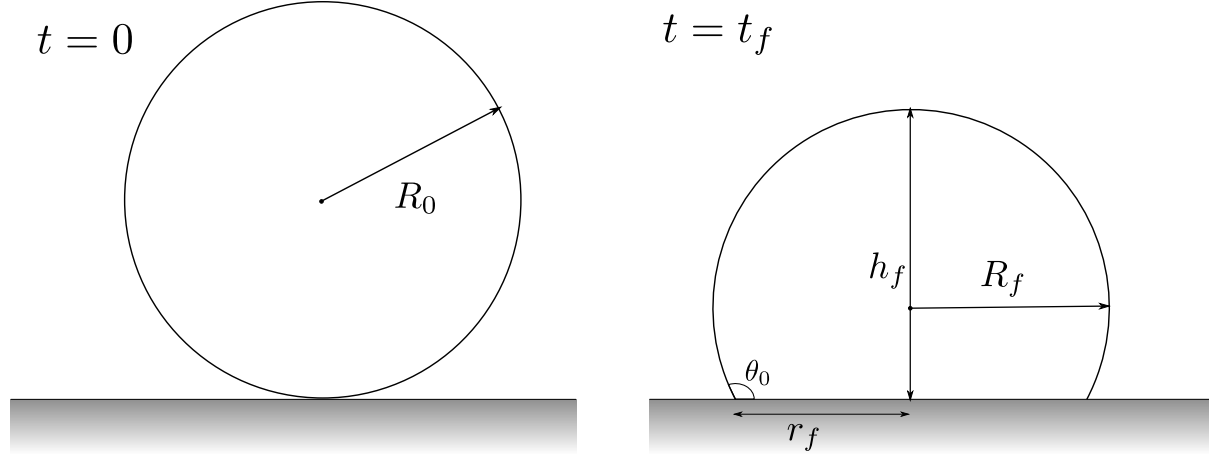
This is the author's peer reviewed, accepted manuscript. However, the online version of record will be different from this version once it has been copyedited and typeset.

PLEASE CITE THIS ARTICLE AS DOI: 10.1063/1.50131032



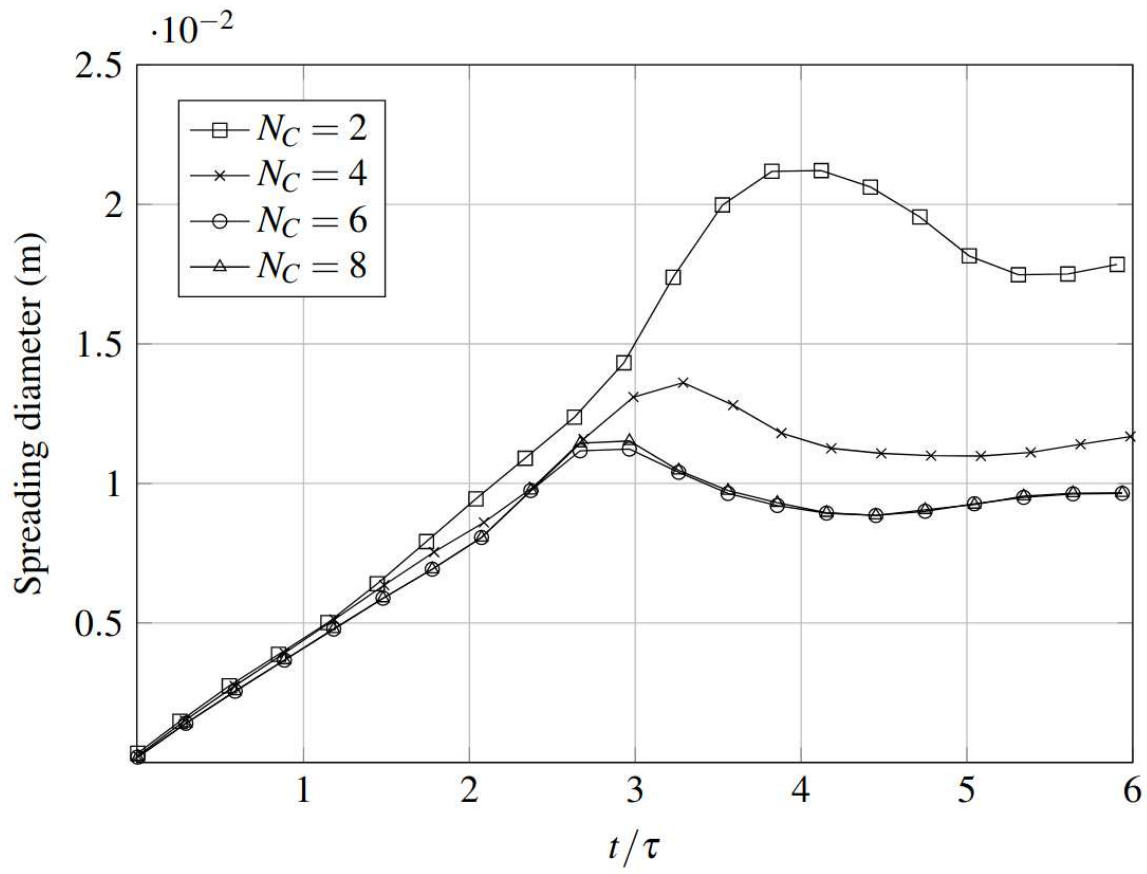
This is the author's peer reviewed, accepted manuscript. However, the online version of record will be different from this version once it has been copyedited and typeset.

PLEASE CITE THIS ARTICLE AS DOI: 10.1063/1.50131032



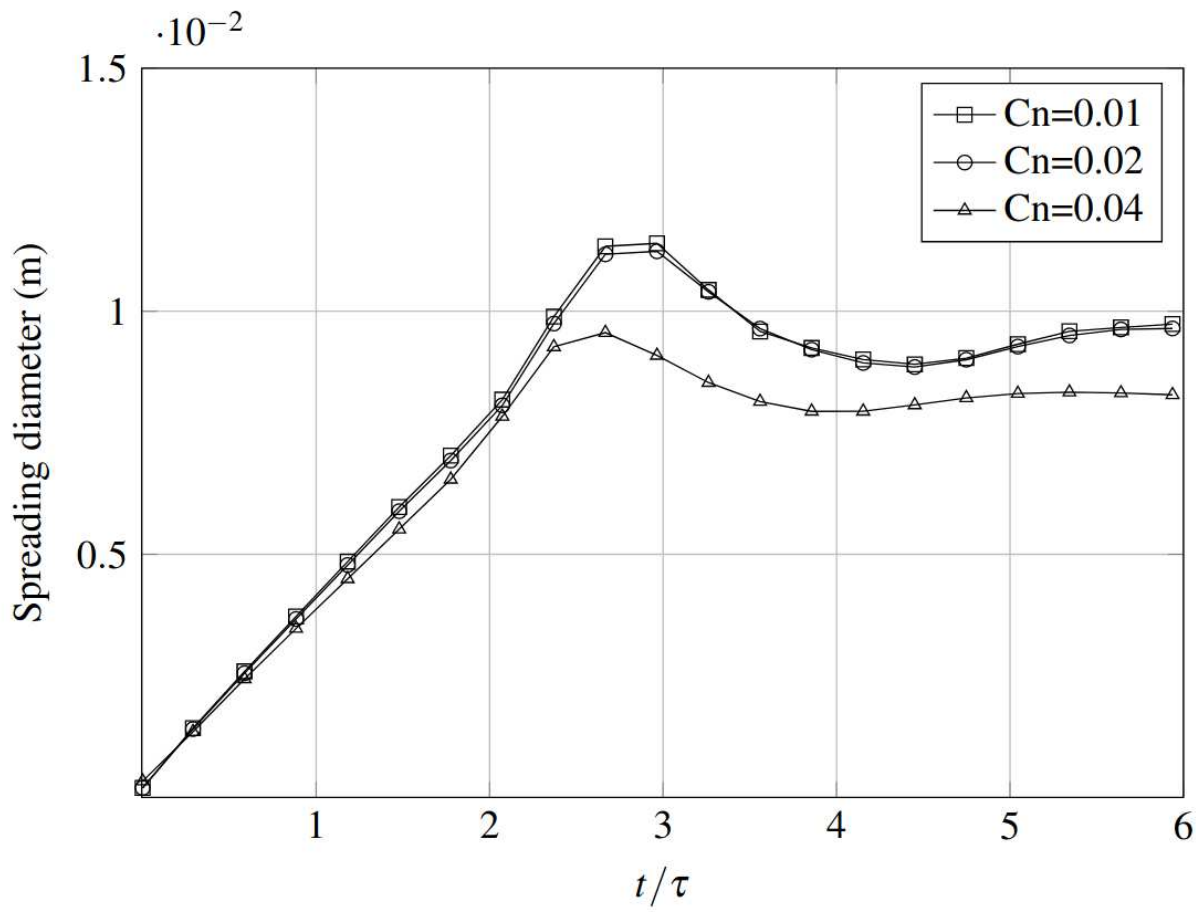
This is the author's peer reviewed, accepted manuscript. However, the online version of record will be different from this version once it has been copyedited and typeset.

PLEASE CITE THIS ARTICLE AS DOI: 10.1063/1.50131032



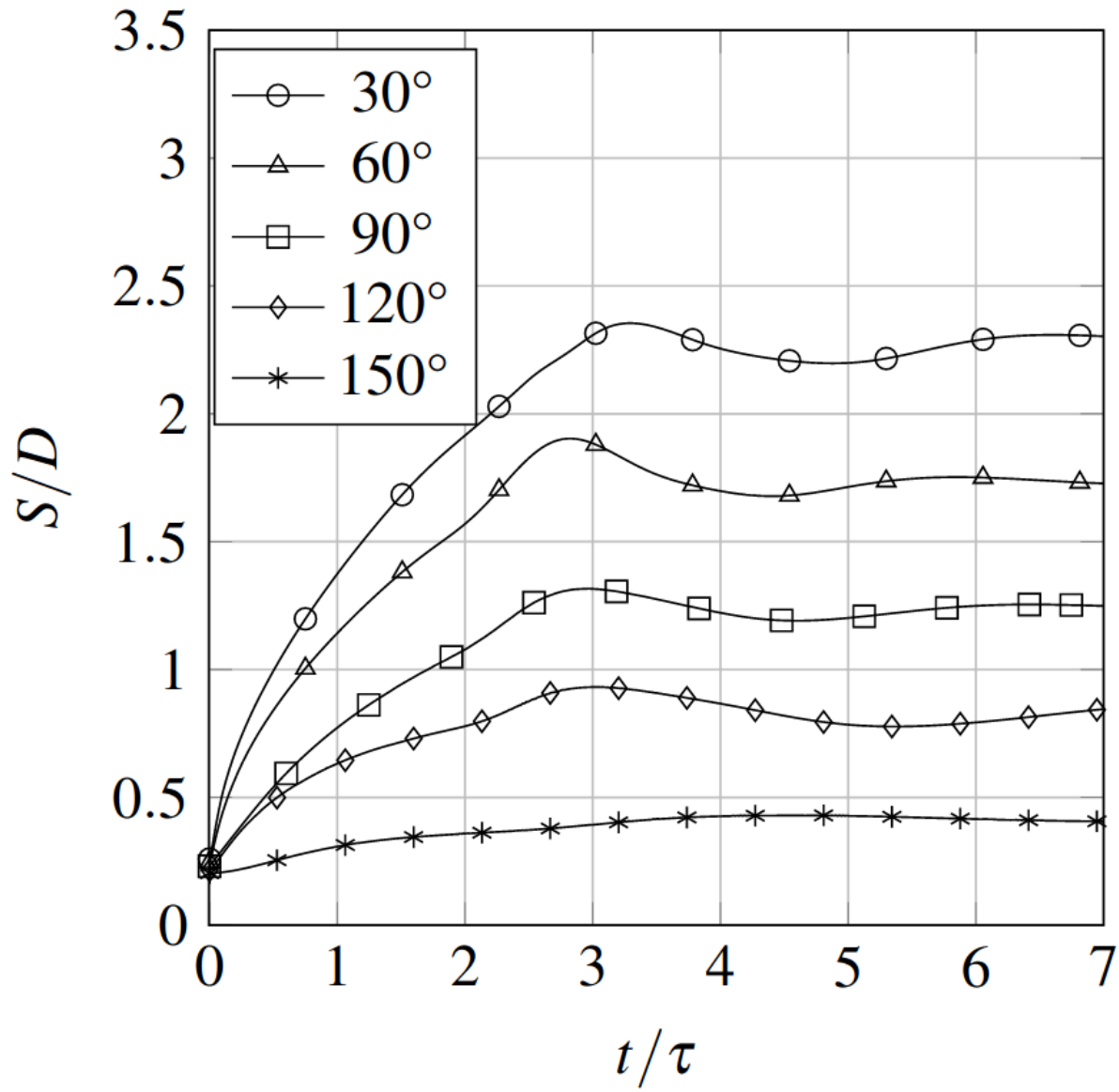
This is the author's peer reviewed, accepted manuscript. However, the online version of record will be different from this version once it has been copyedited and typeset.

PLEASE CITE THIS ARTICLE AS DOI: 10.1063/1.50131032



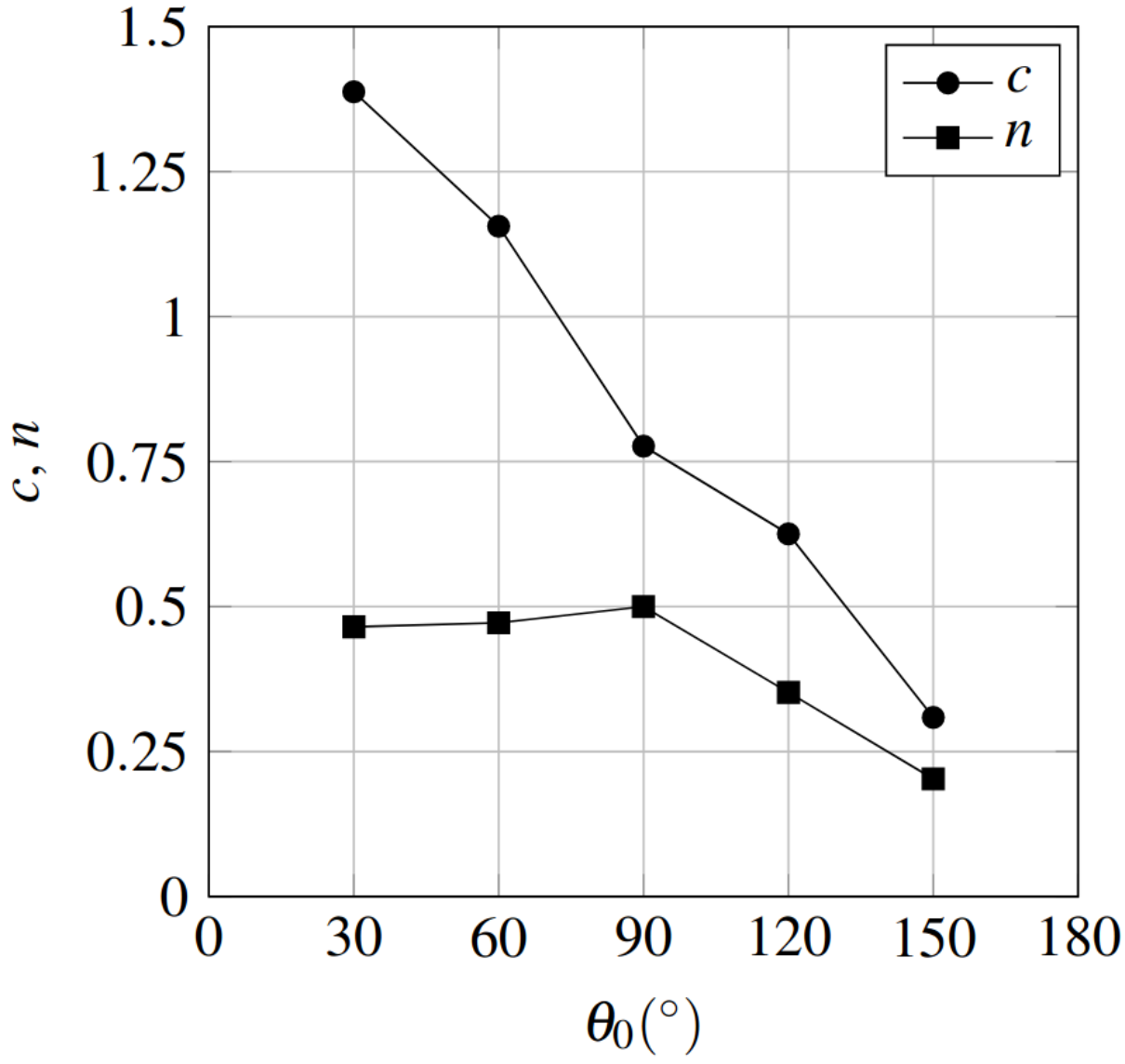
This is the author's peer reviewed, accepted manuscript. However, the online version of record will be different from this version once it has been copyedited and typeset.

PLEASE CITE THIS ARTICLE AS DOI: 10.1063/1.50131032



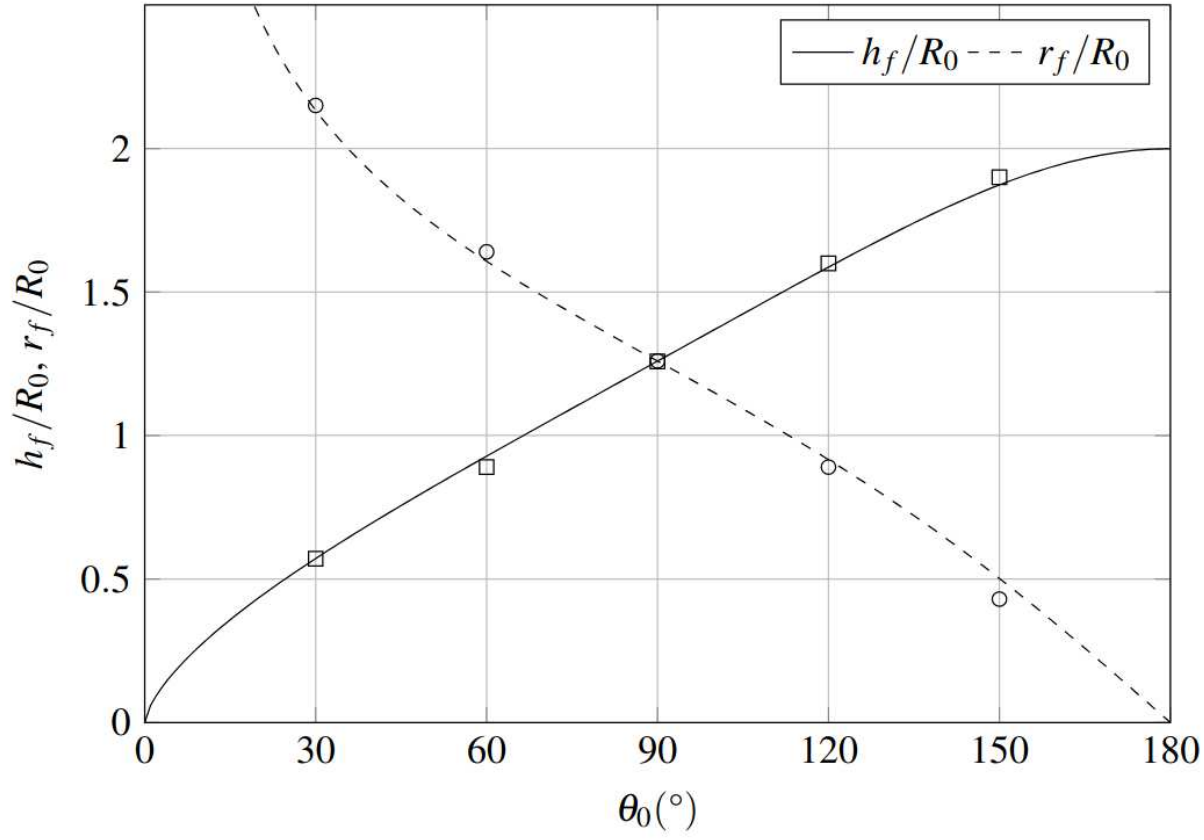
This is the author's peer reviewed, accepted manuscript. However, the online version of record will be different from this version once it has been copyedited and typeset.

PLEASE CITE THIS ARTICLE AS DOI: 10.1063/5.0131032



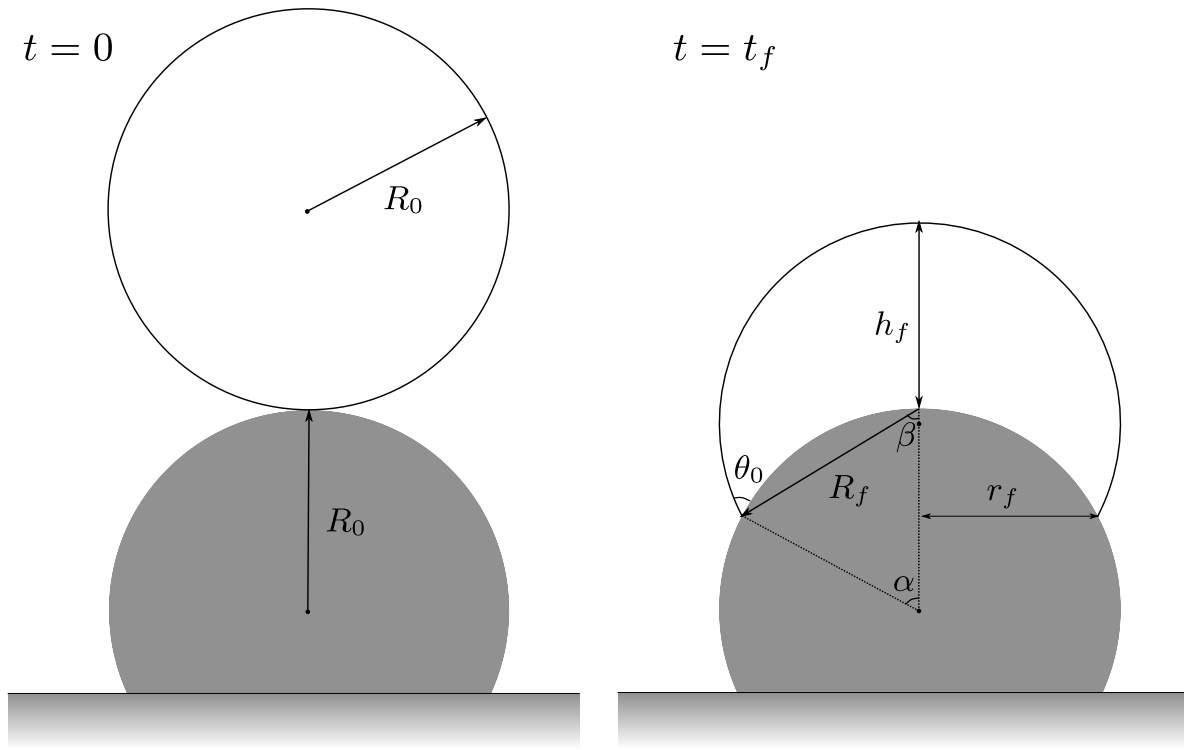
This is the author's peer reviewed, accepted manuscript. However, the online version of record will be different from this version once it has been copyedited and typeset.

PLEASE CITE THIS ARTICLE AS DOI: 10.1063/5.0131032



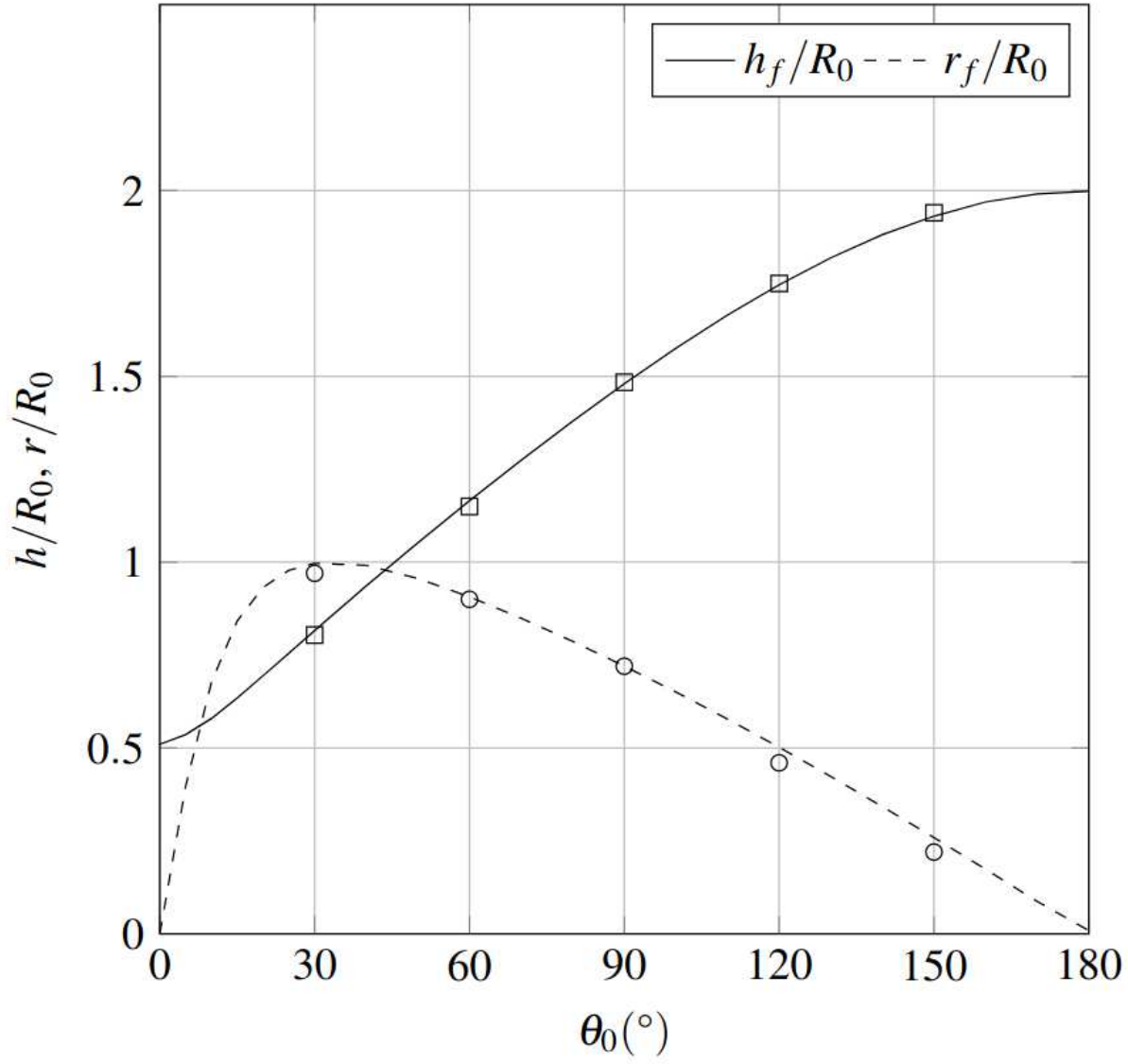
This is the author's peer reviewed, accepted manuscript. However, the online version of record will be different from this version once it has been copyedited and typeset.

PLEASE CITE THIS ARTICLE AS DOI: 10.1063/1.50131032



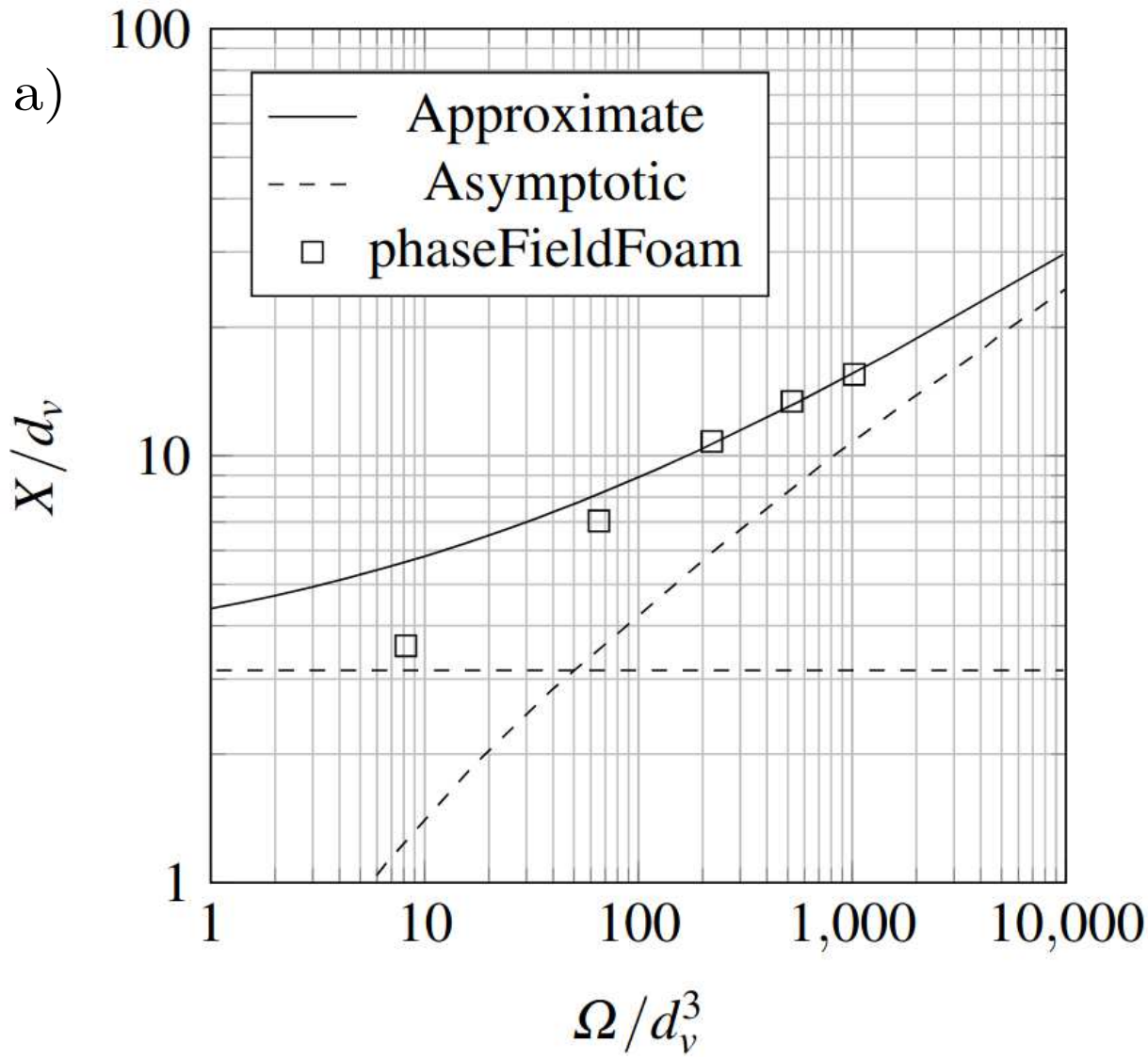
This is the author's peer reviewed, accepted manuscript. However, the online version of record will be different from this version once it has been copyedited and typeset.

PLEASE CITE THIS ARTICLE AS DOI: 10.1063/1.50131032



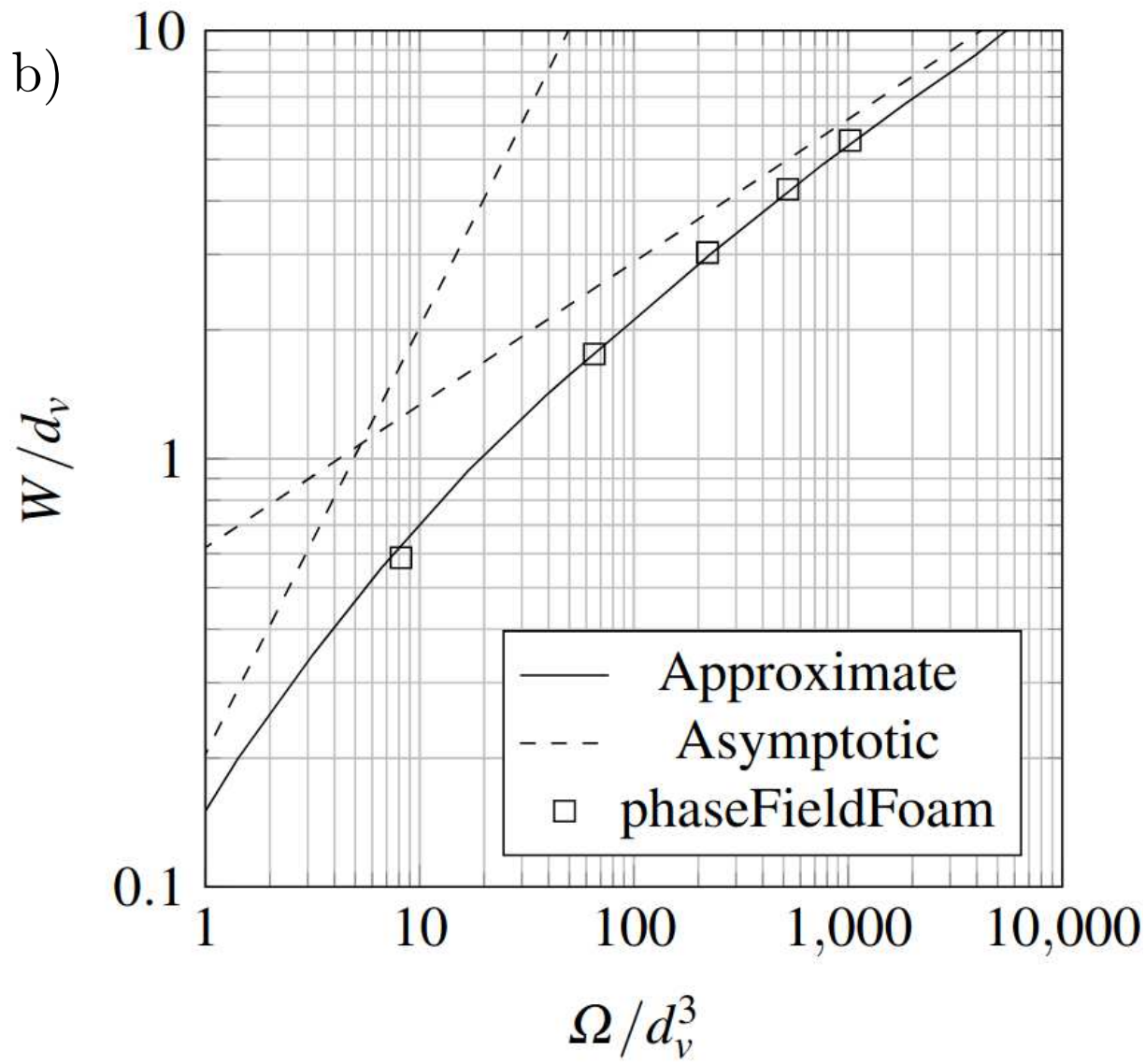
This is the author's peer reviewed, accepted manuscript. However, the online version of record will be different from this version once it has been copyedited and typeset.

PLEASE CITE THIS ARTICLE AS DOI: 10.1063/5.0131032



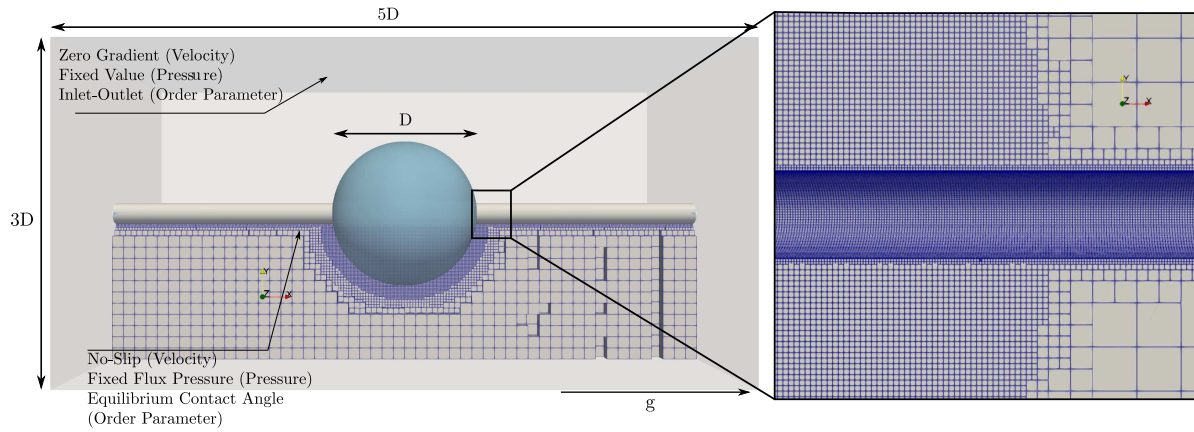
This is the author's peer reviewed, accepted manuscript. However, the online version of record will be different from this version once it has been copyedited and typeset.

PLEASE CITE THIS ARTICLE AS DOI: 10.1063/5.0131032



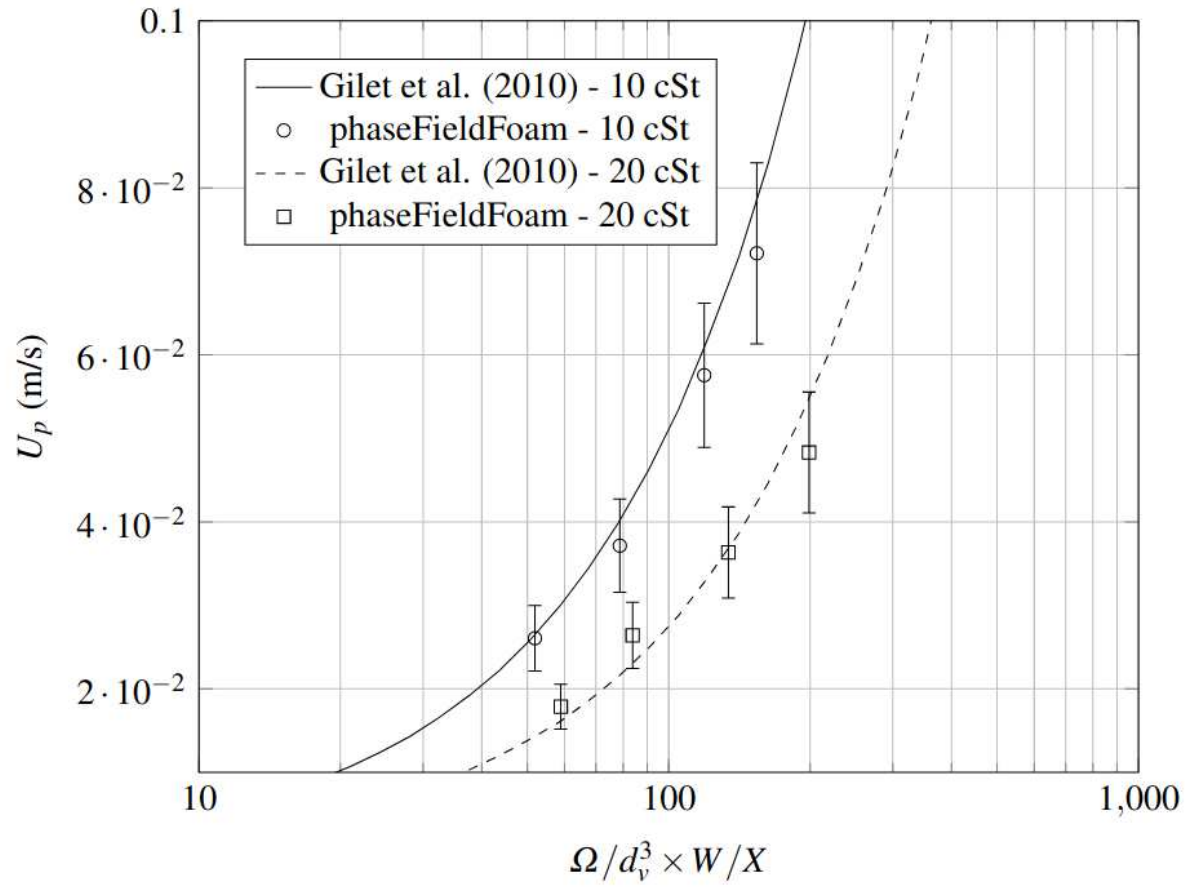
This is the author's peer reviewed, accepted manuscript. However, the online version of record will be different from this version once it has been copyedited and typeset.

PLEASE CITE THIS ARTICLE AS DOI: 10.1063/1.50131032



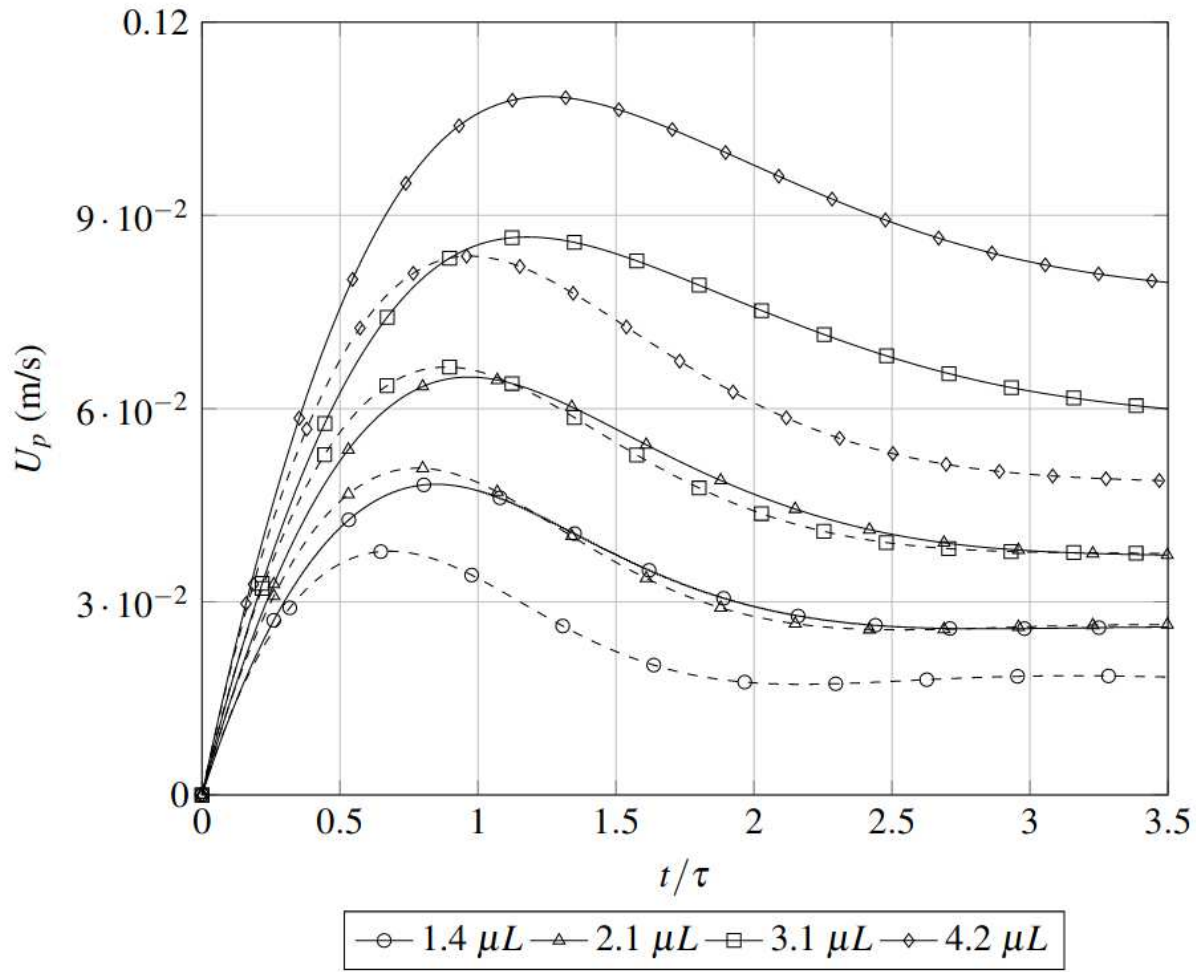
This is the author's peer reviewed, accepted manuscript. However, the online version of record will be different from this version once it has been copyedited and typeset.

PLEASE CITE THIS ARTICLE AS DOI: 10.1063/1.50131032



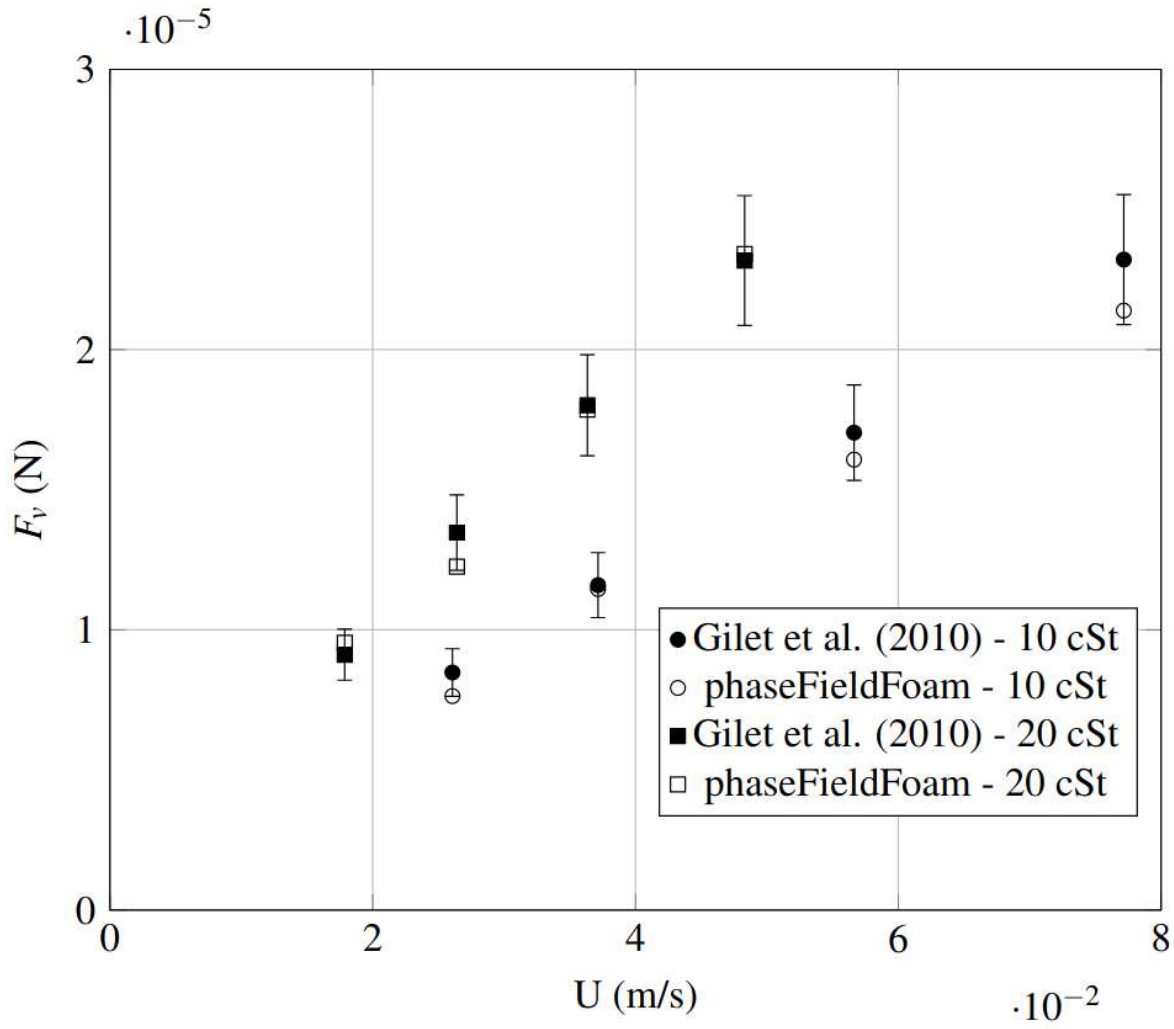
This is the author's peer reviewed, accepted manuscript. However, the online version of record will be different from this version once it has been copyedited and typeset.

PLEASE CITE THIS ARTICLE AS DOI: 10.1063/1.50131032



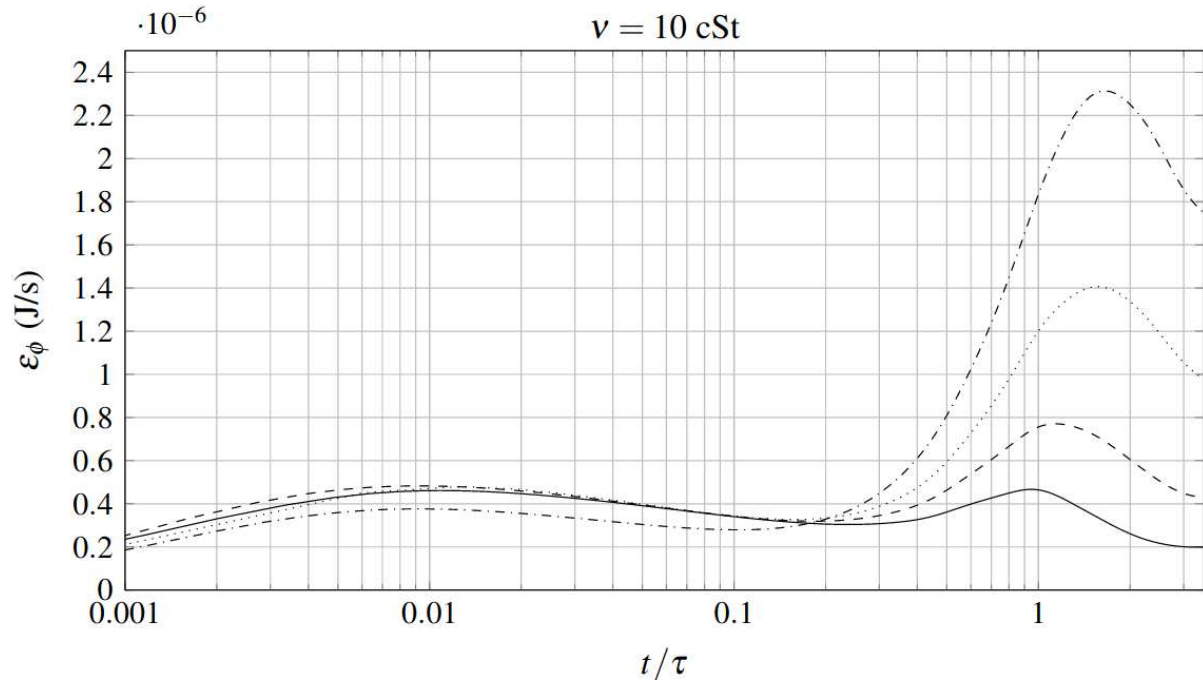
This is the author's peer reviewed, accepted manuscript. However, the online version of record will be different from this version once it has been copyedited and typeset.

PLEASE CITE THIS ARTICLE AS DOI: 10.1063/1.50131032



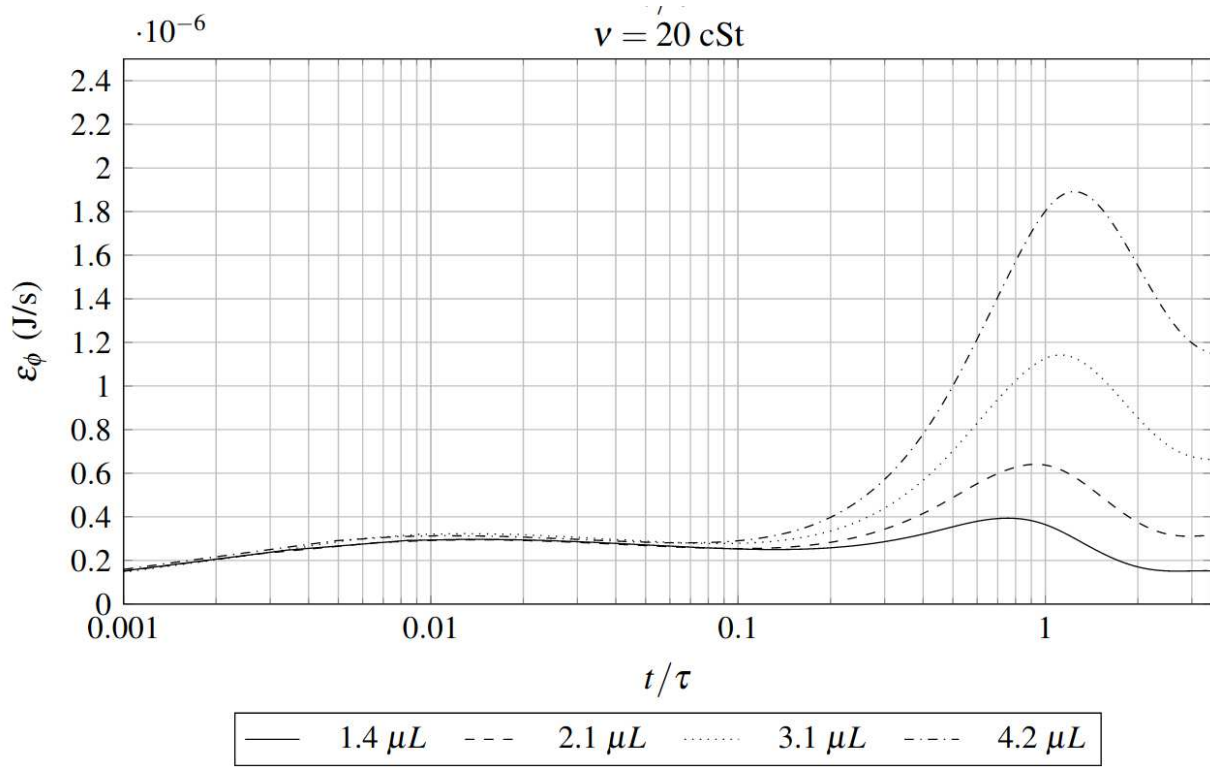
This is the author's peer reviewed, accepted manuscript. However, the online version of record will be different from this version once it has been copyedited and typeset.

PLEASE CITE THIS ARTICLE AS DOI: 10.1063/1.50131032



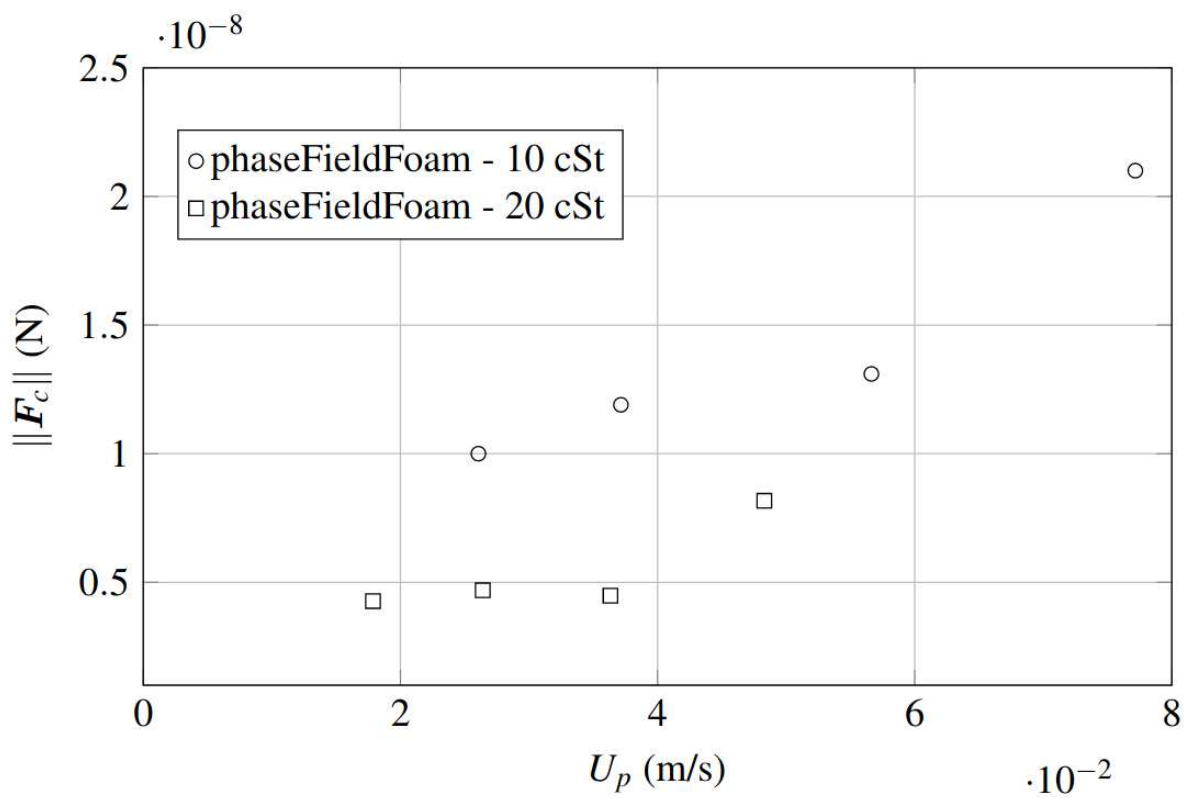
This is the author's peer reviewed, accepted manuscript. However, the online version of record will be different from this version once it has been copyedited and typeset.

PLEASE CITE THIS ARTICLE AS DOI: 10.1063/1.50131032



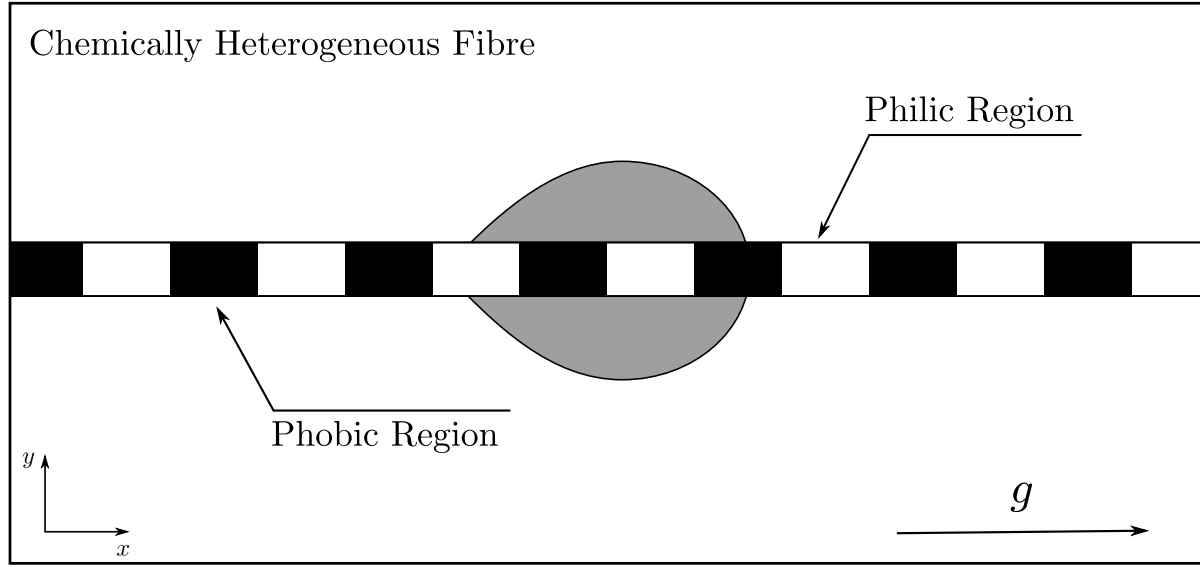
This is the author's peer reviewed, accepted manuscript. However, the online version of record will be different from this version once it has been copyedited and typeset.

PLEASE CITE THIS ARTICLE AS DOI: 10.1063/1.50131032



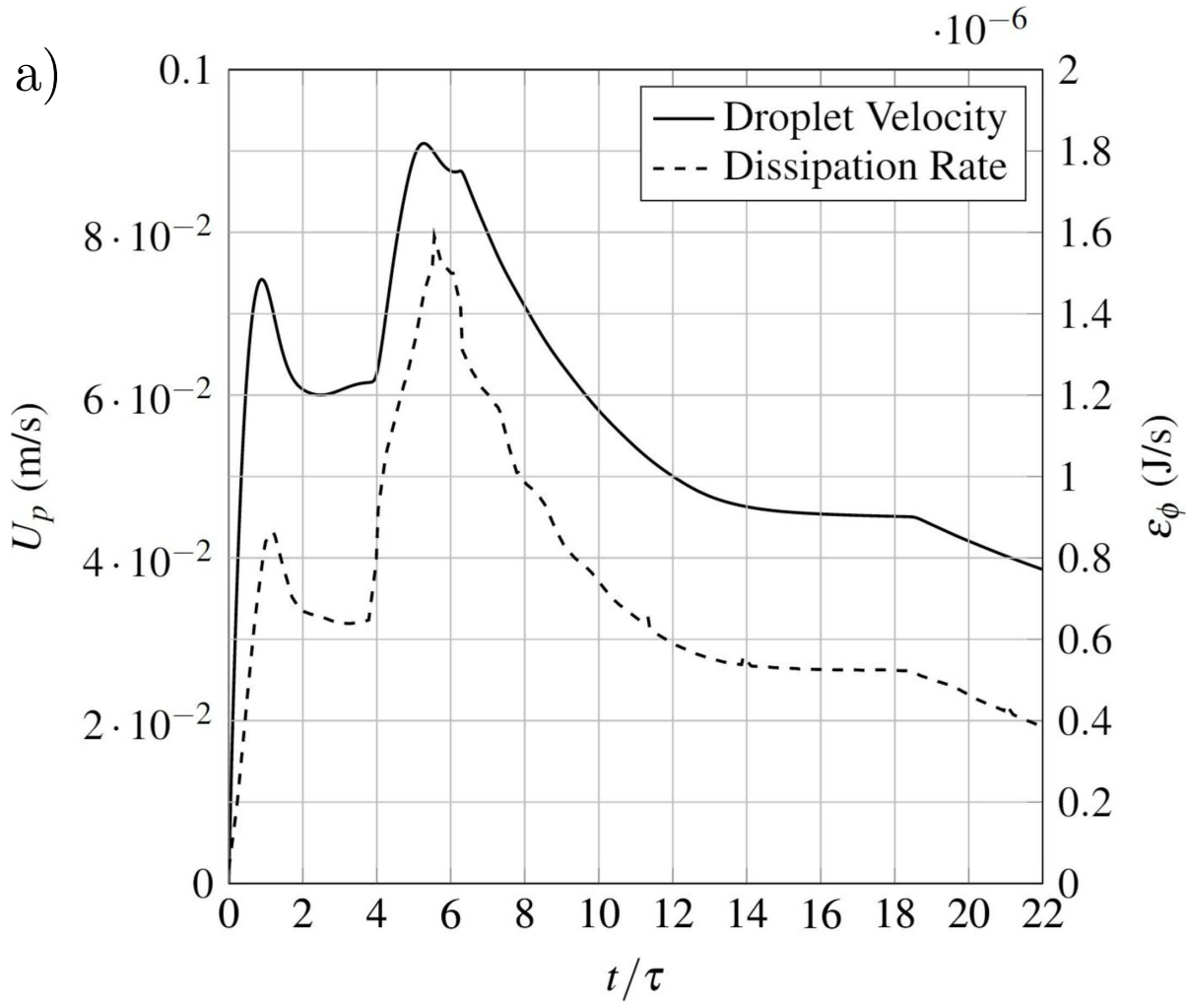
This is the author's peer reviewed, accepted manuscript. However, the online version of record will be different from this version once it has been copyedited and typeset.

PLEASE CITE THIS ARTICLE AS DOI: 10.1063/1.50131032



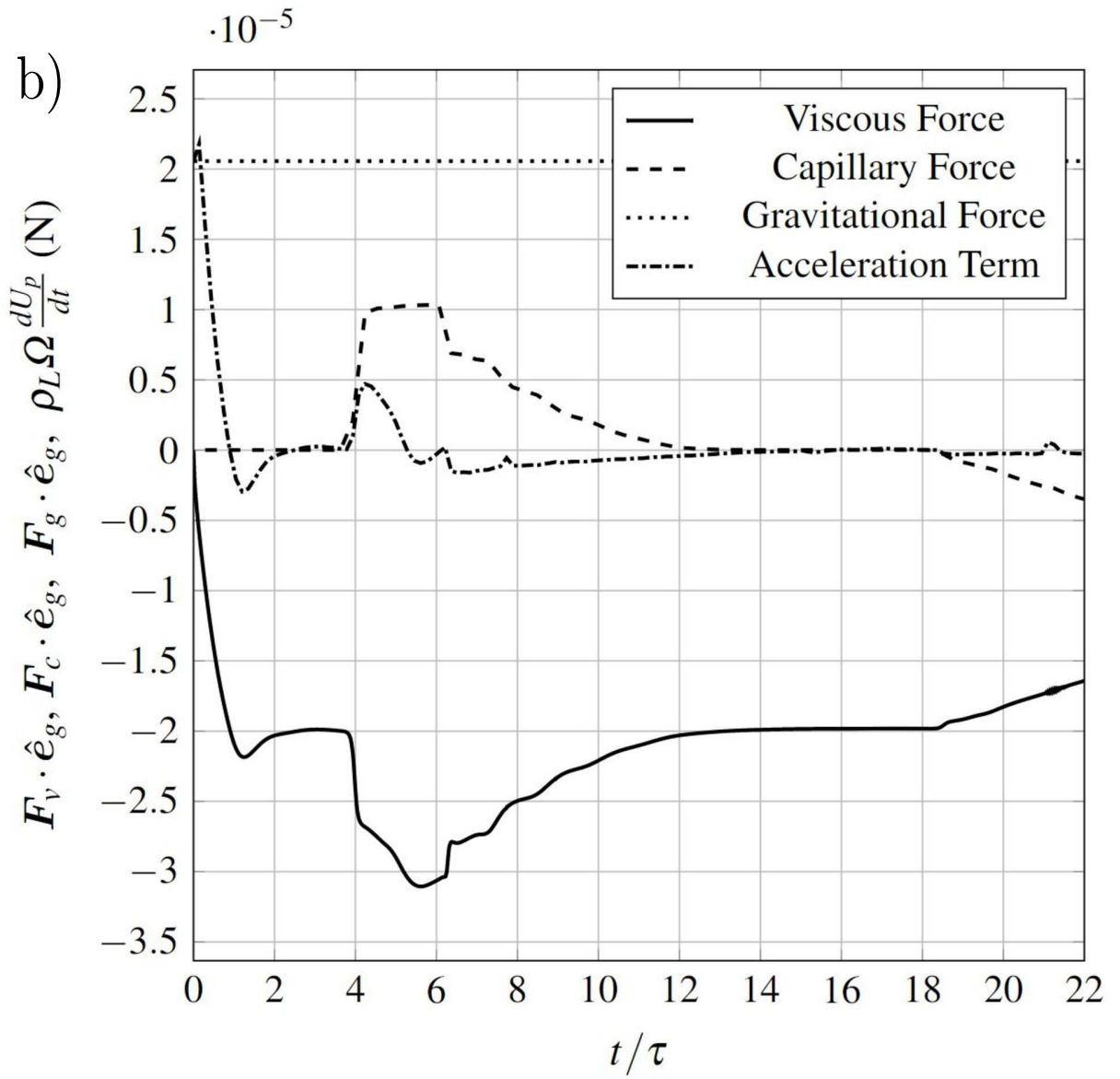
This is the author's peer reviewed, accepted manuscript. However, the online version of record will be different from this version once it has been copyedited and typeset.

PLEASE CITE THIS ARTICLE AS DOI: 10.1063/1.50131032



This is the author's peer reviewed, accepted manuscript. However, the online version of record will be different from this version once it has been copyedited and typeset.

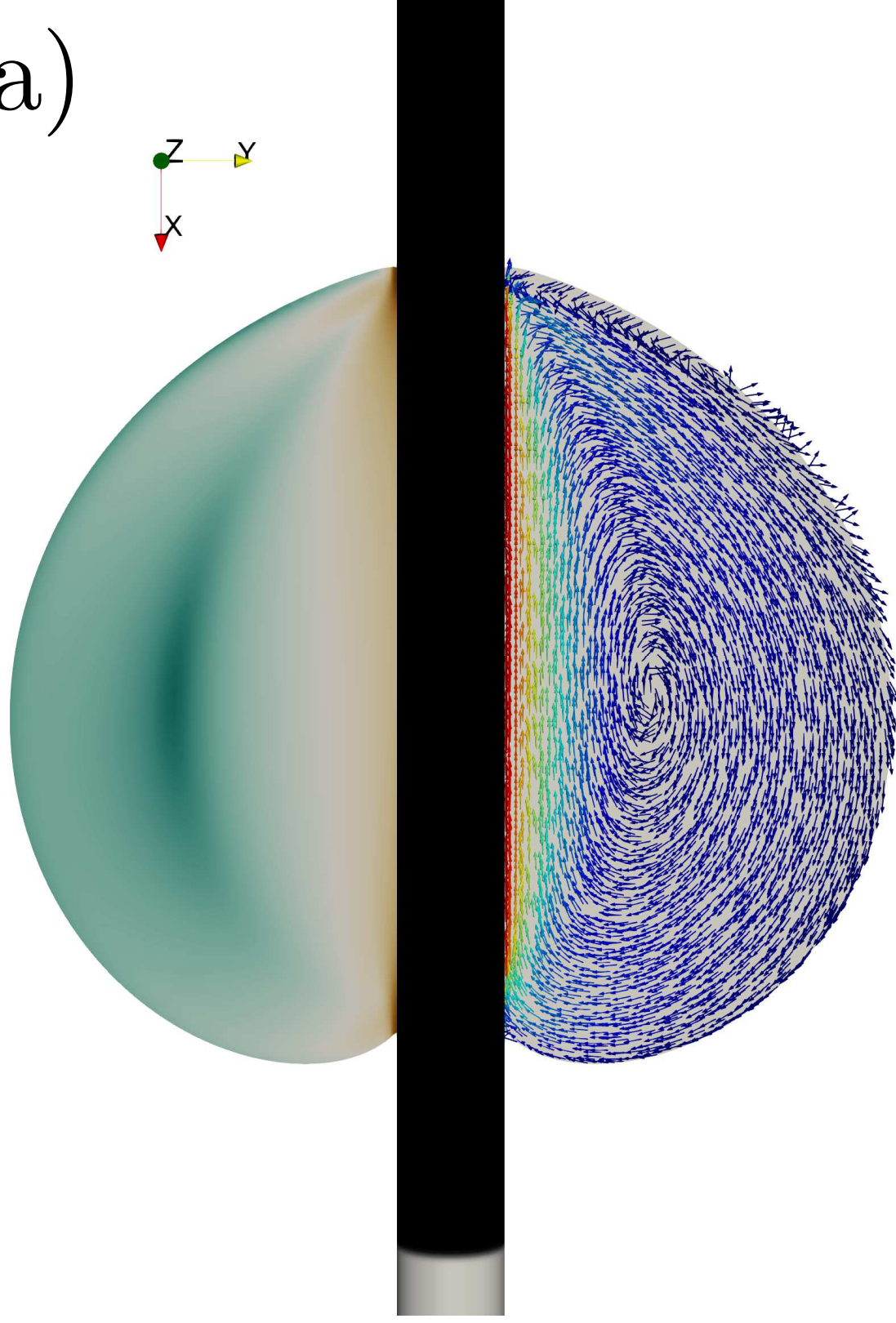
PLEASE CITE THIS ARTICLE AS DOI: 10.1063/5.0131032



This is the author's peer reviewed, accepted manuscript. However, the online version of record will be different from this version once it has been copyedited and typeset.

PLEASE CITE THIS ARTICLE AS DOI: 10.1063/5.0131032

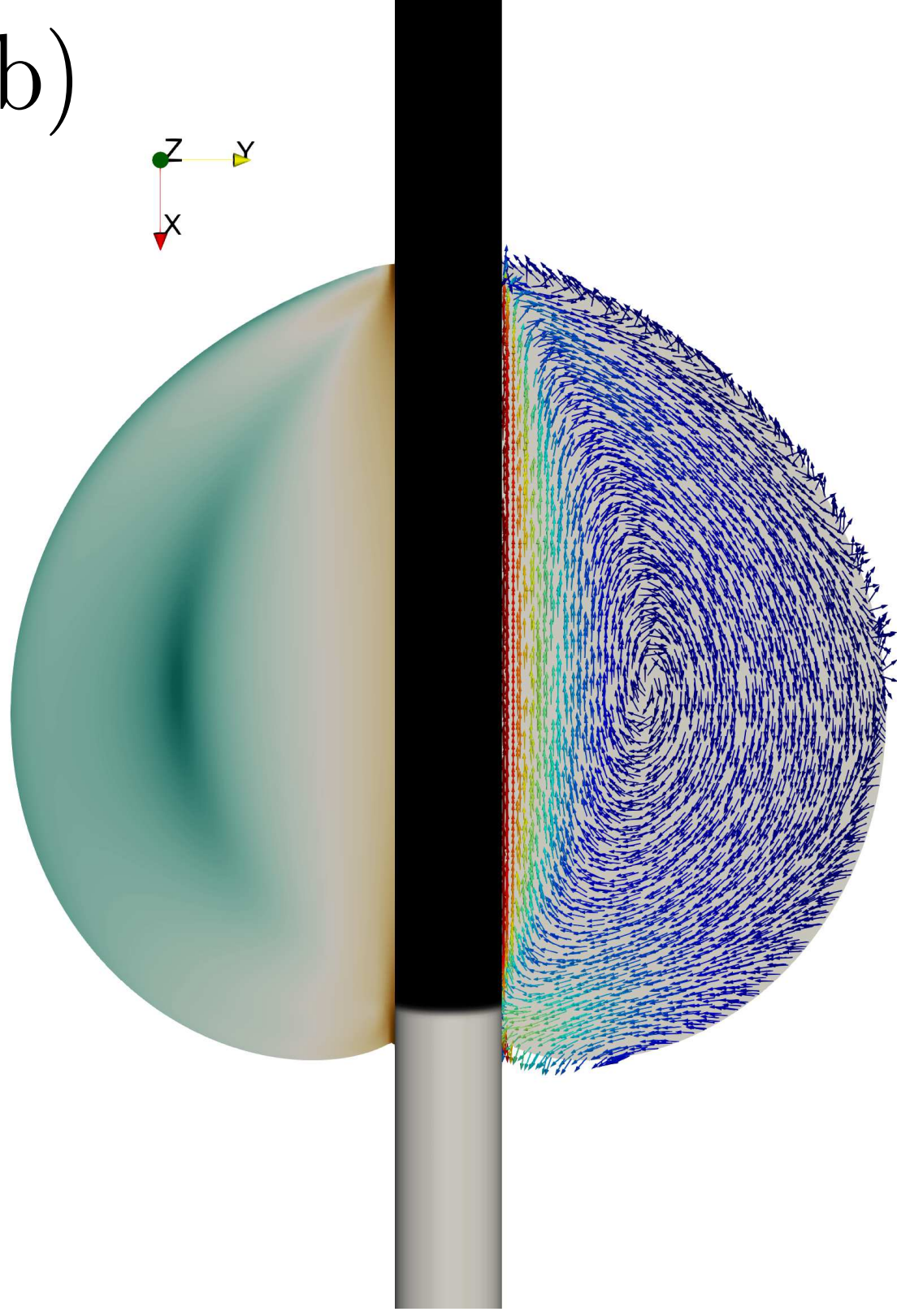
a)



This is the author's peer reviewed, accepted manuscript. However, the online version of record will be different from this version once it has been copyedited and typeset.

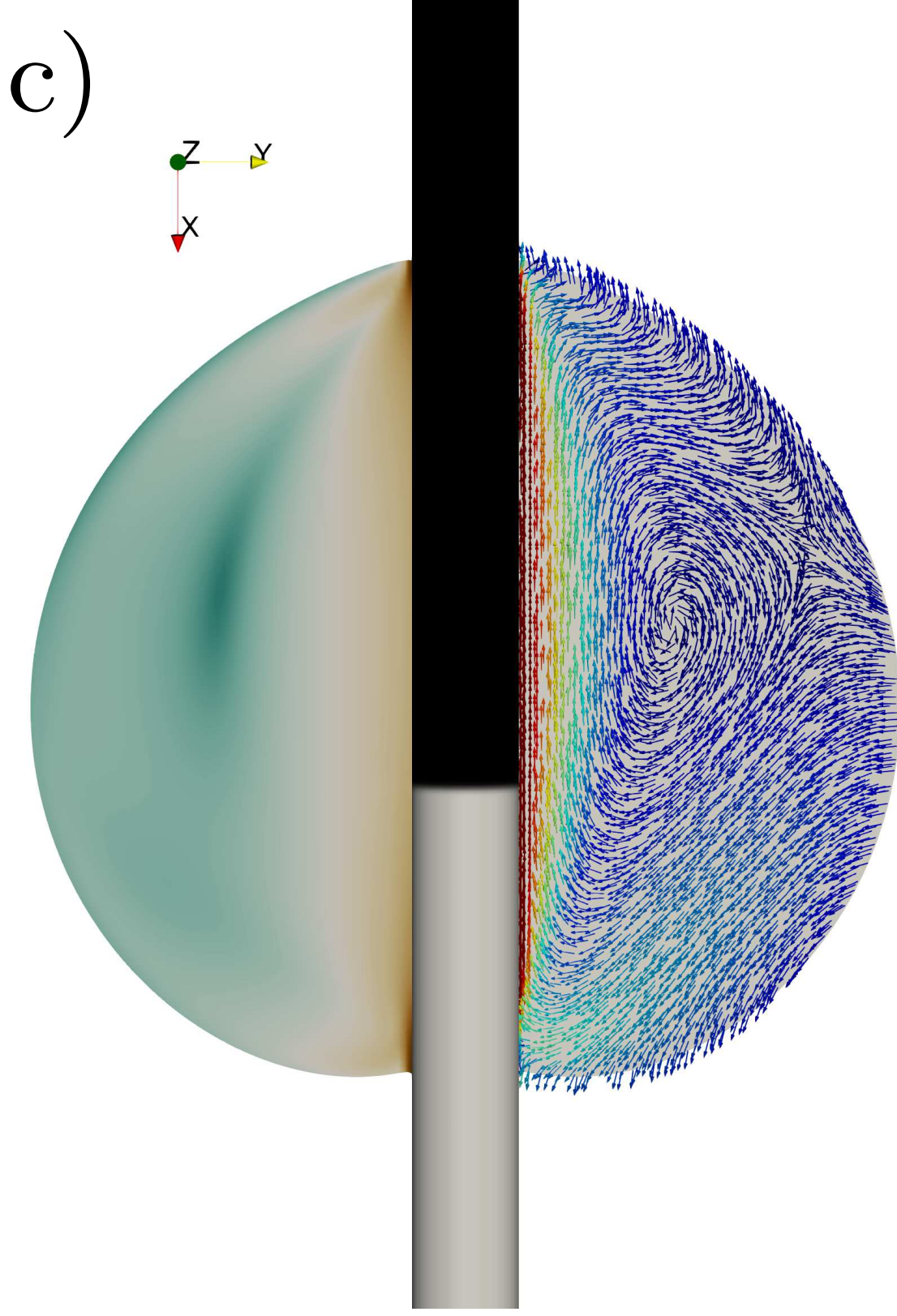
PLEASE CITE THIS ARTICLE AS DOI: 10.1063/5.0131032

b)



This is the author's peer reviewed, accepted manuscript. However, the online version of record will be different from this version once it has been copyedited and typeset.

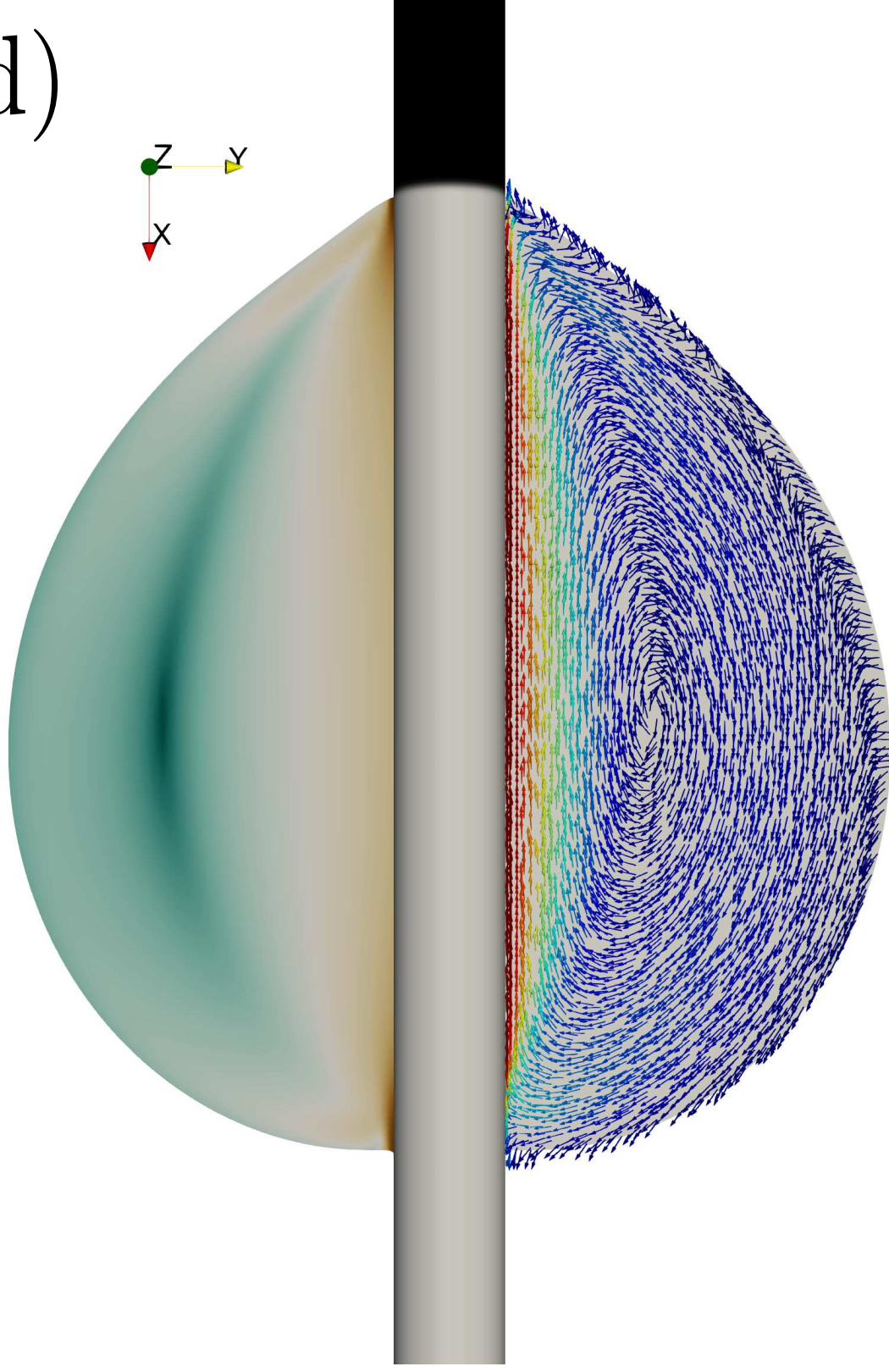
PLEASE CITE THIS ARTICLE AS DOI: 10.1063/5.0131032



This is the author's peer reviewed, accepted manuscript. However, the online version of record will be different from this version once it has been copyedited and typeset.

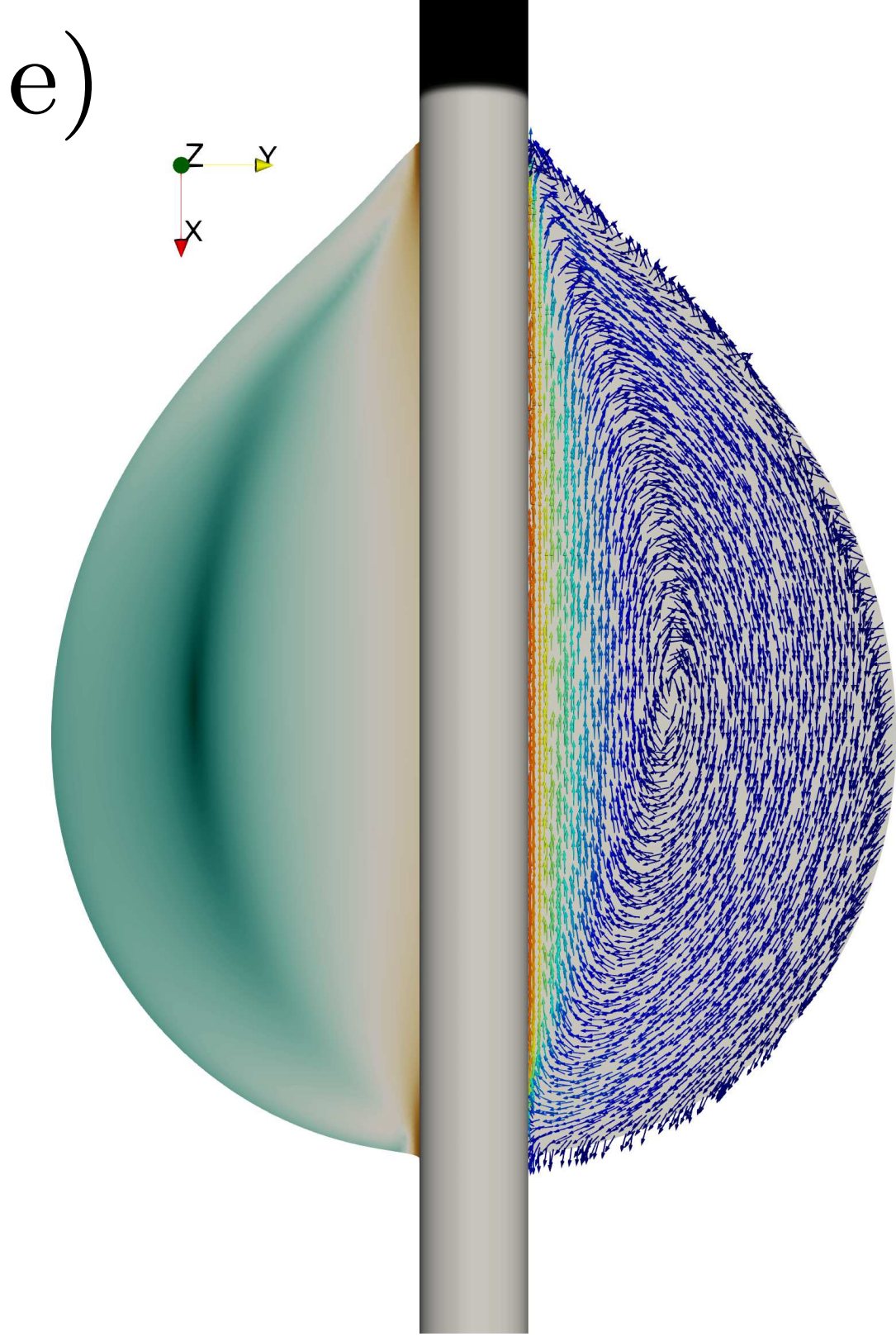
PLEASE CITE THIS ARTICLE AS DOI: 10.1063/5.0131032

d)



This is the author's peer reviewed, accepted manuscript. However, the online version of record will be different from this version once it has been copyedited and typeset.

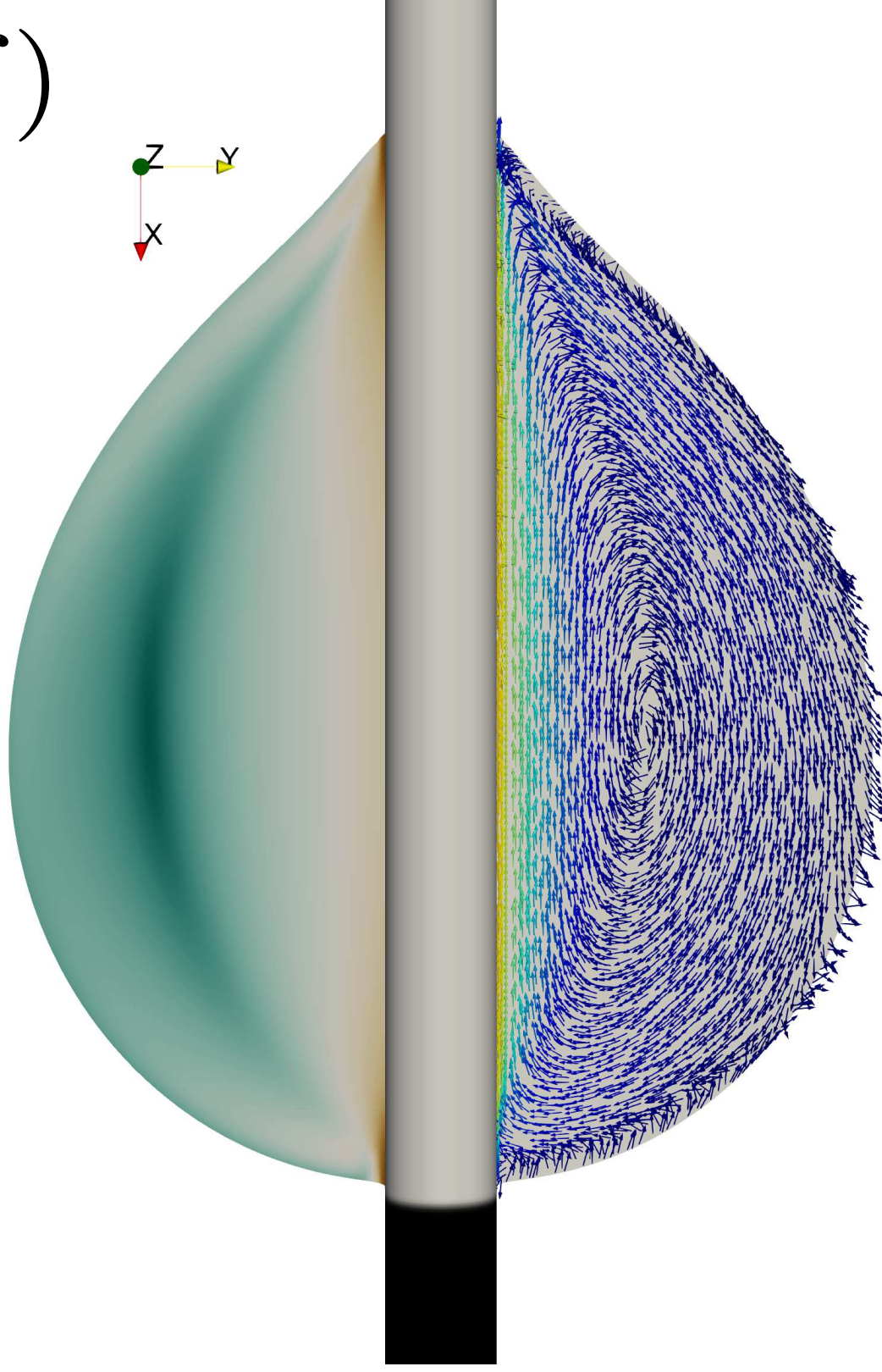
PLEASE CITE THIS ARTICLE AS DOI: 10.1063/5.0131032



This is the author's peer reviewed, accepted manuscript. However, the online version of record will be different from this version once it has been copyedited and typeset.

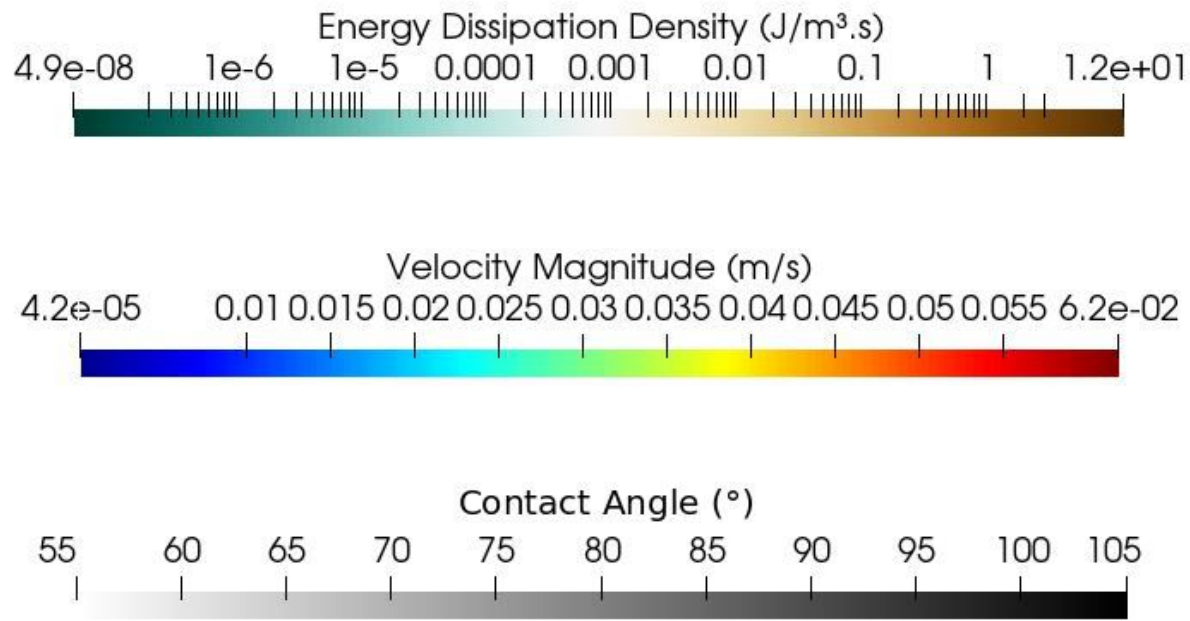
PLEASE CITE THIS ARTICLE AS DOI: 10.1063/5.0131032

f)



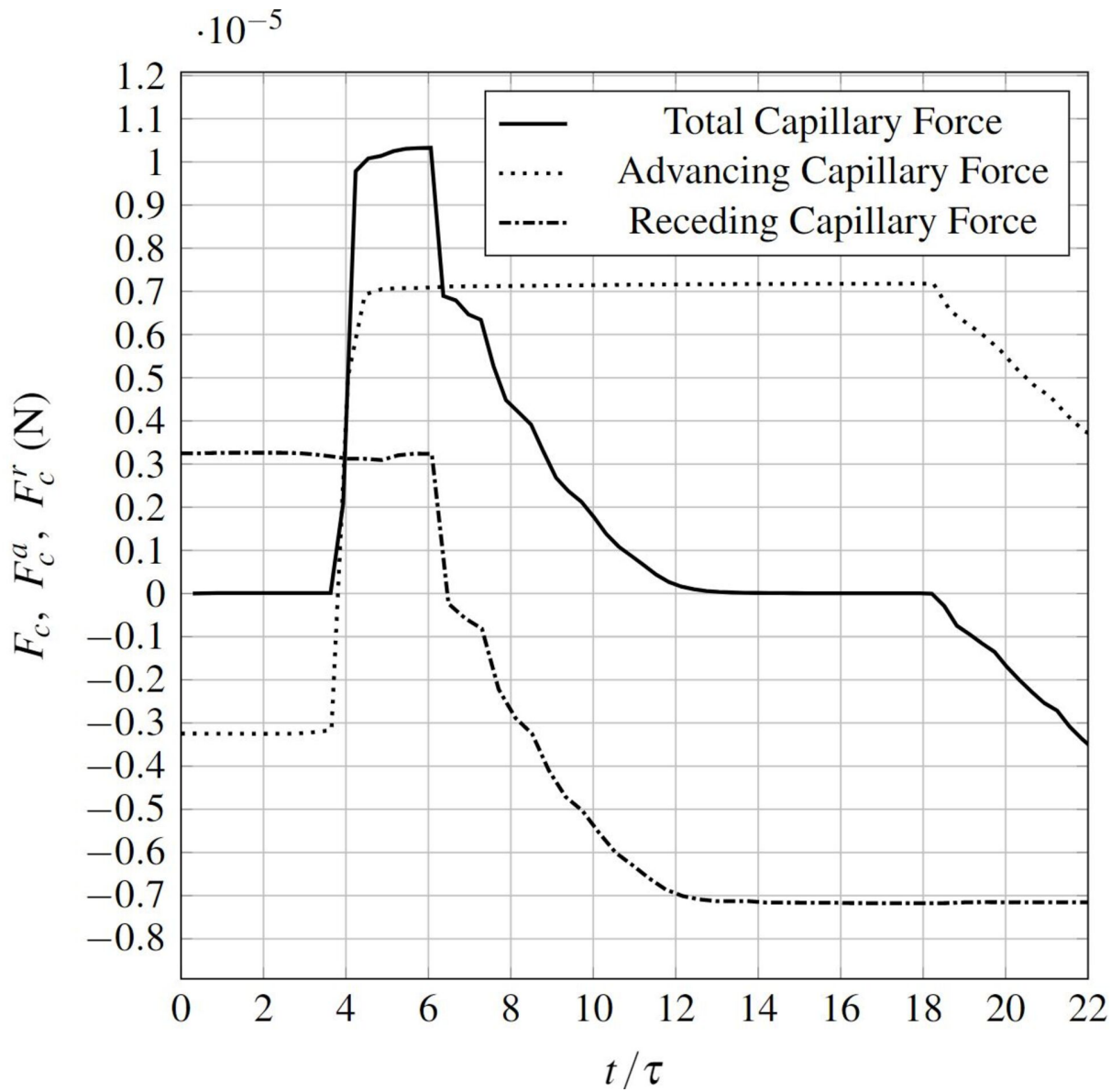
This is the author's peer reviewed, accepted manuscript. However, the online version of record will be different from this version once it has been copyedited and typeset.

PLEASE CITE THIS ARTICLE AS DOI: 10.1063/1.50131032



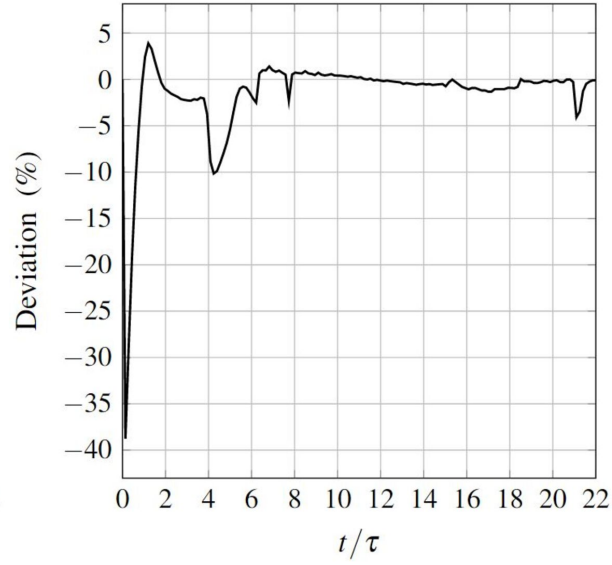
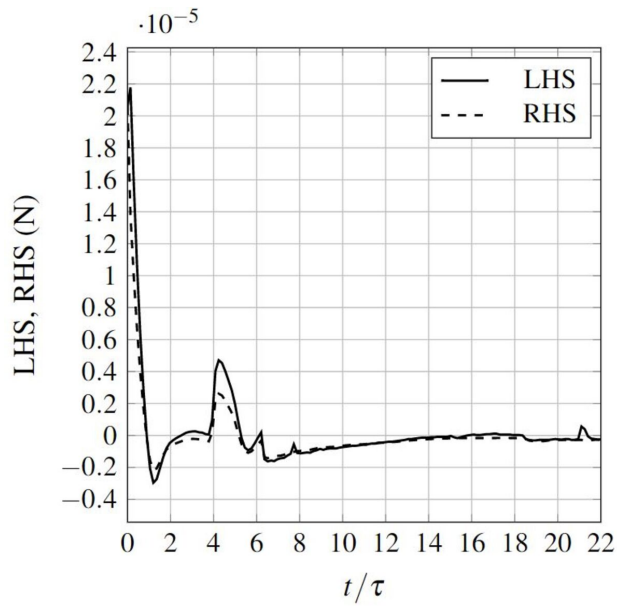
This is the author's peer reviewed, accepted manuscript. However, the online version of record will be different from this version once it has been copyedited and typeset.

PLEASE CITE THIS ARTICLE AS DOI: 10.1063/1.50131032



This is the author's peer reviewed, accepted manuscript. However, the online version of record will be different from this version once it has been copyedited and typeset.

PLEASE CITE THIS ARTICLE AS DOI: 10.1063/1.50131032



This is the author's peer reviewed, accepted manuscript. However, the online version of record will be different from this version once it has been copyedited and typeset.
 PLEASE CITE THIS ARTICLE AS DOI: 10.1063/1.50131032

